NMR Spectroscopy of Biomolecular Liquid-Liquid Phase Separation

Dissertation
For award of the degree
"Doctor rerum naturalium" (Dr.rer.nat.)
Of the Georg- August-Universität Göttingen

Within the doctoral program
"Physics of Biological and Complex Systems"
Of the Georg-August University School of Science (GAUSS)

Submitted by
Crhistian Felipe Pantoja Rivillas
From Palmira, Colombia

Göttingen 2023

Thesis committee

Prof. Dr. Markus Zweckstetter
Structure Determination of Proteins Using NMR
Max-Planck-Institute for Multidisciplinary Sciences, Göttingen, Germany
Translational Structural Biology, German Center for Neurodegenerative Disease, Göttingen

Prof. Dr. Marina Bennati
Electron-spin Resonance Spectroscopy
Max-Planck-Institute for Multidisciplinary Sciences, Göttingen, Germany

Prof. Dr. Stefan Jakobs
Mitochondrial Structure and Dynamics Group
Max-Planck-Institute for Multidisciplinary Sciences, Göttingen, Germany
Clinic of Neurology, University Medical Center Göttingen, Germany

Members of the examination board

1st referee:
Prof. Dr. Markus Zweckstetter
Structure Determination of Proteins Using NMR
Max-Planck-Institute for Multidisciplinary Sciences, Göttingen, Germany
Translational Structural Biology, German Center for Neurodegenerative Disease, Göttingen

2st referee:
Prof. Dr. Marina Bennati
Electron-spin Resonance Spectroscopy
Max-Planck-Institute for Multidisciplinary Sciences, Göttingen, Germany

Further Members of the examination board

Prof. Dr. Stefan Jakobs
Mitochondrial Structure and Dynamics Group
Max-Planck-Institute for Multidisciplinary Sciences, Göttingen, Germany
Clinic of Neurology, University Medical Center Göttingen, Germany

Prof. Dr. Bert de Groot
Computational Biomolecular Dynamics
Max-Planck-Institute for Multidisciplinary Sciences, Göttingen, Germany

Dr. David Zwicker
Theory of Biological Fluids
Max-Planck-Institute for Dynamics and Self Organization, Göttingen, Germany

Prof. Dr. Christian Griesinger
NMR-based Structural Biology
Max-Planck-Institute for Multidisciplinary Sciences, Göttingen, Germany

Date oral examination: 10th March 2023

Acknowledgments

First of all, I would like to thank Prof. Markus Zweckstetter for the great opportunity to work in his laboratory and for giving me all the facilities to conduct the present doctoral work, as well as his guidance and support in the development of the project. I will always be very grateful to him.

I would also like to thank Prof. Marina Bennati and Prof. Stefan Jakobs for their support and fruitful discussions about my doctoral project in our TAC meetings.

Moreover, I would like to thank the DAAD for all the financial and logistical support to make my doctoral project possible.

I would also like to thank Conny for her support and willingness to help me in all situations where I needed help.

I would like to thank Sol for providing me with indispensable materials such as the protein that I have used extensively during this project, but also for the good conversations and support she has always given me.

I would especially like to thank Alain for his indispensable guidance in understanding the biology behind phase separation and for the long scientific discussions we often had in the mornings.

Additionally, I would like to thank all my colleagues and former lab mates Filippo, David, Timo, Adriana, Pijush, Tina, Antonia, Taekyung, Maria, Jeff, Lisa, Conny, S, Matthew, Gwladys, Milan, Zheng, Irina, Anton, Reshma, Debdeep and Fiamma for the shared moments and for a comfortable working environment.

I would like to thank my colleagues in the NMR II department, Juan Carlos and Daniel for their sincere friendship and enormous support during all these years. Especially to Juan Carlos for his support and help when it was needed the most.

Thank you to all the staff of the NMR II who in one way or another have been involved in the undertaking of this project and made its completion possible.

I would like to thank my friends in Göttigen, Giorgio, Morine, Karol, Daniel, Juan Carlos, for the many dinners and good times we spent together these years.

Especially, I would like to thank Virginia for her unconditional support and company during this whole process. I will always be deeply grateful to her.

I would like to thank my family Maria Elena, Enrique and Negro for their support and love throughout this process. Especially to my mother Maria Elena for being my inspiration and encouragement.

Abstract

Phase separation of biomolecules has transformed our understanding of cell organization and function, motivating intensive research in the last decade. New evidence for their critical role in mechanisms essential for cellular function has been uncovered. However, little is known regarding the molecular factors that govern their function, and techniques capable of probing their intrinsically dynamic nature are required. Nuclear magnetic resonance (NMR) spectroscopy is a powerful method to study biomolecules in solution, with its flexibility making it very attractive to study transitory and dynamic systems.

In manuscript 1, we first explore the kinetics of droplet formation using NMR spectroscopy on a model system. The simplicity and versatility of the triethylamine (TEA)/water system offers a detailed description of the nucleation process and demixing kinetics. Notably, we detected a chemical exchange process between nucleation sites and matrix solution in the slow time scale of NMR. The corresponding exchange rate was quantified using exchange spectroscopy (EXSY) mediated by cooling/heating cycling. Finally, we illustrated the potential of our strategy by quantifying the exchange rate of a client molecule in the system.

In manuscript 2, we analyze the potential of NMR to study non-uniform samples or two-phase systems. We developed an improved spatially resolved NMR experiment to study a phase-separated sample of Tau protein. By including a suitable water suppression block, multicomponent quantification of small and large molecules was feasible. We provide an extended strategy to quantify protein concentration in a spatially resolved fashion. Additionally, we presented a quantitative phase diagram of Tau protein using spatially resolved NMR.

Finally, in manuscript 3 we demonstrate the application of NMR to study biochemical reactions inside biomolecular condensates. Here, we monitored in real-time the phosphorylation process of Tau condensate mediated by the kinase CDK2. The kinetic data revealed that phosphorylation inside Tau condensate is accelerated compared to dispersed phase. Altogether, the present findings push the borders of the applicability of NMR to challenging phase separate systems, extending our understanding of the molecular factors behind the phase separation process.

Publications

Dynamic component exchange in a model phase separating system: an NMR approach

Pantoja, C. F., Zweckstetter, M., & Rezaei-Ghaleh, N. (2022). Dynamical component exchange in a model phase separating system: an NMR-based approach. *Physical Chemistry Chemical Physics*, 24(10), 6169-6175. https://doi.org/10.1039/D2CP00042C

Authors: Christian F. Pantoja, Markus Zweckstetter, Nasrollah Rezaei-Ghaleh.

Author contribution: *C. F. P., M. Z. and N. R.-G.: conceptualization, funding acquisition, data curation; C. F. P.: investigation, visualization; C. F. P. and N. R.-G.: methodology, formal analysis; M. Z. and N. R.-G.: supervision; M. Z.: writing – review & editing; N. R.-G.: writing – original draft.*

Determining the Physico-Chemical Composition of Biomolecular Condensates from Spatially-Resolved NMR

Pantoja, C. F., Ibáñez de Opakua, A., Cima-Omori, M. S., & Zweckstetter, M. (2023). Determining the Physico-Chemical Composition of Biomolecular Condensates from Spatially-Resolved NMR. Angewandte Chemie International Edition, 62(17), e202218078. https://doi.org/10.1002/anie.202218078

Authors: Christian F. Pantoja, Alain Ibáñez de Opakua, Maria-Sol Cima-Omori, Markus Zweckstetter

Author contribution: *C.F.P.: designed and conducted NMR experiments, as well acquired and analyzed data; C.F.P., AldO and M.Z.: conceptualization and visualization. M.S.C.: Produced the protein; M.Z.: supervision; M.Z and C.F.P.: writing and editing manuscript.*

Condensed-phase signaling can expand kinase specificity and respond to macromolecular crowding

Sang, D., Shu, T., Pantoja, C. F., de Opakua, A. I., Zweckstetter, M., & Holt, L. J. (2022). Condensed-phase signaling can expand kinase specificity and respond to macromolecular crowding. *Molecular Cell*, 82(19), 3693-3711. https://doi.org/10.1016/j.molcel.2022.08.016

Authors: Dajun Sang, Tong Shu, Christian F. Pantoja, Alain Ibáñes de Opakua, Markus Zweckstetter, Liam J. Holt.

Author contribution: *D.S. and T.S. undertook all experiments and analysis except NMR, supervised by L.J.H. C.F.P. undertook NMR experiments with analysis help from AIdO, su- pervised by M.Z. All authors contributed to writing and editing the manuscript.*

Table of Contents

List of Figures

Chapter 1: General introduction

1.1 Biomolecular liquid-liquid phase separation and cell biology

1.1.1 What are biomolecular condensates?

The term “biomolecular condensates” has been attributed to the collection of intra-cellular structures lacking membranes [1, 2]. In contrast to canonical organelles, the lack of membrane facilitates molecular transport and provides high flexibility regarding cell stimulus. Intrinsically disordered proteins (IDPs) and nucleic acids are the main components of biomolecular condensates [3, 4]. Their assembly is mediated by multivalent and transitory interactions. They are reported to be present in the cytoplasm, membranes, and even in the nucleus (Figure 1A). The wide diversity of condensates has been associated with their broad functional role.

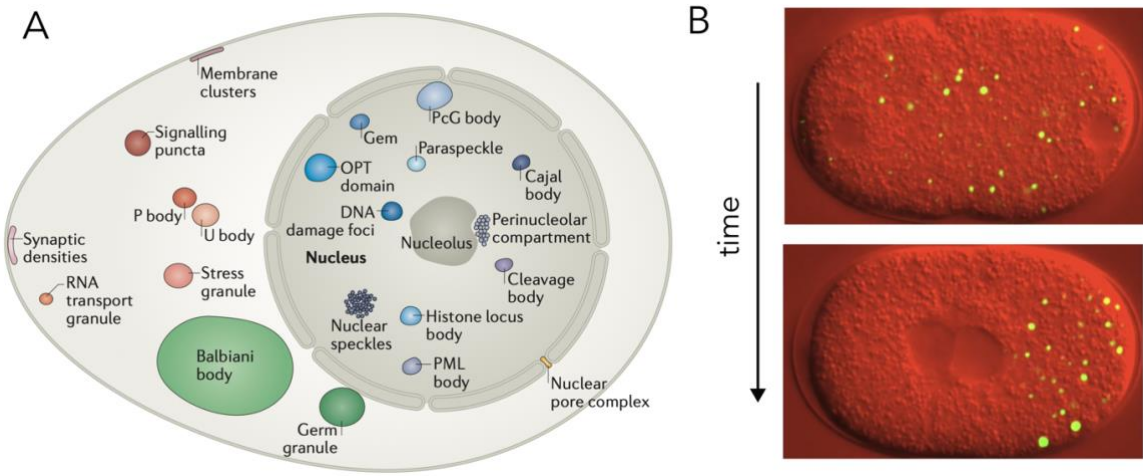

Figure 1. *Description of biomolecular condensates present in the cell and P granules. A) Biomolecular condensates can be found within the cellular environment. B) P granules illustrated in the sensing and colocalization of biomolecular condensates during the cell division of C. Elegans. (Figure adapted from [1, 5])*

Phase separation mediates the formation of biomolecular condensates. This concept is described extensively in thermodynamic and polymer sciences[6, 7]. Minimization of free energy drives the demixing and following assembly of two coexistent phases. The phase diagram indicates the phase separation conditions and coexistent limits of the two phases. Additionally, it reveals the fine balance between entropy and enthalpy contributions associated with the demixing process. Continuous efforts have been dedicated to expanding our thermodynamic description of biomolecular condensates [8]. However, complexity and non-equilibrium conditions in the cell have limited the scope of the current studies.

1.1.1 Primary sequence and forces that regulate biomolecular condensation

Recent studies have provided new ideas regarding the "grammar" of interactions that rule the phase separation of biomolecules[9]. The predominant role played by repetitive or degenerate sequences called "low-complexity domains" has been pointed out. Commonly, these sequences are rich in aromatic residues that allow the formation of intricate networks that stabilize the new phases (Figure 2). Additionally, these sticking interactions are counterbalanced by the presence of flexible segments.

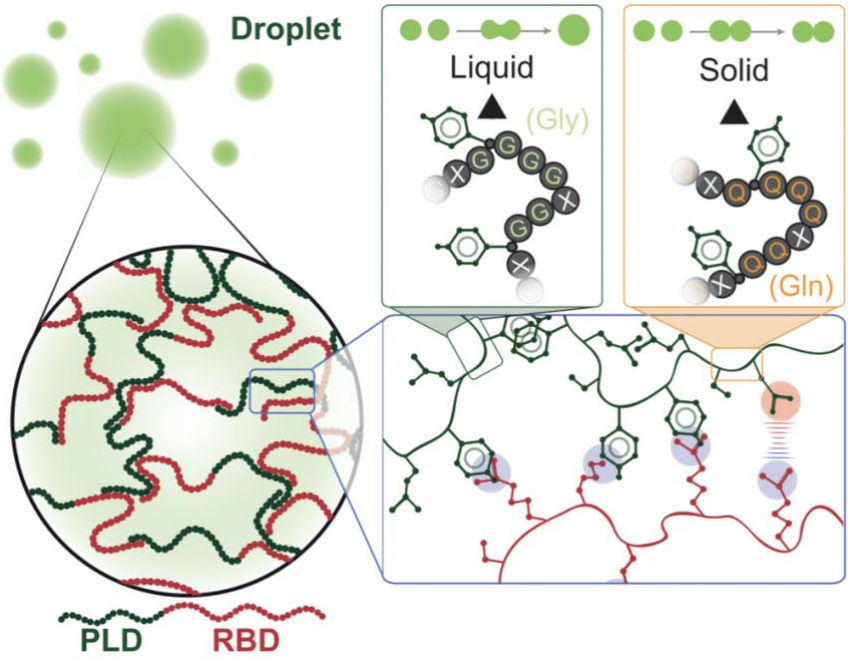

***Figure 2**. Formation of biomolecular condensates (droplet) based on spacer and sticker description. Prion-like domain (PLD) and RNA binding domain (RBD) constitute the aminoacid organization of FUS protein. Associative interactions between aromatic residues determine the phase separation propensity of the protein. Instead, Spacers constituted by residues like glycine, glutamine or serine regulated the material properties of the condensate phase (Figure adapted from [9])*

The complete description is collected in the "spacer and stickers" theory [10]. The ideas behind this theory have been described in the past through to pioneering studies in polymer science [11]. However, not only low-complexity domains can explain the complete driving force behind phase separation, as other very important interactions can play an active role during this process. One of these are the weak and long-distance electrostatic interactions play a significant role in regulating the formation of condensates that involve sequences with high polar amino acid content (Figure 3). For instance, these forces regulate the formation of the more popular RNA-rich condensates that involved polyelectrolyte molecules.

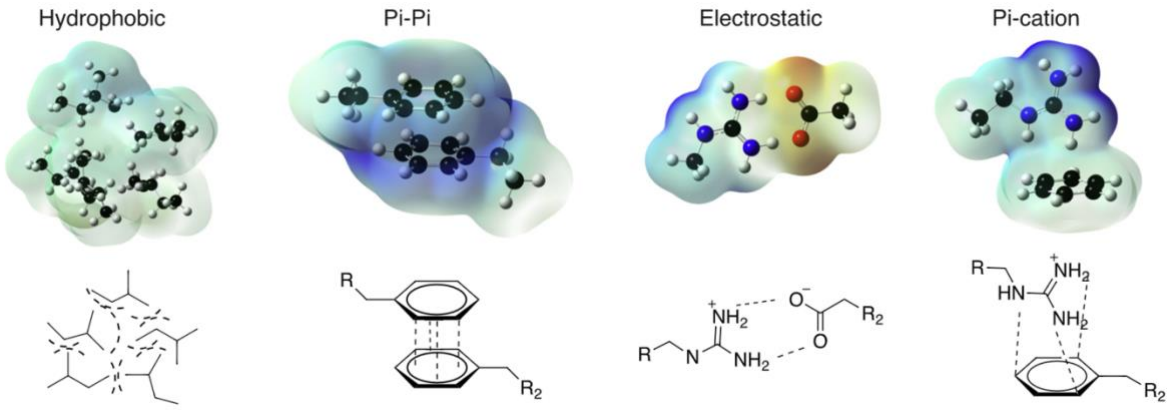

***Figure 3**. Forces that regulated biomolecular condensation. Electrostatic surface potential is illustrated for each participating force. Note that these interactions can also participate in the recruitment process of molecules inside condensates. (Figure adapted from [12])*

1.1.2 Material properties and functional roles

Material properties of condensates are diverse forming liquid, gels and also solid structures[1]. The preference for one state or another has been connected with the primary amino acid sequences. Evidence of the different material properties is well illustrated in the cell. For example, RNA-binding proteins can drive the formation of stress granules in the cytoplasm [13]. These condensates reveal to have liquid-like properties that facilitate the exchange of components with the environment. Another example happens in the nuclear pore where proteins enriched in FG motifs can mediate the formation of gels regulating the transport between the cytoplasm and nucleus[14, 15]. Finally, we can mention the nucleolus whose unique gel-like material properties have fascinated the scientific community for a long time[16].

Summarizing, the formation of biomolecular condensates can be described according to their primary sequence and intermolecular interactions. Nevertheless, the diversity of biomolecules like proteins offers a new layer of complexity motivating multidisciplinary efforts to elucidate the functional and mechanistic role in cell organization.

1.2 Biomolecular condensates implications in function and pathology

1.2.1 Functional role

Biomolecular condensates can be founded abundantly in the intracellular environment. This spread formation suggests a significant role in cell organization and function [17]. Essentially, condensation implies that a specific set of components can localize and increase their local concentration. The selective recruitment or exclusion inside condensates can play a regulatory role in the homeostatic balance in the cell. Additionally, that activity can be modulated by a sensitive stimulus like pH, temperature, and crowding conditions. To provide a useful description, we designate the name of

"scaffold molecules" to those components that constituted the condensate phase, and "client molecules" to those components that are recruited inside the condensate phase. Employing that denotation, we can briefly describe the functional roles associated to scaffold and client molecules.

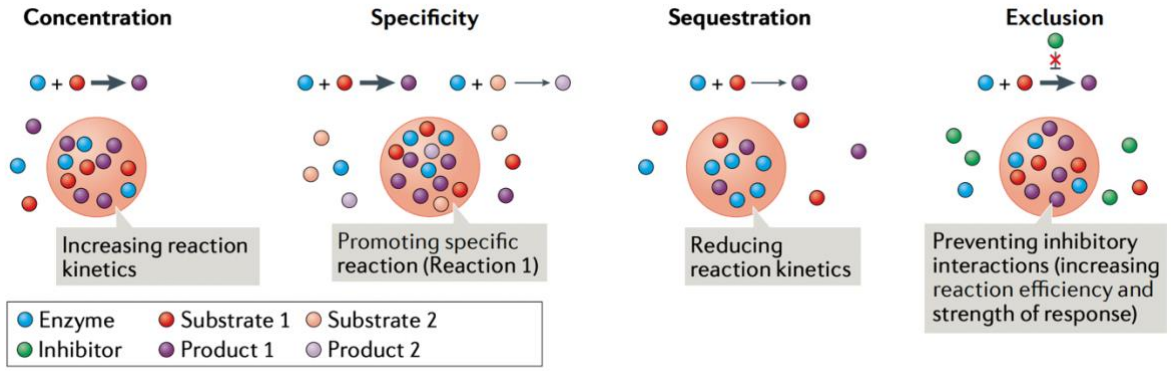

***Figure 4**. Regulation of biochemical reactions mediated by biomolecular condensates.Recruitment or exclusion is essential to understand the implications of condensates in enzymatic activity. Co-recruitment of enzyme and substrate (client molecules) can increase the chemical reaction or promote specificity. Conversely, sequestration or exclusion of substrates can reduce or limit chemical conversion. (Figure adapted from [17])*

The formation and stability of the condensate phase rely on the interactions that scaffold molecules can establish with themselves or additional partners. In that order, the connection between condensate formation and cell stimulus is mediated by the scaffold molecules. Next, the assembling of a new phase can unbalance the chemical potential, inducing the partition of closed components. These components designated as "client molecules" can be macromolecules or small metabolites present in the intracellular environment. Co-recruitment of client molecules has called for a special interest in the potential implications that biomolecular condensates have in enzymatic activity [17, 18]. For example, the recruitment or exclusion of components can act like a switch triggering or inhibiting a particular chemical reaction (Figure 4). A multitude of functions has been associated with biomolecular condensates, another very attractive one is their functional role during gene expression [19]. Recent evidence supports that the low complexity domain of polymerase-II can act as a "scaffold molecule" mediating the recruitment of the transcription factors [20]. However, biomolecular condensates are not only associated to correct cell function, but they are also implicated in different diseases.

1.2.2 Pathological role

The pathological role of condensates is linked to their close connection with disordered proteins. A large number of disordered proteins traditionally involved in diseases have been reported to undergo phase separation [21]. The transition from highly soluble conformations to highly ordered structures has been the research focus to understand the link between disordered proteins and diseases. In that context, the formation of biomolecular condensates is suggested as an intermediate state between functional and pathological forms. The evidence regarding this assessment is supported by the liquid-solid transitions observed for some condensates (Figure 4). For example, the low-complexity FUS can

form condensates that evolve in a process known as “maturation” to form solid-like structures with pathological consequences[22]. In particular, we will focus on another member of this group of proteins that is well-recognized by its pathological role has been recently has been reported to undergo phase separation.

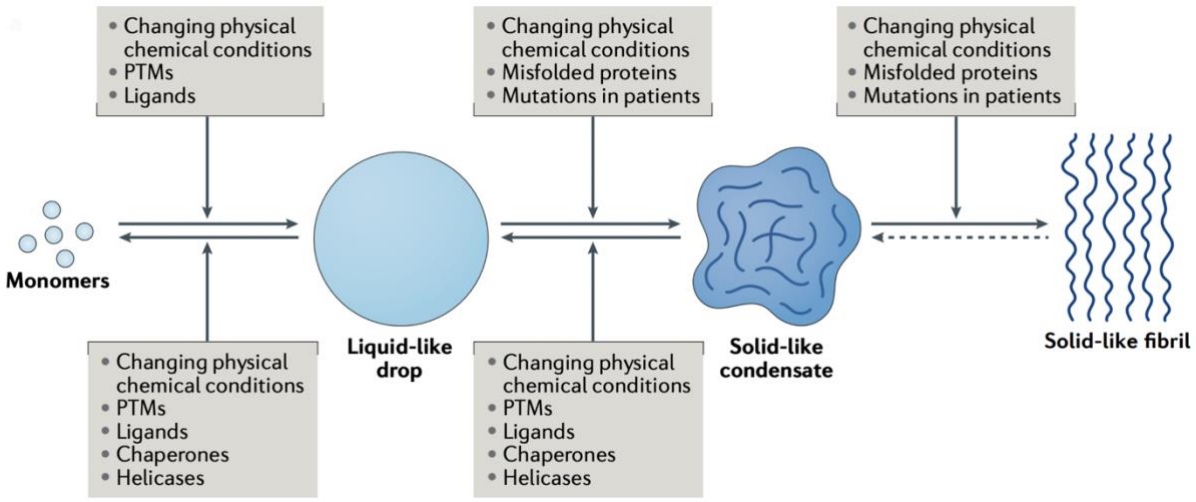

***Figure 5**. Pathological role of biomolecular condensates. Monomers can assemble condensates sensing different physical and chemical factors in the cell. The formation of liquid-like droplets can mature and form solid-like structures. Such structures could play an intermediate role in the formation of rigid and solid-like structures. (Figure adapted from [21]*

1.2.3 Tau protein and phase separation

Microtubule-associated Tau protein (Figure 6) is recognized by its pathological role in the group of diseases known as Tauopathies[23]. Tau protein is expressed in the neurons and its functional role is connected with the stabilization of microtubules[24]. However, under pathological conditions, Tau protein can form insoluble structures with toxic characteristics associated with the development of Alzheimer’s disease. The reasons behind the transition between functional to pathological conformation are still unknown. Recent studies suggest that Tau protein can form condensates under physiological conditions [25, 26]. These condensates have been suggested to act as an intermediate state during the aggregation pathway of Tau protein. One of the aims of the present work is to provide a thermodynamic description of Tau condensates and the driving forces behind their phase separation properties.

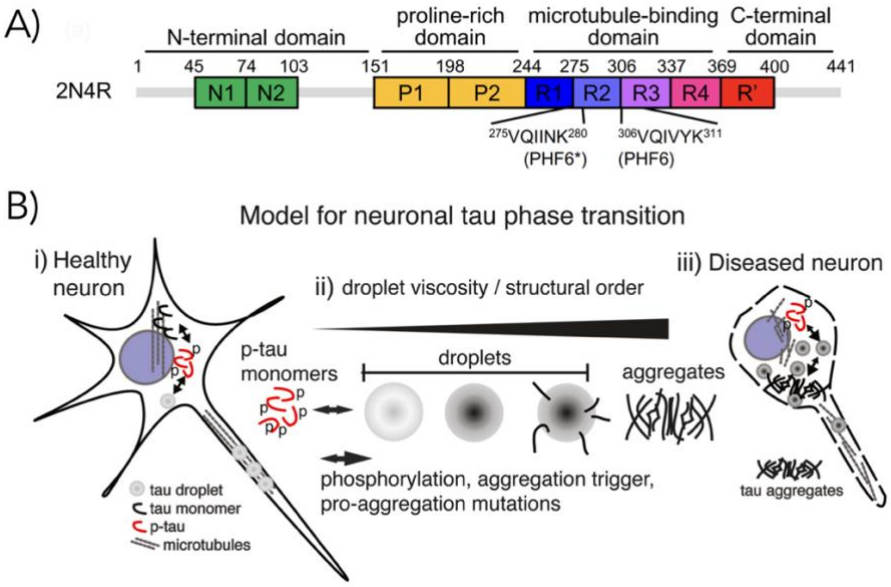

Figure 6*. Tau protein and potential intermediate role of condensates in the aggregation process. A) Domain organization of Tau protein. Microtubule-binding domain contains two hexapeptides (PHF6 /PHF6*) involved in the formation of the fibrillar structures. Tau condensates can promote more extended conformations where both hexapeptides can facilitate the aggregation process[25]. B) Pathological role and maturation of Tau condensates mediated by phosphorylation. Unregulated phosphorylation of Tau protein can drive the maturation of condensates and promote the formation of Tau aggregates[26]. (Figure adapted from [26, 27])*

1.3 Thermodynamic description of phase separation

Phase separation has been extensively studied in polymer science (Appendix 4), and we will now summarize the main concepts useful for the development of the present work. Phase separation means the formation of two or more coexistent phases. This process is accompanied by a non-uniform distribution of components in the system. Constant concentrations are determined once the system reaches a minimum of free energy (Figure 7A). The concentration values of both phases are reported along with a physical variable that modulates the entropy interaction. Commonly, that parameter corresponds to the temperature of the system.

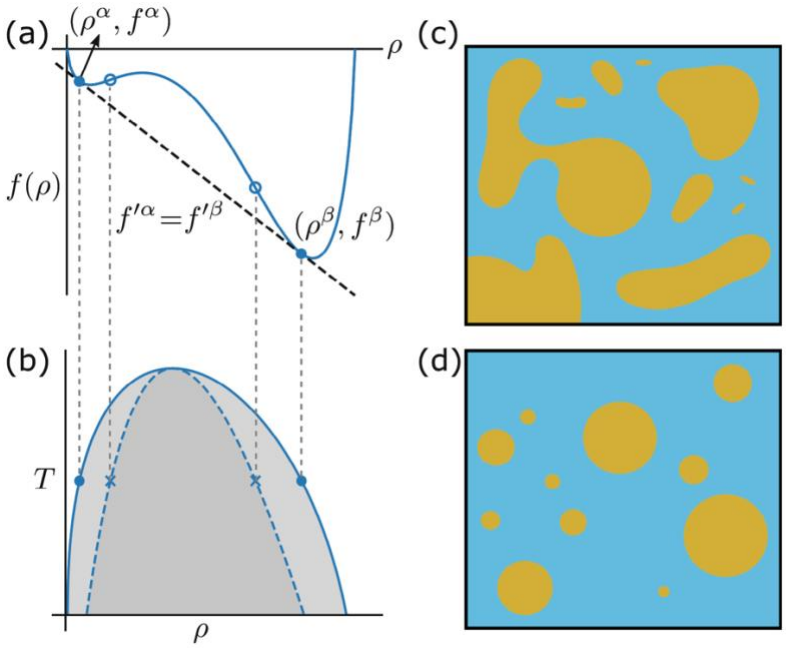

Figure 7. *Phase diagram along with a pictorial description of nucleation and spinodal decomposition. A) Free energy is represented as a function of the temperature. The inflection point represents the minimum of energy corresponding to specific compositions in the coexistent curve. B) The phase diagram is represented by the coexistent and spinodal curves. C) Quenching the system in the unstable region (dark gray) triggered the spontaneous separation of the system recognized as spinodal decomposition. D) Instead Quenching the system in the meta-stable region (light gray) induced the phase separation driven by nucleation process (Figure adapted from [28]).*

We can classify the driving forces behind demixing in terms of interactions between solvent and solute [29]. Taking a polymer chain as an example, predominant interactions between polymer and solvent (solvent-solute) facilitate the formation of a uniform phase. Instead, dominant interactions between polymer-polymer or solvent-solvent can induce the demixing of the system forming two phases. The emerging binary system will bring one phase rich in the polymer and the other depleted. Equilibrium concentrations of the polymer in both phases measured under different temperatures constitute the coexistent curve which describes the phase diagram of the system (Figure 7B).

After the system reaches the two-phase region in the phase diagram, the phase separation process is triggered. Two mechanisms can operate during the demixing process according to temperature and composition. The first mechanism is called spinodal decomposition[30]. The demixing process is initiated without nucleation sites and the conversion of the system into two phases happens spontaneously (Figure 7C). The second mechanism is called nucleation process (Figure 7D). Here, the formation of a new phase is mediated by the formation of nucleation sites where the new phase can start to grow. Then, after the droplet dimension reaches a stable size distribution the energy of the system is minimized forming large droplets and finally a new phase. The difference between both processes is the absence of a thermodynamic barrier to trigger phase separation. Spinodal decomposition is an unstable thermodynamic state in contrast to with the meta-stable nature of the nucleation process. Additionally, spinodal decomposition is carried out uniformly along the sample volume, contrary, to the nucleation mechanism where specific places are involved

1.4 Methods to study biomolecular condensates in vitro

The development of new techniques and strategies to study biomolecular condensates is a prominent topic nowadays [31]. Their dynamic and transitory nature reduces the types of analytical techniques applicable. Nevertheless, an incrementing number of strategies have been developed in the last years to study biomolecular condensates. In this section, we are going to provide a brief overview of the more used and common techniques employed.

1.4.1 Optical methods

Probably, the most extended group corresponds to the optical methods [32]. Microscopy measurements are the initial step to characterize phase-separating systems[31]. The main advantage constitutes the simplicity and the low demand for material needed to provide a quick evaluation of the phase separation conditions. Commonly, this approach is applied along with the use of fluorescent label tags[33]. Labeling the molecule of interest is possible to provide information regarding the recruitment, exclusion, or even approximate concentration values.

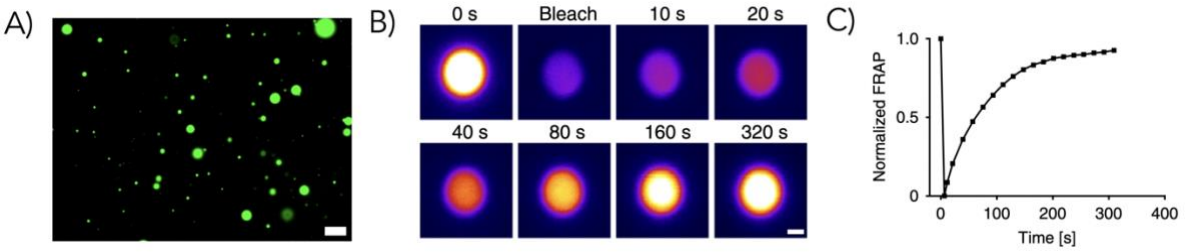

***Figure 8**. Fluorescent microscopy and FRAP measurement of Tau condensates. Phase separation of Tau protein reported by fluorescence microscopy. B) Photobleaching of Tau condensates labeled with green fluorescent protein (GFP). C) FRAP recovery curve reported from Tau condensates. (Figure adapted from [34])*

Another useful technique that uses labeled material is Fluorescent Recovery after Photobleaching (FRAP) [32]. This approach provides information regarding the material properties of the condensate phase. This technique is very valuable following the maturation process (liquid-solid transition) of condensates. Finally, turbidity methods required a limited amount of material, making them suitable for quick evaluation. In contrast with fluorescent microscopy, no labeling is needed. Usually, this approach is combined with a temperature ramp to estimate the temperature transition of the system[35].

1.4.2 Hybrid approaches

These methods constitute the second most extended group to study phase separation in vitro. The collection of hybrid methods includes the combined application of well-established analytical tools. A good example is the determination of critical concentration for the system of interest[36]. Critical concentration corresponds to the maximum concentration of a component in solution before the demixing process initiates. To quantify protein concentration the system is centrifuged allowing to separate both phases. Then, protein concentration can be measured using standard protocols like UV-vis or biochemical assays.

1.4.3 Emerging methods:

We can mention a new set of emerging methods that probably find a large application in the next years. Spectroscopy techniques like Raman microscopy provide a single droplet-level composition of biomolecular condensates [37]. Terahertz spectroscopy has been able to elucidate changes in the solvent inside the condensate phase [38]. Finally, microfluidic strategies have gained more attention regarding limited sample amounts and precise values in reporting phase diagrams [39].

We can extract two conclusions regarding the current methods. First, excluding spectroscopy techniques, the information provided is predominantly qualitative. Second, molecular or residue-specific information is almost absent. In that order, methods capable to study dynamic systems at the residue level are desirable. NMR is a powerful technique able to study dynamic systems and provide information at the atomic level. In the next part, we are going to review the fundamental of NMR basis and the current developments in the NMR field to study biomolecular condensates

1.5 Nuclear magnetic resonance to study biomolecular condensates

1.5.1 Nuclear magnetic resonance

NMR spectroscopy is a technique based on nuclear transitions under high magnetic fields [40]. Shown in (Figure 8), a pictorial description places the nuclear spins orientated randomly in the absence of any magnetic field (Figure 8A). Following, the application of a high magnetic field reveals the polarization of the system creating two different states (Figure 8B). The asymmetric distribution of nuclear spins creates a net magnetization useful to perform the NMR experiment. Applying a transversal magnetic field also known as the radio-frequency field (RF), creates non-equilibrium magnetization (Figure 8C). Turning off the RF field the non-equilibrium magnetization returns to its initial condition reporting an electromagnetic signal called free induction decay (FID). This signal contains information regarding resonance frequencies of the nuclear spin in the time domain (Figure 8D). Converting the temporal signal to the frequency domain using the Fourier transform (FT) allows us to record the common NMR spectrum.

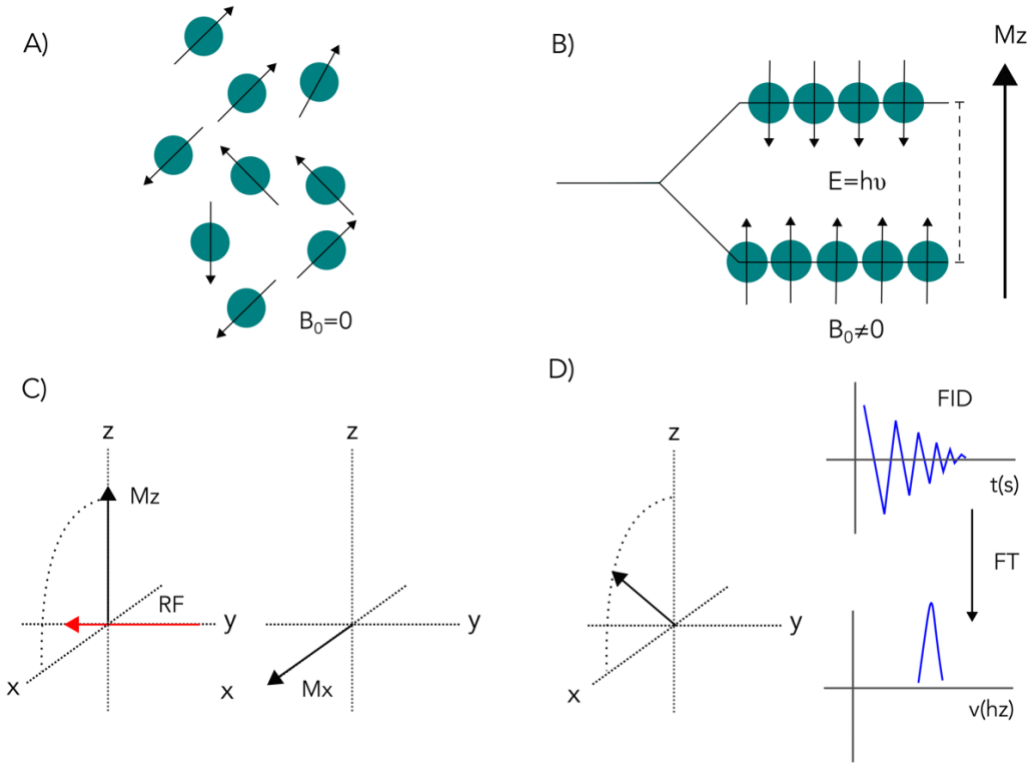

***Figure 9**. An illustrative description of the principles behind NMR spectroscopy. A) In the absence of a magnetic field (B_0=0) nuclear spins are randomly oriented. B) The application of a high magnetic field polarizes the system inducing a difference in nuclear spin populations. C) To create a detectable signal the application of the RF field perturbates the system creating a non-equilibrium magnetization (x-magnetization). D) after turning off the RF field the magnetization returns to equilibrium conditions reporting the FID signal. Fourier transforms the temporal signal and reports the resonance frequency of the nuclei*

1.5.2 Nuclear magnetic resonance and structural elucidation

Before the introduction of the Fourier transforms (FT) by Richard Ernst [41], NMR was recognized as a very insensitive technique with a limited range of applications. However, the improved sensitivity by FT along with technological development enabled the application of NMR to molecular structure elucidation. The small difference in the magnetic environment was an essential tool to determine the number of atoms involved in the structure. The presence of scalar coupling between two active nuclei allows us to connect this chemical environment based on bonding proximity (Figure 10A). Probably, one of the most significant pieces of information detectable is spatial proximity using the Nuclear Overhauser Effect (NOE) [42]. The collective application of these properties allows us to determine the structural information of molecules at atomic level resolution.

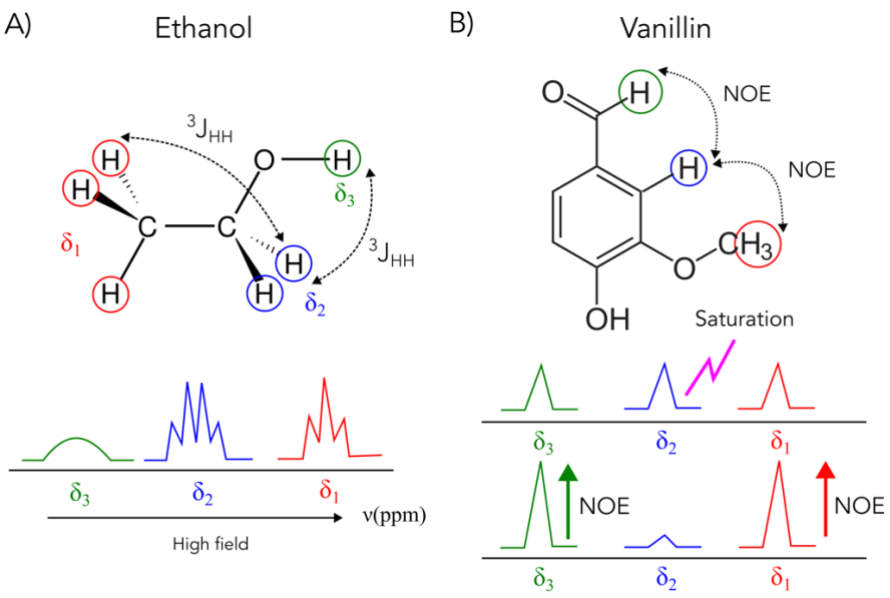

***Figure 10**. Description of the basic sources of information provided by NMR. A) The ethanol molecule illustrates the information contained in the chemical shift and scalar coupling. Close proximity to electronegative species will de-shielding the nuclei reducing the field in which the NMR resonance will appear. That is illustrated by the proton attached to the oxygen atom (green) contrasting with the methyl group (red) in high field values. The second parameter is scalar coupling which allows connecting of atoms through 3 bonds. That information is detectable between the blue and red groups of atoms. B) Illustrative example of NOE information. The Vanillin molecule reflects spatial proximity between the ring proton (blue) and the additional groups (red and green). Saturation by constant irradiation reflects the enhancement of signal caused by NOE.*

Following the success of studying small and simple molecules intense efforts were placed into making NMR applicable to biomolecules. Here, we can mention the pioneering work performed by Kurt Wüthrich and coworkers developing new strategies based on NMR to study peptides and short fragments of nuclei acids [43]. New developments in sensitivity and biochemical engineering have brought new opportunities to NMR to study large systems like proteins.

1.5.3 Nuclear magnetic resonance and biomolecules

The extension of NMR to biomolecules came along with the inclusion of multidimensional NMR and strategies for isotope labeling. According to the molecular weight and complexity of the molecule, increasing the number of NMR resonances make it complicated to interpret the NMR spectrum. Increasing the signal dispersion using multidimensional experiments has been a key point to study large molecules in NMR. To provide a simple description of the main concepts behind multidimensional approaches we will present the main features of two-dimensional experiments. Initially, the system is placed under high field conditions creating observable polarization or active magnetization. That moment is denoted as the preparation period (Figure 9A). Next, the active magnetization is excited by the RF field. This non-equilibrium magnetization can evolve under influence of the magnetic interaction of interest (scalar coupling, dipolar coupling, or chemical shift).

This step is denoted as the evolution period. Following, the information from the initial spin is transferred to the second spin through desired magnetic interaction. That period is recognized as a mixing. In the last part, information is returned to the initial spin to perform the detection of the NMR signal. Applying an FT along both incremental times (t_1, t_2) provides a frequency map where signals are connected through cross peaks in that case in which the magnetic interaction between them is active (Figure 9B).

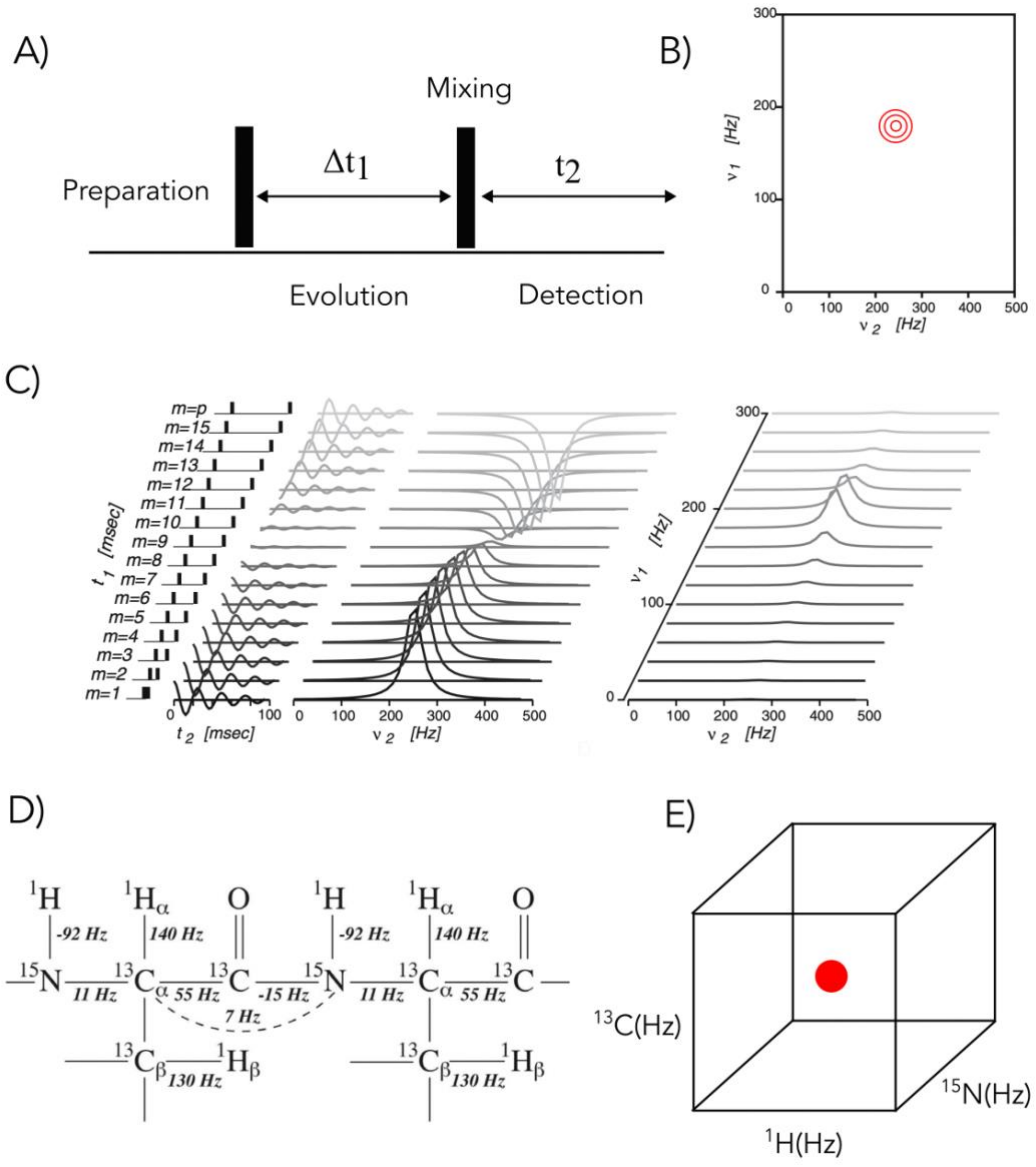

Figure 11. *Multidimensional NMR principles and application to biomolecules. A) Representation of basic elements of multidimensional NMR (preparation, evolution, mixing, and detection). B) Two-dimensional NMR spectrum recording after Fourier transform S(t_1,t_2) signal. C) Time increment and creation of the second dimension. Note that the oscillatory signal is visible after Fourier transform S(t_2). The final representation shows a peak forming between both frequencies involved. D) Heteronuclear scalar coupling present after isotopic labeling protein backbone. Heteronuclear couplings are essential for polarization transfers involved in protein NMR. E) Representation of 3D NMR experiment recorded after additional nuclei are included (^{13}C /^{15}N). (Figure adapted from [44])*

However, two-dimensional experiments cannot provide sufficient dispersion to explore largely and complicate molecules (Figure 11B). Thus, inclusion of heteronuclear experiments was the next step to develop protein NMR. Natural abundances of the isotopes of ^{12}C and ^{14}N present in proteins are not active to perform NMR experiments. Instead, isotopic enrichment of isotopes ^{13}C and ^{15}N using recombinant technologies enables the use of NMR [45]. The availability of additional nuclei increases the dimensionality connecting more than two nuclei along with the substantial increase in resolution (Figure 11D). The parallel developments in isotope label strategies and NMR experiments set the bases for the flourishing expansion of biomolecular NMR.

1.5.4 Nuclear magnetic resonance and dynamics / chemical exchange

Until this point, we have described the potential application of NMR to explore molecular structures. However, NMR is not only restricted to structural analysis it can also provide information relative to motions and dynamics of proteins [46]. Nuclear spin relaxation is the main source of this information. A detailed description of the mechanism involved is beyond the scope of the current introduction.

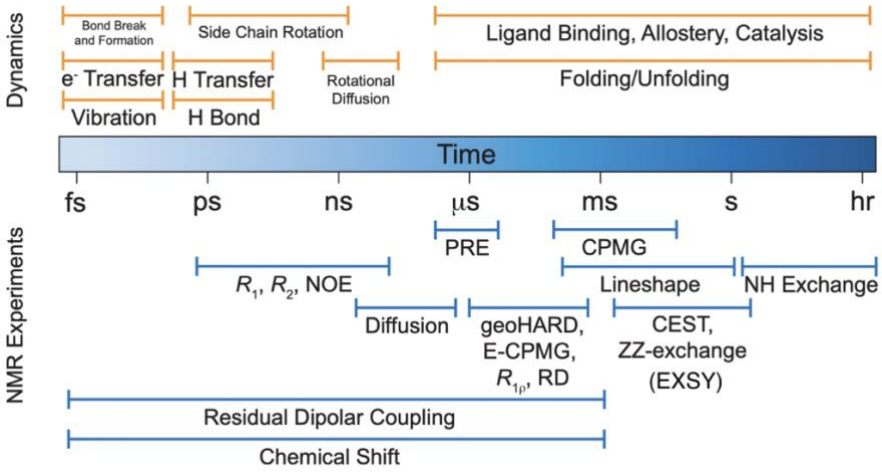

***Figure 12**. Time scales and motions accessible by NMR spectroscopy. The corresponding motions and suitable NMR experiments are represented. (Figure adapted from [47])*

NMR spectroscopy has access to a broad time scale (Figure 12). Such flexibility permits NMR to provide valuable information on biomolecular motions. Additionally, NMR can also provide information regarding another dynamic process called chemical exchange [48]. That process involved the movement of nuclear spin between two different magnetic environments (Figure 13A). According to the exchange rate of the process, we can denote three different time scales. In the fast time scale, interconversion between two states happens so fast that only an average resonance frequency can be detected. Following, interconversion into the intermediate time scale is characterized by strong line broadening in the NMR signals. Finally, a process taking place in the slow time scale creates two defined NMR signals corresponding to both magnetic environments (Figure 13B).

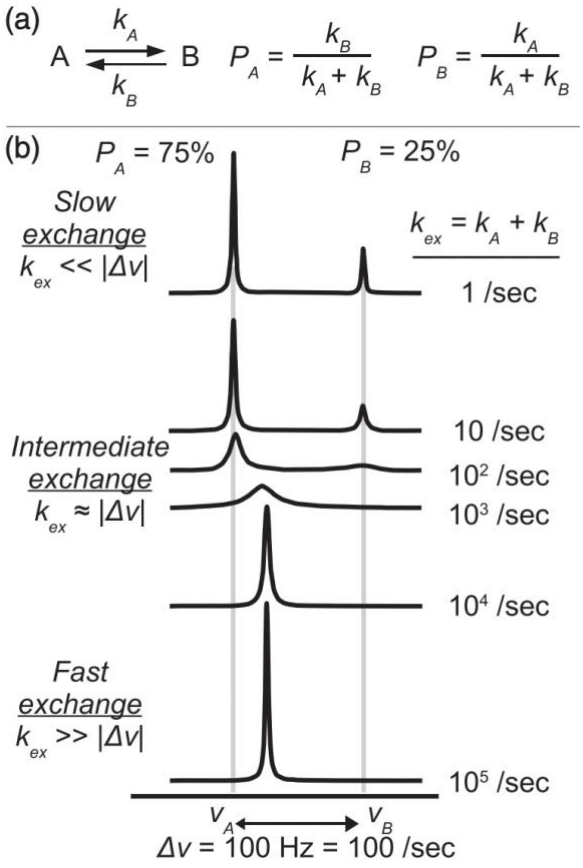

***Figure 13**. Chemical exchange process in NMR spectroscopy. A) Chemical exchange process is characterized by a specific kinetic rate ($K_{ex} = k_a + k_b$) and population of both states. B) According to kinetic rate a specific kind of NMR lineshape is observable. (Figure adapted from [49])*

Summarizing this brief overview of biomolecular NMR, we can highlight that after more than 70 years of study, NMR reaches the point of being a well stablished biophysical technique. Along with the new developments in Cryo-electron microscopy and computational tools, NMR is expected to be crucial explore dynamic biomolecular systems [50] .

1.5.5 Biomolecular condensates and NMR

Biomolecular condensates include two features that make them highly suitable to be studied by NMR spectroscopy. The main feature is that large group of proteins that undergo phase separation are flexible and disordered proteins [3]. Indeed, NMR is widely recognized to be able to report atomic information of proteins that lack structure. Additionally, the high sensitivity for the local chemical environment gives NMR a privileged position to study dynamic and weak interactions. We will mention the most relevant strategies using NMR to study biomolecular condensates at the moment:

1.5.5.1 Intermolecular NOEs

The formation of a new phase is driven by increasing the intermolecular interactions. In the last decade, NMR spectroscopy develops a group of experiments able to study surface interactions for a globular protein. Employing a specific isotopic label skin, NMR spectroscopy can provide information relative to a residue involved in surface interactions[51]. This information is provided by the spatial proximity of two nuclei. The mechanism involves intermolecular NOE [52]. This strategy has been applied with success to several systems like FUS, DDX4, and CAPRIN1[53-55]. Residue-specific information regarding intermolecular contacts has been revealed. Particularly, protein sequences that include a high content of aromatic residues.

1.5.5.2 Paramagnetic relaxation enhancement (PRE)

According to the idea that intermolecular interactions are critical to understanding the forces that drive phase separation. Intermolecular PRE has been applied to elucidate transitory interactions at long distances. Here an active paramagnetic specie is attached to a silent NMR molecule (no isotopic labeling) and its effect is detected by second specie which is active in NMR. In principle, a paramagnetic specie can induce dipolar relaxation at distances that are superior to the proton NOEs. Applying this strategy, intermolecular contacts between chains involved during the phase separation can be detectable. This approach has been applied to a system like FUS and CAPRIN1 with relative success[53, 56].

1.5.5.3 Relaxation measurements

The formation of the condensate phase brings a change in the material properties due to a dramatic increase in protein concentration. These changes can influence both the dynamic and but the conformational assembly of the protein of interest. Nuclear relaxation can provide information regarding the motions and dynamics of the protein [57]. The conventional set of relaxation experiments (R_1, R_2, Heteronuclear NOEs) has been applied to specific cases (FUS and CAPRIN1). Limitations regarding line broadening of the NH signals are the main drawback of this methodology. The current results highlight the increase in the transverse relaxation rates associated with the increase in the viscosity and minimum changes in the fast motion regime[53].

1.5.5.4 Electrical potential and solvent PRE

Probably, the more attractive method is the integration of solvent PRE with the prediction of the near electrical potential of the protein[56]. This strategy can map the electrostatic potential of the protein during the course of the phase separation process. This is the case of the neutralization of the CAPRIN1 during the phase separation mediated by ATP [58]. This methodology promises to be useful to systems that involve polyelectrolytes like RNA molecules.

1.6 Limitations and opportunities to new of developments of NMR to study biomolecular condensates

1.6.1 NMR sample limitations

The complete group of NMR approaches described before share a common limitation. Large sample volumes are required to perform conventional experiments. Indeed, many systems that undergo phase separation cannot produce the required material. In principle, protein production restricts the amount of protein that can be available to perform the experiments. Second, under phase separation conditions, the extension of the condensate phase is less than the volume needed to fill the active volume inside the NMR probe. The active volume could be interpreted as the minimum volume required to obtain a homogeneous magnetic field along the sample. High magnetic field homogeneity is essential to record a high-resolution NMR spectrum. That is especially important in the case of biomolecules. The extension of NMR methods to limited sample volumes can increase the number of systems that can be accessible. Additionally, the observation of a two-phase system can provide simultaneous information on the coexistent phases. which is very valuable regarding the thermodynamic characterization of the system. For example, providing an equilibrium concentration of components is possible to determine the phase diagram of the system of interest.

1.6.2 Droplet formation

A main feature of the phase separation process is the formation of small droplets. These microscopic condensates are the first indication that the system can undergo a phase transition. Sample heterogeneity constitutes the main factor behind the low number of studies that involve droplets and high-resolution NMR [59]. Additionally, droplet formation constitutes a meta-stable state that decays during the time of assembling a new phase. The time-dependent feature restricts the number of NMR experiments applicable. In the case of biomolecules, the application of multidimensional NMR is time demanding and sample stability is a key factor. Nevertheless, the study of droplet formation and its dynamic nature have a significant implication in the context of biomolecular condensates [18]. For example, the trafficking or exchange of components with the environment is a key functional feature. Indeed, drug targeting of condensates using small molecules depends on quick exchange and recruitment inside the condensate phase[60].

1.6.3 Composition, recruitment and thermodynamic characterization of biomolecular condensates using NMR

Despite that composition is essential to understand the phase separation of biomolecules, limited information is available regarding concentration and global composition. Indeed, the significant concentration difference between the diluted and condensate phases makes challenging the application of a single technique. The main source of information regarding concentration is provided by fluorescent microscopy or hybrid methods that independently quantify each phase[36]. Quantification is predominantly qualitative in part because of the exhausting calibration process or complications during sample preparations. New methods capable to quantify protein concentration inside condensates are desirable.

Establishing a clear connection between thermodynamic description and biology can help us to elucidate the forces that rule biomolecular condensates. Providing precise and feasible information is critical to developing new models and validating previous ones. Precise quantification of protein and additional components under equilibrium conditions can constitute a first step. Nevertheless, sample volume and spectral quality under phase separation conditions should be addressed.

Recruitment and exclusion are representative features of biomolecular condensates. Providing information regarding molecules that are enriched or depleted is a key point behind understanding their biological function. Indeed, NMR can provide information on client molecules in label-free mode. That is especially useful in the context of small molecules where the addition of tag molecules could affect their chemistry

1.6.4 Quantification and real-time monitoring of chemical reactions mediated inside condensates

1.6.4.1 Chemical reactions and biomolecular condensates

Regulation of biochemical processes has been connected to a role played by biomolecular condensates[1]. Co-recruitment of enzymes and substrates is supposed to enhance enzymatic activity by increasing local concentration. Several studies highlight the important role played by the law of mass action [17]. However, recent evidence suggests that improvements achieved by condensates could involve multiple factors beyond the law of mass action [61]. Structural features along with multivalent interactions between scaffold and client molecules can also modulate the enzymatic activity. This evidence stresses that a complete description should include a mechanistic description of the potential interactions between components inside condensates.

A limited number of methods can provide experimental information regarding chemical reactions inside condensates. A standard protocol involves Western blot gels reporting mobility changes associated with chemical modifications [62]. However, access to residue specifics is still challenging. To provide a complete description of the enzymatic activity techniques with accessibility to residue level information are desirable. NMR spectroscopy can provide an atomic description but also evaluate interactions involved during the catalytic activity.

Along with access to flexible and dynamic systems NMR can provide real-time information on chemical reactions [63]. Chemical modification induces changes in the local magnetic environment. These modifications are reported by changes in the linewidth and intensity. Following such events during the chemical conversion can provide a kinetic and mechanistic description. The potential to monitor the chemical reactions of biomolecules by NMR has been demonstrated in the past. However, application to monitoring chemical reactions inside condensates has not been reported before. We expect that the adaptation of NMR to study chemical reactions inside condensates could offer a mechanistic description of the mediated enzymatic activity.

1.7 Aims of this study

The dynamic and transitory nature of biomolecular condensates plays an essential role as a functional part of cell machinery. However, their intrinsic dynamic nature makes them very difficult to study using the most popular biophysical techniques. NMR spectroscopy offers a reliable alternative to studying transitory and dynamic systems. We expect that the expansion of the NMR capabilities to study condensates will play a significant role in their study. The potential applicability of NMR under very demanding conditions are illustrated in the present work.

In manuscript one, a detailed description of the phase separation phenomenon is presented for a model system. NMR reveals that chemical exchange between nucleation sites (droplets) and solution can be quantified under demixing conditions. Applying integrative tools, exchange of client molecule was detected between both phases. In that order, we suggest that our present results motivated the extension of our present approach to study more complicated systems that involve biomolecules. Additionally, the present approach paves of way to improve the characterization of the droplet conditions, revealing the potential information that can be extracted using NMR spectroscopy.

In manuscript two, a two-phase system that includes Tau protein along with multiple components was analyzed. We record high-resolution NMR data of the phase-separated system using spatially resolved NMR, monitoring and reporting the concentration of the components present. Our current results highlight that multicomponent quantification is accessible and reliable using this approach. Additionally, information regarding kinetics and equilibrium concentration was achievable for Tau condensates reporting the first quantitative phase diagram of Tau protein.

In manuscript three, we demonstrate that NMR can monitor chemical reactions inside condensates in a real-time mode. Using a suitable sample setup, we were able to measure the accelerated phosphorylation process inside Tau condensates mediated by the kinase CDK2. The present finding highlights the potential role that NMR can play in reporting biochemical reactions inside condensates.

In summary, the global aim of the present work is to demonstrate the crucial role that NMR can play in the study of biomolecular condensates. From providing a detailed description of the phase separation mechanism to real-time monitoring of chemical reactions inside condensates, we expect that the present results motivate future works regarding new applications and the expansion of the methods here presented. We expect that our contribution has provided a new avenue to study biomolecular condensates by applying high-resolution NMR spectroscopy.

Chapter 2: General discussion

2.1 Manuscript 1

NMR spectroscopy can describe the droplet formation during the phase separation process

To uncover the complexity behind the study of the phase separation phenomenon by NMR we choose a simple and well-established model system. The triethylamine/water (TEA/H_2O) model is a classic example of a binary mixture that can undergo phase separation driven by entropy contributions [64]. Given that phase separation of the TEA/H_2O system can be triggered by temperature, we exploit the precise temperature control offered by NMR probes to control the desired moment when the system starts demixing. The formation of the new phase reveals interesting features from the NMR perspective. We observed that after quenching the system in the two-phase region, the NMR signals of the TEA molecules experience strong line broadening. In the NMR context, the signal broadening could be interpreted as contributions of the chemical exchange or non-homogeneous line broadening. According to the time scale of the chemical exchange process, we can expect an influence on the linewidth of the NMR signal [65]. Additionally, the formation of small nucleation sites can induce a magnetic susceptibility interruption through the sample [66]. The current results show that the chemical exchange process between both phases happens on the slow time scale regime (k_{ex} ~30 s^{-1}), excluding the potential contribution of the linewidth broadening. Indeed, we can suggest that the significant broadening corresponds to the susceptibility's interruption associated with the emerging new phase. Susceptibility effects have been well described in the literature of heterogeneous systems studied by NMR [67]. For example, systems where molecules can interact with surfaces and restricted space inside colloidal systems [68]. Such effects have even been observed on water molecules recruited inside cell compartments [69]. The present results offer a comprehensive view of the droplet formation during the phase separation from an NMR perspective.

Information encoding in the NMR signals provide a complementary description of the kinetic process during phase separation

Exploiting the high sensitivity offered by the TEA molecule, we used a ^{13}C-NMR to monitor the complete kinetics events during the demixing process. The superior signal dispersion of ^{13}C resonances allows us to separate the two chemical environments formed after the beginning of the phase separation process. Using a complementary approach between NMR peak height and area, we provide a unique characterization of the three stages during the demixing process:

During the early stage (I), our results suggest the formation of nucleation sites (spherical droplets) followed by changes in the average radius impacting the linewidth (peak height) but not the signal intensity (peak area) in a time-dependent manner. This explained by the susceptibility dependency on the radius of spherical droplets[66]. Additionally, it could be explained in a classical nucleation process where the radius of the emerging phase increases according to the surface energy balance reaching a stable average radius before merging [30]. Peak height and area remain invariable during that period (II). At the same time, the formation of a new phase is accompanied by chemical exchange of molecules between the surface of the nucleation site and the solution matrix in the slow time scale.

In the late stage (III), smaller droplets merged into large ones driving the sedimentation of the new phase. This can be followed by the decay in the TEA signal intensity inside the condensate phase. The susceptibility disruption induced by the formation of nucleation sites and the kinetic process imposes a significant obstacle to applying more sophisticated NMR experiments, which is the case in the context of biomolecular NMR. Nevertheless, the pioneering work presented here provides the initial bases that will allow us to design new NMR strategies suitable for biological systems.

Exchange spectroscopy (EXSY) detects a unique chemical exchange between the condensate and dispersed phase

The chemical exchange process is a physical phenomenon that operates a short distance at the atomic level [70]. We suggest that if the chemical exchange mechanism is active between both phases, it should take place on a slow time scale, assuming the distance between the droplet surface and solution is in the order of molecular size. To evaluate our hypothesis, we selected a set of NMR experiments (^{1}H-^{13}C HSQC-NOESY/ ^{1}H-^{1}H-NOESY) suitable to exploring this time regime. Given that such experiments are time-demanding, we used heating/cooling cycling to exploit the reversibility of the process and ensure identical initial conditions for each mixing time [71]. The appearance of cross peaks between TEA molecules in both phases suggested a chemical exchange process between the droplet surface and solution.

Next, to verify the exchange nature of the cross peak observed, we record a complementary approach using ^{1}H-^{1}H NOESY and ^{1}H-^{1}H ROESY. Cross-peak reported by NOESY can be explained by dipolar coupling interaction or by chemical exchange. According to the correlation time dipolar coupling interaction can show positive or negative phase [72]. In the case of small molecules like TEA, the cross-peak is expected to be negative with respect to the diagonal peaks. However, we observe a positive peak with respect to the diagonal peak suggesting an active chemical exchange process. To double-check, we recorded the ^{1}H-^{1}H ROESY experiment. Independently of the correlation time, a cross-peak with a negative phase is expected for dipolar interaction. Again, a positive peak between signals belonging to both phases confirmed the chemical exchange nature of the cross peak detected in the previous experiments. The presented evidence supports the presence of chemical exchange process between the nucleation site and solution during the formation of the new phase. As well, these findings opens new avenues to employ more sophisticated NMR methods in the slow time scale regime to study low-populated states [73, 74] that could be involved in the early formation of the new phase.

Chemical exchange of client molecules can be quantified using ^{19}F-NMR

The observation of the chemical exchange between both phases underlines the versatility of NMR regarding the exploration of exchange components during the phase separation process. In the biomolecular condensate context, molecule trafficking, recruitment, and exclusion play an essential role [1]. The present work paves the way to develop new and more sophisticated techniques dedicated to exploring this exchange process.

To support our assessment, we proposed to study a client molecule that can be partitioned inside the condensate phase during the phase separation process. We choose a candidate able to provide a good

performance regarding sensitivity and simplicity. The hexafluoroisopropanol (HFIP) contains two equivalent CF_3 groups that guarantee the required properties. Using heating/cooling cycling we quantified the inter-phase chemical exchange using the ^{19}F-^{19}F-NOESY experiment. The measured exchange constant (k_{ex} ~16 s^{-1}) reflected a similar magnitude order to TEA molecules (10^1 s^{-1}), suggesting that motion between interphase and solution is potentially dominated by surface properties.

The increasing interest in the functional role played by biomolecular condensates regarding the enzymatic activity or drug targeting by small molecules places the present study in a privileged position. Label-free client molecules could be studied according to their partition, and also the dynamic exchange process between both phases. In light of our findings, we can claim that our approach achieves a valuable description of the phase separation process from the NMR perspective and create new opportunities to expand their applicability to biological systems.

2.2 Manuscript 2

An improved spatially resolved NMR experiment expand the study of biomolecular condensates

The formation of a new phase creates a non-uniform distribution of material along the space. Sample heterogeneity generates challenging problems regarding NMR studies. Magnetic susceptibility differences and asymmetric concentrations between both phases make it complicated to separate contributions from low and high concentrate phases. To provide a feasible solution, we designed a strategy applicable to the limited material amount (protein quantity) and non-uniform samples. Spatially-resolved NMR methods can access limited sample volumes and provide high-resolution information[75]. Nevertheless, applications to biomolecular NMR are rare. To make spatially resolved NMR suitable to study phase separation of biomolecules, we adapted the existent version DPFGSE sequence [76], including the versatile water suppression block WET [77].

To demonstrate the applicability of our method, we induced the phase separation of Tau protein using the crowding agent dextran. After centrifugation and thermal stability, the sample reaches equilibrium conditions forming a binary system. Following, the sample was located inside a coaxial-NMR sample setup allowing to evaluate sample temperature and access to the bottom part of the inner tube, which is crucial to ensure accessibility in systems where a limited amount of protein or extension of the condensate phase is restrictive.

Applying the WET-DPFGSE experiment, we recorded high-resolution 1H-NMR spectra corresponding to both phases. A quick overview revealed that Tau protein is accumulated in the bottom phase along with the crowding agent enriched in the upper phase. Observation of different distributions of buffer components was also detected. Taking advantage of the high sensitivity offered by ^1H NMR, the present method promises to be applicable to a large group of biomolecular systems that undergo phase separation. Overcoming sample limitations and using a no isotopic label material, this strategy could be applied to multicomponent systems under high-resolution conditions including the participation of small and large molecules in a label-free mode.

Multicomponent quantification of phase-separated samples is achievable using spatially resolved NMR

The formation of biomolecular condensates usually involves more than one component. Under cellular conditions, the fine balance between environment and partner interactions regulates the phase separation conditions. Participation of the different components is a crucial aspect to understand the precise factors controlling the biological function of condensates. The dominant technique that can provide information on more than one component is fluorescent microscopy[31]. By adding a fluorescent tag to the target molecule, this technique has provided reliable information regarding the recruitment and phase separation properties of biomolecules. However, expansion to multi-component systems that include small molecules can be a very complicated task. If adding a tag molecule to a macromolecule-like protein has a minimum influence on its normal behavior, adding a bulky group to a small molecule could dramatically modify its chemistry. Here is where the present methodology can play a significant role. The adaptation of the PULCON[78] strategy to spatially resolved NMR allows us to quantify not only small components, but also large molecules like proteins. Using an external reference sample, we report the concentration of the buffer components along with the macromolecule composition in both phases. At the same time, we modified the 1D spin echo imaging (z-profile experiment) to be able to determine the relative amount of water remaining in the protein-rich phase suggesting a reduction of ~19% compared to the uniform sample. Collecting the present results, we point out that this quantification strategy can be applied to multi-component systems that include small molecules and macromolecules, including quantitative recruitment values of client molecules such as metabolites or drugs.

The kinetics of demixing and phase diagram of biomolecules can be measured using spatially resolved NMR

The thermodynamic description is essential to understand the driving forces behind biomolecular condensation. According to theory, the demixing is driven by the nucleation mechanism or spinodal decomposition[30]. After chemical potentials are equalized, two coexistent phases are formed. Monitoring the phase transition and establishing the equilibrium conditions are essential to provide a comprehensive description of the system. Using equilibrium concentrations, it is possible to construct the corresponding phase diagram. The more popular methods (microscopy, turbidity, DLS, etc.) offer qualitative information on the kinetic events and concentrations. Recently, new strategies that include HPLC, microfluidics, and hybrid methods have been proposed to measure phase diagrams [79-81]. Spatially resolved NMR not only provides access to equilibrium concentrations, but transitory events are also detectable. For example, the entropy-driven nucleation of water in the protein-rich phase can be detected and quantified. This highlights the property that NMR has in reporting information regarding the solvent. Additionally, reliable protein concentration can be measured in regimes with strong concentration differences. Using our present methodology, we report the first quantitative phase diagram of the Tau protein and a mechanistic description of its kinetic process. Finally, we expect the information reported will extend our understanding and thermodynamic description of biomolecular condensation.

2.3 Manuscript 3

New dynamic phosphorylation networks between kinases and substrates are created inside condensates

Under in vivo conditions, multi-site phosphorylation was observed on ELK1 catalyzed by MAPK3. The increasing phosphorylation levels for minority sites reveal a crucial property inside condensates. Notably, the close and distant evolutionary enzymes were able to phosphorylate ELK1 after co-recruitment inside condensate. Relaxing specificity is a key feature used to create new links in cell signaling. The correct timing between activity and recruitment of CDK1 using the nuclear reporter NLS-2XWW-GFP underline the dynamic role of biomolecular condensates during the cell cycle. Collecting the current findings, we can highlight the dynamic role that phase separation can have in regulating and expanding cell signaling. Additionally, the present results highlight the pivotal role played by synthetic biology in order to disentangle the complex network in the cell regulation mediated by biomolecular condensates.

Hyperphosphorylation inside in vivo condensates is dominated by multiple factors (e.g., client concentration and binding kinetics)

Recent reports highlight client concentration as a crucial factor regulating enzymatic activity inside condensates [17]. Strong recruitment of substrate and enzyme should accelerate the chemical reaction following the law of mass-action. However, we hypothesize that alternative mechanisms could influence the efficiency of the biochemical reaction. We suggest that binding events between the client and scaffold molecules could play a significant role during enzymatic reactions mediated by condensates. To evaluate our hypothesis, we designed a SIM tag mutant (SIM^{I9P}) able to reduce the binding affinity by the SUMO domains in the condensate phase. Significantly, we found that expression of the mutant ELK1-SIM^{I9P} reduces its recruitment in the condensate phase along with a reduction in the phosphorylation level. The simplest explanation is a reduction of substrate (ELK1) availability in the condensate phase. Increasing the expression levels of the mutant ELK1-SIM^{I9P} can match the concentration of ELK1-SIMWT inside the condensate phase.

However, the phosphorylation level was still 2-fold less compared to the ELK1-SIM^{WT}. These results highlight the complementary role played by binding kinetics in the regulation of the enzymatic activities in the condensate phase. Not only the recruitment of the client molecule determines the efficiency of the chemical reaction that takes place inside the condensate, the binding affinity between the scaffold and client molecule also plays an important role. Probably, stabilizing the substrate conformation improved the enzymatic activity. We propose that enhancement of the biochemical reactions inside condensates should obey multi-factor parameters beyond the law of mass-action already highlighted in the current literature.

Condensate scaffold flexibility is crucial for hyperphosphorylation

Multivalent and transitory interactions have been associated with the formation of biomolecular condensates [1]. Mostly, these weak interactions are formed by flexible chains capable to access a large conformational space. That is the case for flexible scaffolds like SUMO-SIM polymer. However,

biomolecular condensates can also be formed by well-defined structured scaffold molecules [82]. To evaluate the implications of chain flexibility of the scaffold molecule regarding the enzymatic activity, we prepared a well-ordered system that includes two rigid structures. The first structure consists of a homo-hexamer and the second one is a homo-dimer domain from the TRIM25 protein. The last component was fused with two SUMO domains at both extremes capable to drive the recruitment of the SIM-labeled clients. We observed that after expressing the MAPK3-SIM and the substrate ELK1-SIM a comparative recruitment of the client molecules can be reached in the flexible $SUMO_{10}$-SIM_6 condensates. Notably, we observed a dramatic reduction in the phosphorylation level of 10-fold compared to $SUMO_{10}$-SIM_6 condensates. To dissect the potential contribution of the number of binding sites we prepared a 2XSUMO and 3XSUMO construct of our rigid homodimer and we analyze the phosphorylation level of ELK1-SIM under this condition. We observed that phosphorylation levels were almost invariable regarding the increase in the number of binding sites suggesting limited participation in the reduce enzymatic activity. Additionally, we modified the affinity between both components two evaluate the potential implications of the material properties on the activity. Here, we observed a modest increment of 2-fold in the phosphorylation levels when the high-affinity version of two scaffolds was used. Nevertheless, the present results suggest a limited participation of the material properties in the enzymatic activity when a well-structured scaffold constituted the condensate phase. This remarkable finding underlines the broad number of cases where flexible components like IDPs play a role as a scaffold of biomolecular condensates. Summarizing, the large set of conformations adopted by flexible chains can stabilize the condensate phase and also enhanced the performance of biochemical reactions inside.

Synthetic condensed-phase signaling can respond to osmotic compression mediated by macromolecular crowding

Several factors can impact the homeostatic balance during the cell cycle. Osmotic stress is a good example that can affect cell size and increase the macromolecular crowding in the cytoplasm [83]. Additionally, implications in the biomolecular condensates have been reported [84]. To evaluate the effects caused by this factor on phosphorylation levels of ELK1, we tested our synthetic SUMO10-SIM6 system under conditions of osmotic stress. Initial results reveal a 35% reduction of the condensate area along with a 70% increment of enzyme recruitment. Additionally, phosphorylation levels increase by 10% compared to the control experiment. A plausible explanation suggests that under a higher efficient SUMO10-SIM6 system, the chemical reaction already reaches saturation levels. To evaluate the potential effect on a less efficient system, we prepared a SUMO7-SIM6 condensate under identical stress conditions. We observed a similar area reduction and enzyme recruitment compared to the SUMO10-SIM6 system but a 2-fold increment in the phosphorylation level on the ELK1. Our results suggest that osmotic stress can influence the enzymatic activity mediated by the condensates. To elucidate the implications of scaffold flexibility regarding the osmotic stress, we replicated our present experiment using the two-component rigid system. Here, we observed a 10% reduction in condensate area with a 60% increment of enzymatic recruitment. Contrary, to the flexible condensate SUMO7-SIM6, we detected a reduction in the phosphorylation level of 50% on the ELK1.

The negative impact of rigid structures on enzymatic activity reinforces the idea that flexible scaffolds can play a broader role in regulating and tunning cellular signaling. Finally, to disentangle the driving force behind osmotic stress, we explored the implications of molecular crowding in the recruitment

of MAPK3 and reduction in the condensate area. A strategy based on ribosome concentration was employed to regulate molecular crowding. Ribosomes constitute the principal mesostructured able to modulate molecular crowding in the cytoplasm[85]. Increasing the concentration of ribosomes, we observed a monotonic increment in the recruitment of MAPK3 inside SUMO7-SIM6 condensate. Contrary, a negative correlation between the reduction of the condensate area and the increase in molecular crowding was observed. This evidence suggests that macromolecular crowding drives the enzymatic recruitment inside the $SUMO_7$-SIM_6 condensate with increasing enzymatic activity observed under stress conditions. Collecting the current results, we can highlight the role played by macromolecular crowding along with condensate-phase signaling. Additionally, a balance between scaffold flexibility and molecular crowding impact significantly the enzymatic activity mediated by biomolecular condensates.

Phosphorylation of the Alzheimer's disease protein Tau is accelerated in condensates

Synthetic condensates are valuables to simplify the complexity behind the enzymatic activity under *in vivo* and *in vitro* conditions. Nevertheless, a study of endogenous condensates is essential to validate and complement the current findings. To provide a good example, we selected the microtubule-associate Tau protein[24]. According to recent evidence, Tau protein can undergo phase separation assembling liquid-like condensates that could promote the formation of fibrillar structures [25, 26]. The phosphorylation of Tau protein is an essential mechanism that regulates its biological pathological role [86]. To evaluate the potential enzymatic activity inside Tau condensates, we selected CDK2/Cyclin A1 kinase. Using NMR spectroscopy, we quantified the phosphorylation rate of Tau protein in the condensate and uniform phase. To ensure the recruitment of CDK2/Cyclin A1 inside Tau condensate fluorescent microscopy was used. Our data showed a 10-fold enzyme enrichment inside Tau condensate. The kinetic quantification of the residues S199 and T205 suggest an increment in the phosphorylation rates of 3.8-fold and 2.6-fold respectively. Even if the law of mass action can explain the acceleration observed, establishing the enhancement order is crucial information to describe their biological relevance. Finally, we can highlight the unique property of NMR spectroscopy to monitor real-time phosphorylation processes at the residue level. Additionally, conformational changes or binding events could also be detected during the process. Despite the intrinsic signal broadening under condensate conditions, new developments in NMR spectroscopy promise to ensure sufficient spectral quality to access the minority phosphorylation sites. The present results underline the significant role that NMR spectroscopy can play in expanding our understanding of the kinetic process inside biomolecular condensates at the atomic level.

Chapter 3: Summary and outlook

The phase separation field of biomolecules is growing and becoming more diverse. From biochemical regulation to pathological roles, condensates have brought new answers and questions. We expect the field to maintain its growth in the coming years with the joint participation of multidisciplinary efforts. Including the development of new and more sophisticated methods to unravel the principles operating behind these intriguing molecular assemblies.

The application of NMR spectroscopy to study biomolecular condensates is still in development. To illustrate this statement, we have shown in the present work that the chemical exchange process between droplets and solution is detectable by NMR. An extension to study the exchange process that involves client molecules was also described. We expect that the current results can find a broad application regarding the dynamic exchange of small components regulating the condensate's function. For example, drug targeting of condensates is an emerging field that could benefit from the current findings.

Spatially resolved NMR demonstrated its potential to study phase-separated samples. Removing the obscuring contribution of the water signal, the presented method was able to characterize and quantify the two-phase system of Tau protein. Providing multicomponent quantification in a label-free fashion. The current results can open new alternatives to monitoring the co-recruitment effects during the multicomponent partition. Additionally, a new strategy to ensure equilibrium concentration can open opportunities to provide reliable thermodynamic information to improve and validate the current computational model to study biomolecular condensates.

Finally, we demonstrated the potential of NMR to study real-time chemical reactions in condensates. Using Tau protein as a model system, the phosphorylation process involving the kinase CDK2 reflects an increment in the detecting phosphorylation rate in presence of Tau condensates. Additionally, our method offers an alternative to studying transitory interactions between substrates and protein molecules during the chemical reaction. However, limitations such as line broadening should be addressed first for example using perdeuterated strategies to increase sensitivity and resolution.

To conclude, this work expands the borders of the applicability of NMR to study biomolecular condensates. We show unique inter-phase chemical exchange along with the detailed description of the demixing process. We demonstrated the high flexibility that NMR offers in adapting to study restricted sample volumes and quantifying a multi-component system. Finally, we have shown that chemical reactions can be monitored inside condensates at the atomic level using NMR. We expect that our present findings have expanded the applicability of NMR and our knowledge regarding phase separation mechanisms and biomolecular condensates.

Chapter 4: Appendix

4.1 Appendix 1

4.1.1 Thermodynamics of polymer solutions

When polymer molecules are present in solution, they introduce large deviations in the solution ideality. To understand the principles of the phase separation phenomenon for polymers, a primary set of thermodynamic concepts should be introduced. The first step is a clear definition of the thermodynamic properties that define the formation of a solution. The free energy of mixing ΔG_m is properly defined as follows [87]:

$$\Delta G_m = G_{12} - (G_1 + G_2) \quad \text{Eq. 1}$$

Where G_{12} corresponds to the free energy of the formed solution and G_1, G_2 to free energy of pure solvent (1) and polymer (2). Indeed, the spontaneous formation of the solution is determined by the negative of the free energy of mixing ($\Delta G_m < 0$). Additionally, the free energy of the mixture can be separated in the corresponding enthalpy and entropy contributions:

$$\Delta G_m = \Delta H_m - T\Delta S_m \quad \text{Eq. 2}$$

Here, under ideal solution conditions, the interaction parameter associated with enthalpy is $\Delta H_m = 0$. To ensure ideal conditions, molecular sizes, as energy of interactions between 1-2, 1-1, and 2-2, are assumed to be equal. This condition is called *athermal mixing*, where rotational, vibrational, or translational entropies are the same after the solution formation. The remainder term, also called combinatorial entropy, is always positive after the mixing ($\Delta S_m > 0$). The reason behind this is the increase of the distinguishable spatial arrangement after the mixing.

To provide a clearer description of ΔS_m, statistical mechanics propose the formation of a three-dimensional lattice where each cell has a dimension of molecular size and each molecule can organize randomly (Figure 14). Here we can define the combinatorial entropy of the system based on the accessible distinguishable states Ω.

$$\Delta S_m = k \ln \Omega \quad \text{Eq. 3}$$

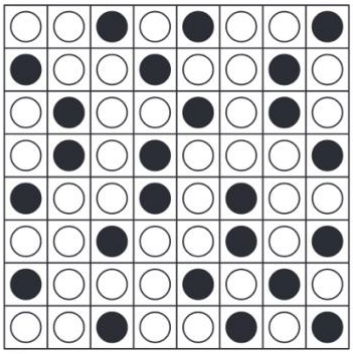

Figure 14. *Representation of the three-dimensional lattice. Solvent (white circles) and solute (black circles) molecules are assumed to have identical size and they can fit inside each molecular size cell (Figure adapted from [87]).*

The combinatorial entropy can now be applicable to the ideal solution conditions:

$$\Delta S_m^{comb} = k[\ln \Omega_{12} - (\ln \Omega_1 + \ln \Omega_2)] \quad \text{Eq. 4}$$

Distinguishable states for the mixture Ω_{12}, solvent Ω_1, and solute Ω_2 are indicated. For the case of a pure substance, the number of distinguishable spatial arrangements is 1 ($\Omega_1 = 1,\ \Omega_2 = 1$). In that order, the combinatorial entropy will be determined by the mixture contribution:

$$\Delta S_m^{comb} = k \ln \Omega_{12} \quad \text{Eq. 5}$$

For a system composed of N_1 molecules of solvent and N_2 molecules of solute with a three-dimensional lattice of ($N_1 + N_2$) places, the combinatorial entropy of the mixing is defined by:

$$\Delta S_m^{comb} = -k\left\{N_1 \ln\left[\frac{N_1}{N_1 + N_2}\right] + N_2 \ln\left[\frac{N_2}{N_1 + N_2}\right]\right\} \quad \text{Eq. 6}$$

Commonly, thermodynamical properties are defined using molar units. Here, we convert this expression in terms of molar fraction $X_i = n_i.(n_i + n_j)^{-1}$ using the Avogadro number $n_i = N_i / N_A$ and the universal gas constant $R = kN_A$. The final expression is the following:

$$\Delta S_m^{comb} = -R[n_1 \ln X_1 + n_2 \ln X_2] \quad \text{Eq. 7}$$

The free energy for the formation of the ideal solution is $\Delta G_m = -T\Delta S_m^{comb}$, so that we arrive to:

$$\Delta G_m = RT[n_1 \ln X_1 + n_2 \ln X_2] \quad \text{Eq. 8}$$

The final description of the free energy of the mixing is an important result for the thermodynamic properties. However, its application is limited because only a few systems behave as ideal solutions. In the context of small molecules where sizes are comparable, the main source of discrepancy correlates with athermal mixing ($\Delta H_m \neq 0$). In addition, polymer solutions show a large deviation from ideality even in cases where $\Delta H_m = 0$, mainly because of the assumption that polymer

molecules have a similar size than solvent molecules. In the following section, we are going to present the Flory-Huggins theory and attempt to address the main limitations involved in this first approximation.

4.1.2 Flory-Huggins theory

The initial step in the Flory-Huggins theory is the prediction of the free energy of the mixing ΔG_m for a system composed of solvent and polymer molecules. Here, the polymer molecules are represented by segments, each of which has an identical volume size than a solvent molecule. The size of the polymer molecule can be determined by the number of segments x in the chain. The similar size between segments and solvent molecules enables us to fit them in the three-dimensional lattice described before. Solvent molecules and chain segments can be fit in individual cells with the additional restriction of connectivity between segments x of the polymer molecule.

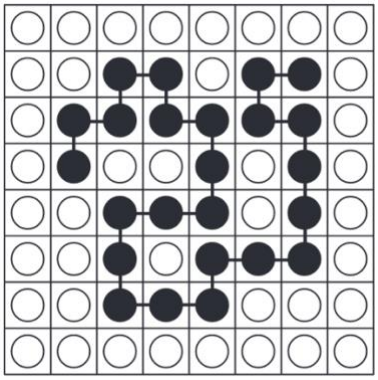

Figure 15. *Three-dimensional lattice that includes solvent and polymer molecule. Solvent molecules are indicated by empty circles. Chain segments of the polymer are indicated by black circles. Note that the connectivity between chain segments induces a restriction in the accessible number of spatial arrangements for the system (Figure adapted from [87]).*

To simplify the prediction of the free energy of the mixing we are going to consider a system where solvent and polymer do not interact $\Delta H_m = 0$. Under this condition, the free energy of the mixing is determined by the combinatory entropy of the system. Unlike the solvent $(\Omega_1 = 1)$, the polymer can adopt more than one conformation (distinguishable spatial arrangement) as a pure substance $(\Omega_2 > 1)$. Using the combinatory entropy (Eq. 7) for ideal solutions, we can derivate the entropy of mixing for the polymer system:

$$\Delta S_m^{comb} = k \ln \frac{\Omega_{12}}{\Omega_2} \qquad \text{Eq. 9}$$

The distinguishable number of arrangements for the polymer mixture Ω_{12} is defined for a three-dimensional lattice of a number of cells N given by the solvent N_1 and polymer molecules N_2 along with segmental chains $(N = N_1 + xN_2)$:

$$\Omega_{12} = \Omega_2 \left[\left(\frac{N}{xN_2} \right)^{N_2} \left(\frac{N}{N_1} \right)^{N_1} \right] \quad \text{Eq. 10}$$

Now combining this expression with (Eq. 9), we can derivate the combinatory entropy for the polymer mixture:

$$\Delta S_m^{Comb} = -k \ \ln \left[N_1 \ln \left(\frac{N_1}{N} \right) + N_2 \ln \left(\frac{xN_2}{N} \right) \right] \quad \text{Eq. 11}$$

Then, we represent the combinatorial entropy in terms of moles ($n_i = N_i/N_A$) and volume fractions for solvent $\phi_1 = N_1/(N_1 + xN_2)$ and polymer $\phi_2 = xN_2/(N_1 + xN_2)$. Here, we arrive at the final expression using ($k = R/N_A$):

$$\Delta S_m^{comb} = -R[n_1 \ln \phi_1 + n_2 \ln \phi_2] \quad \text{Eq. 12}$$

Note that under identical sizes for solvent and solute (Eq.11) is reduced to the expression for ideal solutions. Indeed, the expression obtained here is a general expression for athermal mixing between solvent and solute with different sizes.

4.1.3 Flory-Huggins interaction parameter:

The second step in the Flory-Huggins theory is the description of the enthalpy mixture associated with intermolecular interactions. Here we are going to consider a contact-free energy $\Delta G_m^{contact}$ which includes the entropy change associated with the change in randomness after interaction takes place. Three types of different interactions are considered: *solvent-solvent* g_{11}, *polymer segment- polymer segment* g_{22} and *solvent-polymer segment* g_{12} [87].

The free energy change Δg_{12} associated with the formation of the segment-solvent interaction is linked to the contribution of the segment-solvent, solvent-solvent, and segment-segment interaction.

$$\Delta g_{12} = g_{12} - \frac{1}{2}(g_{11} + g_{22}) \quad \text{Eq. 13}$$

Additionally, the contact-free energy $\Delta G_m^{contact}$ will consider the number of solvent-segment contacts in solution p_{12}:

$$\Delta G_m^{contact} = p_{12} \Delta g_{12} \quad \text{Eq. 14}$$

To define the number of solvent-segment contacts, we define the number of adjacent lattice sites per molecule of polymer as $(z-2)x + 2$. For the case of large molecules as polymers $(z-2)x \gg 2$ the expression is reduced to $N_2(z-2)x$ where z represents the coordination number in the lattice (Figure 3). Additionally, following the mean-field approximation, a certain number of places will be occupied by the solvent molecules ϕ_1. Finally, we derive an expression for the segment-solvent contacts:

$$p_{12} = N_2(z-2)x\phi_1 \quad \text{Eq. 15}$$

Using the equivalent of $N_1\phi_2 = xN_2\phi_1$, we can express the previous expression in terms of volume fraction of the polymer ϕ_2:

$$p_{12} = (z-2)N_1\phi_2 \qquad \text{Eq. 16}$$

Then, using (Eq.14), we can provide the contact-free energy expression:

$$\Delta G_m^{contact} = (z-2)N_1\phi_2\Delta g_{12} \qquad \text{Eq. 17}$$

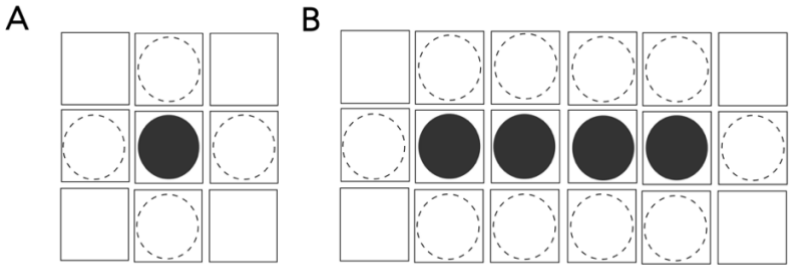

Figure 16. *Coordination number z and adjacent lattice sites for segment (A) and polymer molecule (B).*

Because the experimental access to the lattice coordination number z and the free energy change Δg_{12} are hard to measure, a single parameter representative of both is introduced χ. This term is recognized as *Flory-Huggins solvent-polymer interaction parameter:*

$$\chi = \frac{(z-2)\Delta g_{12}}{kT} \qquad \text{Eq. 18}$$

The Flory-Huggins interaction parameter is a temperature-dependent and dimensionless parameter that includes contributions from enthalpy and entropy:

$$\chi = \chi_H + \chi_S \qquad \text{Eq. 19}$$

Here enthalpy contributions are temperature dependent $\chi_H = b/T$. Instead, entropy is assumed as constant $\chi_s = a$.

Using the relations $N_1 = n_1N_A$ and $R = kN_A$, we can report the contact-free energy based on the Flory-Huggins interaction parameter:

$$\Delta G_m^{contact} = RTn_1\phi_2\chi \qquad \text{Eq. 20}$$

After obtaining the contact-free energy and combinatorial entropy of mixing, we can introduce the Flory-Huggins for Gibbs free energy of mixing (Eq. 21):

$$\Delta G_m = \Delta G_m^{Contact} - T\Delta S_m^{comb} \qquad \text{Eq. 21}$$

$$\Delta G_m = RT[n_1 \ln \phi_1 + n_2 \ln \phi_1 + n_1\phi_2\chi]$$

4.1.4 Chemical potential for polymer solutions:

Polymer solutions similar to other thermodynamic systems can be described using intensive properties of the system (properties independent of the amount of material, e.g., temperature, pressure, etc.). Additionally, partial molar quantities $\bar{z}_i$ are commonly used to investigate changes in thermodynamic properties when a small amount of n_i component is added to the system. The partial molar quantity is defined by:

$$\bar{z}_i = \left(\frac{\partial z}{\partial n_i}\right)_{P,T,n_j} \quad \text{Eq. 22}$$

Two partial molar quantities are extensively use in the context of polymer solutions [87]. These are partial molar volume $\overline{V_i}$ and partial molar free energy $\overline{G_i}$. The last property reassembles in one of the most important thermodynamic properties, called chemical potential μ_i.

$$\mu_i = \left(\frac{\partial G}{\partial n_i}\right)_{P,T,n_j} \quad \text{Eq. 23}$$

For the case of non-ideal solutions under equilibrium conditions, the chemical potential is defined:

$$\mu_i - \mu_i^0 = RT \ln a_i \quad \text{Eq. 24}$$

Where μ_i^0 represents the standard-state chemical potential and a_i the activity of substance *i*. The difference $\mu_i - \mu_i^0$ represents partial molar free energy change $\overline{\Delta G_i}$. We can apply this definition to the Flory-Huggins free energy of mixing to obtain the partial molar free energy for solvent and polymer components:

For the case of the solvent:

$$\mu_i - \mu_i^0 = \left(\frac{\partial \Delta G_m}{\partial n_1}\right)_{P,T,n_2} = RT \frac{\partial}{\partial n_1}\{n_1 \ln \phi_1 + n_2 \ln \phi_2 + n_1 \phi_2 \chi\}_{P,T,n_2} \quad \text{Eq. 25}$$

$$\mu_i - \mu_i^0 = \left(\frac{\partial \Delta G_m}{\partial n_1}\right)_{P,T,n_2} = RT \left[\ln \phi_1 + \left(1 - \frac{1}{x}\right)\phi_2 + \chi \phi_2^2\right]$$

For the case of the polymer:

$$\mu_i - \mu_i^0 = \left(\frac{\partial \Delta G_m}{\partial n_2}\right)_{P,T,n_1} = RT \frac{\partial}{\partial n_2}\{n_1 \ln \phi_1 + n_2 \ln \phi_2 + n_1 \phi_2 \chi\}_{P,T,n_1} \quad \text{Eq. 26}$$

$$\mu_i - \mu_i^0 = \left(\frac{\partial \Delta G_m}{\partial n_2}\right)_{P,T,n_2} = RT \left[\ln \phi_2 - (x-1)\phi_1 + \chi \phi_1^2\right]$$

The resulting expressions for the partial molar free energy can be used to back-calculate the activity of solvent and polymer in the system. This information is useful when experimental data is contrasted with the theoretical prediction for activities. In the following, we are going to review the implications of Flory-Huggins theory in the description of the phase separation properties of polymer systems.

4.1.4 Phase separation by Flory-Huggins theory:

The thermodynamic description offered by Flory- Huggins (FH) theory gives the opportunity to explain the phase separation phenomenon of polymer solutions. First, we express the Flory-Huggins free energy of the mixture in molar quantities ΔG_m^* dividing the (Eq. 21) by $(n_1 + xn_2)$:

$$\Delta G_m^* = RT[\phi_1 \ln \phi_1 + \left(\frac{\phi_2}{x}\right) \ln \phi_2 + \chi\, \phi_1 \phi_2] \qquad \text{Eq. 27}$$

Here, we can identify that both initial terms are always negative and represent the entropy contribution to the mixing. These terms always promote miscibility, favoring the formation of a uniform phase. In contrast, the second term depends on temperature and FH polymer-solvent interaction parameter χ. These terms can promote the demixing of the solution. To visualize the counterbalance of these contributions, we present the changes in the FH free energy when a uniform polymer solution is preferred and when instability can drive the phase separation of the mixture (Figure 17A-B).

First, we consider a condition where solvent and polymer are soluble in the complete range of volume fractions (Figure 17A). Here, a single global minimum is presented in the FH free energy curve. If we select a composition φ_A, we can show that any accessible composition for a two-phase system $\varphi_A^1 < \varphi_A$ and $\varphi_A^2 > \varphi_A$ produces a positive change in the FH free energy (distance between the initial composition and tie-line that joins the final volume fractions). This means that a uniform system is stable and favorable thermodynamically. Now, we consider a condition where the polymer solution is unstable promoting a two-phase system through phase separation (Figure 4B). In this case, two energy minimums are observed in the free energy curve. These energy minimums are associated with two specific compositions, a polymer-depleted phase φ_2' and a polymer-rich phase φ_2''. Note, that compositions between $0 < \varphi_2 < \varphi_2'$ and $\varphi_2'' < \varphi_2 < 1$ lead to a similar conclusion exposed for the stable solution where the uniform phase is favorable. Next, we consider a composition φ_B that presents between $\varphi_2' < \varphi_B < \varphi_2''$ (Figure 17B). Here, after the system is broken into two compositions φ_B^1 and φ_B^2, FH free energy change becomes negative, promoting the formation of a two-phase system. Under these conditions, phase separation happens spontaneously and the final composition of the mixture is determined by the two-energy minimum in the curve. Then, thermodynamic equilibrium is ensured by the equality of the chemical potential of all species in each phase (Eq. 28). This condition is illustrated by a common tangent line shared by two points in the curve (Figure 17B, dash-line).

$$\mu_1' - \mu_1^0 = \mu_1'' - \mu_1^0 \qquad \text{Eq. 28}$$

$$\mu_2' - \mu_2^0 = \mu_2'' - \mu_2^0$$

Following, we explore the region between $\varphi_2' < \varphi_2 < \varphi_B^1$ and $\varphi_B^2 < \varphi_2 < \varphi_2''$ where phase separation is still favorable. Note, an increase in the FH free energy is associated with the demixing process, meaning that phase separation will not occur spontaneously. This region is classified as meta-stable and an energy barrier should be overcome to form a binary system. Separation between regions where phase separation can be promoted spontaneously or not are the inflection points in the FH free energy curve which are called *spinodal compositions*. Unstable and meta-stable regions are delimitated by binodal and spinodal curves as indicated in (Figure 17B).

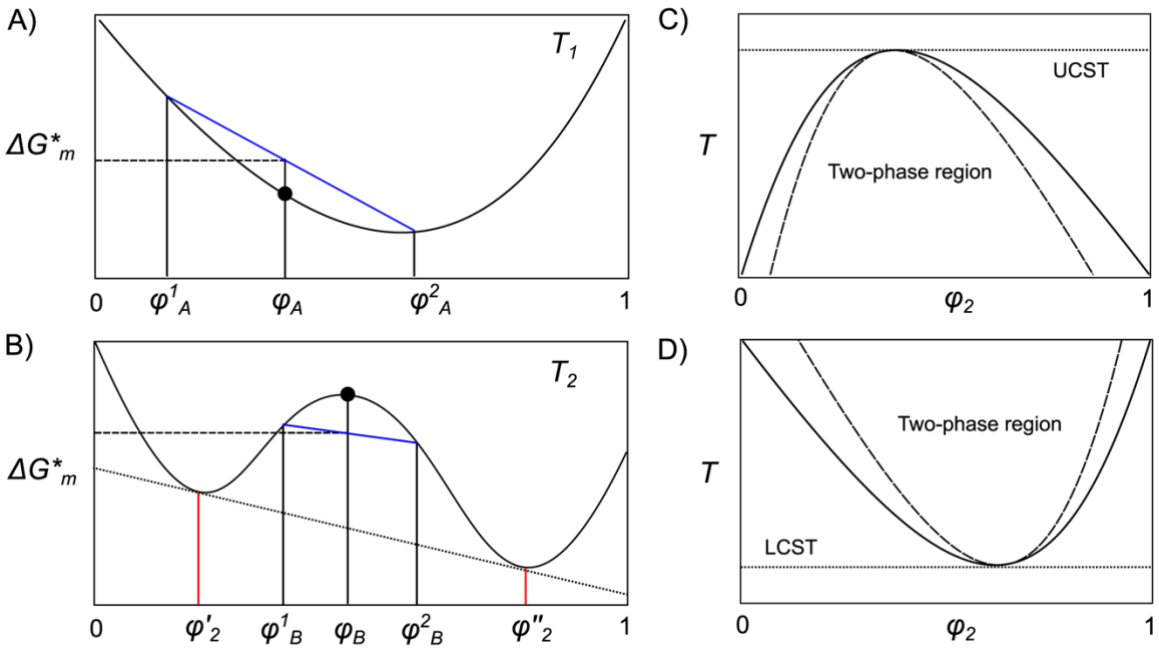

Figure 17. *Flory-Huggins free energy landscape and phase diagrams for polymer solutions. A) FH Free energy curve for a stable polymer solution. B) FH Free energy landscape for a polymer solution that can undergo phase separation. C) Illustrative Phase diagram for polymer solution with UCST behavior. D) Illustrative Phase diagram for polymer solution that undergoes LCST behavior. The solid line represents the coexistent curve or binodal curve, instead dash-line inside the two-phase region represents the spinodal curve. Critical temperatures indicate the point of merging for binodal and spinodal curves.*

Commonly, the phase separation of polymer solutions is represented by the phase diagram of the system. As we described before, phase separation is promoted by non-zero enthalpy contributions indicated in (Eq. 27). These contributions are determined by the FH-interaction parameter and global temperature. Experimentally, the temperature is an accessible parameter that allows us to modulate and control the phase separation conditions. We illustrate in (Figure 4C) a typical phase diagram for a polymer solution where low temperature reduces the miscibility and promotes the formation of the two-phase system. This behavior is characteristic of systems with an upper critical solution temperature (UCST). On the contrary, some polymer solutions have the opposite behavior where an increment of temperature promotes the demixing of the polymer solution (Figure 4D). Such behavior is consistent with specific and favorable interactions between solvent and solute. For example, extensive hydrogen bond networks between polymer segments and solvent. Polymer solutions under this category have a lower critical solution temperature (LCST).

4.1.5 Flory-Huggins theory: relevance and limitations

FH theory was a significant step in understanding the thermodynamical principles of polymer solutions. However, several considerations should be addressed when this theory is applied to describe and interpret experimental results. The assumption of a unique lattice size where solvent and polymer molecules can fit is a reductionistic view of the system (solvent molecule size is not necessarily identical to monomer units). Additionally, a uniform organization of the polymer chains represented in the model is only possible for high-concentrate solutions. However, this assumption is not fully satisfied when the solution turns diluted and chains are mostly isolated. On the other hand, the interaction parameter is a complex one, being a mixture of enthalpy and entropy contributions. Nevertheless, FH theory established the basics for more sophisticated theories used today in polymer science.

4.2 Appendix 2

4.2.1 Two-dimensional exchange spectroscopy (EXSY)

Chemical exchange is a dynamic process that can be studied through a specialized group of NMR experiments. A suitable experiment is chosen by the time scale of the exchange process. In the present case, we are interested in the exchange process which takes place in the very slow exchange regime $k \ll |\Omega_\Delta/2|$. Here, k represents the exchange constant and Ω_Δ corresponds to the frequency difference between both sites. Under these conditions, the exchange process has no impact on the linewidth of the sites involved, so a dedicated experiment called 2D Exchange Spectroscopy (EXSY) is employed [88]. To explain how this experiment works we consider a symmetrical two-site exchange process. These conditions ensure that concentrations and relaxation properties are equal in both exchange sites. The 2D EXSY pulse sequence is presented below (Figure 18):

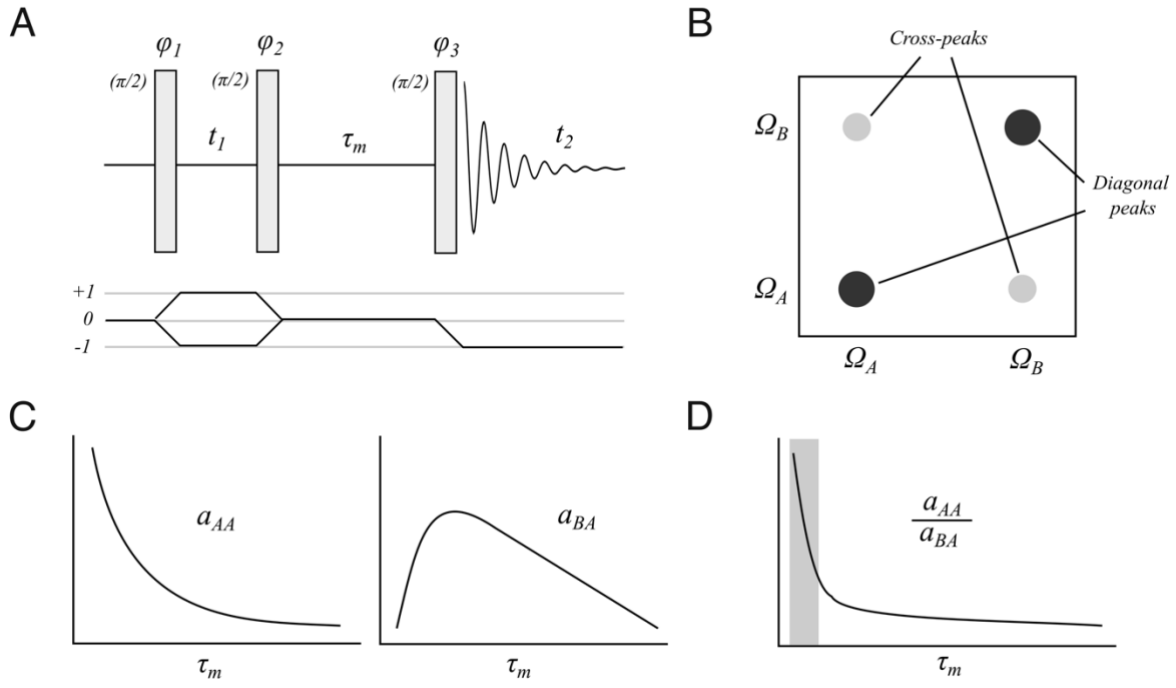

Figure 18. *Two-dimensional Exchange Spectroscopy (EXSY). A) Pulse sequence representative of the EXSY experiment. Coherence transfer pathways are illustrated on the bottom. B) 2D NMR spectrum corresponding to EXSY experiment. Diagonal peaks and cross-peaks associated with the exchange process are indicated. C) Mixing coefficients for diagonal peaks a_{AA} and cross-peaks a_{BA} are presented. D) The initial rate approximation region is indicated by the gray zone (Figure adapted from [89]).*

As (Figure 18A) indicates, three non-selective pulses constitute the basics of the EXSY experiment. In the first part, a $\pi/2$-pulse creates transversal magnetization which evolves during the period t_1. Here, the complex magnetization components $M_{A,B}^+$ in both sites are described by [88]:

$$M_A^+(t_1) = M_{A0}\exp(i\Omega_A t_1 - t_1/T_2) \qquad \text{Eq. 29}$$

$$M_B^+(t_1) = M_{B0}\exp(i\Omega_B t_1 - t_1/T_2)$$

After the transversal magnetization evolves, the second $\pi/2$ pulse with phase along the y-axis converts the real part of the transversal magnetization to a longitudinal magnetization $M_{Az,Bz}$:

$$M_{Az}(t_m = 0) = -M_{A0} \cos \Omega_A t_1 \exp\{-t_1/T_2\} \quad \text{Eq. 30}$$

$$M_{Bz}(t_m = 0) = -M_{B0} \cos \Omega_B t_1 \exp\{-t_1/T_2\}$$

Following, we have the mixing time τ_m in which the exchange could take place. During that time longitudinal magnetization can experience cross-relaxation or exchange between both sites. The longitudinal magnetization at end of the mixing period is given by:

$$\begin{aligned} M_{Az}(\tau_m) = M_{Az}(t_m = 0)\ \frac{1}{2}[1 + \exp\{-2k\tau_m\}] \exp\{-\tau_m/T_1\} \\ + M_{Bz}(t_m = 0)\ \frac{1}{2}[1 - \exp\{-2k\tau_m\}] \exp\{-\tau_m/T_1\} \\ M_{Bz}(\tau_m) = M_{Az}(t_m = 0)\ \frac{1}{2}[1 - \exp\{-2k\tau_m\}] \exp\{-\tau_m/T_1\} \\ + M_{Bz}(t_m = 0)\ \frac{1}{2}[1 + \exp\{-2k\tau_m\}] \exp\{-\tau_m/T_1\} \end{aligned} \quad \text{Eq. 31}$$

Finally, longitudinal magnetization is converted to an observable term through the last $\pi/2$ pulse. If an exchange process or cross-relaxation takes place during the mixing time, a cross-peak at (Ω_A, Ω_B) will appear in the 2D EXSY experiment (Figure 18B). The intensity of the cross-peak and diagonal peaks $(\Omega_A = \Omega_A, \Omega_B = \Omega_B)$ will be determined by the mixing coefficients $a_{kl}(\tau_m)$ and equilibrium magnetization M_{A0} or M_{B0}:

$$I_{AA}(\tau_m) = a_{AA}(\tau_m) M_{A0} \quad \text{Eq. 32}$$

$$I_{BB}(\tau_m) = a_{BB}(\tau_m) M_{B0}$$

$$I_{AB}(\tau_m) = a_{AB}(\tau_m) M_{B0}$$

$$I_{BA}(\tau_m) = a_{BA}(\tau_m) M_{A0}$$

Here, we observe that mixing coefficients (Figure 18C) are equivalent to the factors present in (Eq. 31):

$$\begin{aligned} a_{AA}(\tau_m) = a_{BB}(\tau_m) = \frac{1}{2}[1 + \exp\{-2k\tau_m\}] \exp\{-\tau_m/T_1\} \\ a_{AB}(\tau_m) = a_{BA}(\tau_m) = \frac{1}{2}[1 - \exp\{-2k\tau_m\}] \exp\{-\tau_m/T_1\} \end{aligned} \quad \text{Eq. 33}$$

Note, using the ratio between mixing coefficients can remove the contributions from T_1 relaxation time, and the exchange constant k can be determined using the intensity ratio between diagonal peak and cross-peak:

$$\frac{I_{AA}}{I_{AB}} = \frac{a_{AA}}{a_{AB}} = \frac{1 + \exp\{-2k\tau_m\}}{1 - \exp\{-2k\tau_m\}} \cong \frac{1 - k\tau_m}{k\tau_m} \qquad \text{Eq. 34}$$

The linearity is preserved under the initial rate approximation (Figure 18D), which is valid for a symmetrical two-site exchange and short mixing times ($k\tau_m < 1$). In general, precise determination of exchange constants involves the acquisition of several 2D EXSY experiments where the mixing time is changed.

4.3 Appendix 3

4.3.1 Magnetic field gradients and spatially resolved NMR

Under high-resolution conditions, NMR spectroscopy looks for highly homogeneous fields where resonances can be uniform along space (Figure 19A). However, for spatially-resolved methods, application of variable magnetic fields is essential to obtain spatial resolution of the resonances of interest. To achieve that, we can apply magnetic field gradients which can slightly modify the main component of the principal magnetic field B_0. For example, a linear magnetic field along the z-axis can turn the Larmor frequency of the nuclei to being spatially dependent along the z-axis (Figure 1B). For an isolated spin, the Larmor frequency $\omega(z)$ is defined as:

$$\omega(\mathrm{z}) = \gamma B_0 + \gamma G.z \qquad \text{Eq. 35}$$

Here, γ represents the gyromagnetic ratio of nuclei and G represents the gradient strength of the magnetic field.

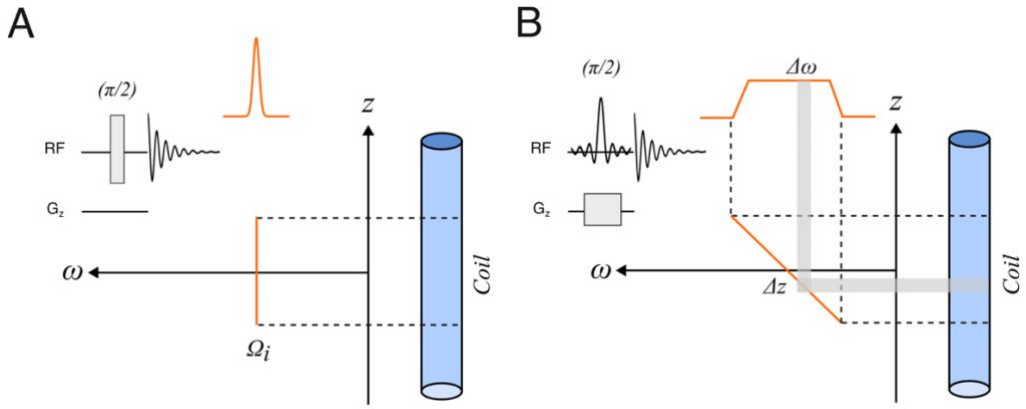

Figure 19. *Basics elements of spatially-resolved NMR. A) A non-selective NMR experiment. The application of the non-selective $\pi/2$ pulse excites the complete active coil in the sample. Because of the uniform B_0 along to z-axis a single resonance Ω_i is observed. B) Spatially resolved NMR experiment. In contrast, the application of the magnetic field gradient encoded the resonance along the z-axis. Then, simultaneous application with a selective (SINC) pulse enables collection of spatially resolved information restricted to region Δz.*

This linear relationship (Eq. 35) is essential for MRI applications allowing spin information to be encoded in space [70]. However, to choose a discrete region we need to combine the application of a magnetic field gradient and selective pulse (Figure 19B). Here, the selection thickness Δz depends on the gradient strength and bandwidth of the selective pulse $\Delta\omega$.

$$\Delta z = \frac{\Delta\omega}{\gamma G} \qquad \text{Eq. 2}$$

Additionally, the spatial position is determined by the resonance signal Ω_i and the central frequency of the RF pulse ω_{RF}.

$$z_0(\Omega_i) = \frac{\Omega_i - \omega_{RF}}{\gamma G} \quad \text{Eq. 3}$$

There is an important consideration regarding the range of signals of interest $\Delta\Omega_i$. Under conditions where $\Delta\omega \gg \Delta\Omega_i$, the complete set of signals can be treated as recruited in one slice. However, under matched-gradient conditions $\Delta\omega \sim \Delta\Omega_i$, each chemical shift should be treated as a different slice in the sample [75]. In general, both conditions are used depending of the application aim.

References

1. Banani, S.F., et al., *Biomolecular condensates: organizers of cellular biochemistry.* Nat Rev Mol Cell Biol, 2017. **18**(5): p. 285-298.
2. Hyman, A.A., C.A. Weber, and F. Jülicher, *Liquid-Liquid Phase Separation in Biology.* Annual Review of Cell and Developmental Biology, 2014. **30**(1): p. 39-58.
3. Cohan, M.C. and R.V. Pappu, *Making the Case for Disordered Proteins and Biomolecular Condensates in Bacteria.* Trends Biochem Sci, 2020. **45**(8): p. 668-680.
4. Mitrea, D.M. and R.W. Kriwacki, *Phase separation in biology; Functional organization of a higher order Short linear motifs - The unexplored frontier of the eukaryotic proteome.* Cell Communication and Signaling, 2016. **14**(1): p. 1-20.
5. Brangwynne, C.P., et al., *Germline P granules are liquid droplets that localize by controlled dissolution/condensation.* Science, 2009. **324**(5935): p. 1729-32.
6. Dobry, A. and F. Boyer-Kawenoki, *Phase separation in polymer solution.* Journal of Polymer Science, 1947. **2**(1): p. 90-100.
7. Cheremisinoff, N.P., *Handbook of polymer science and technology*. Vol. 4. 1989: CRC Press.
8. Riback, J.A., et al., *Composition-dependent thermodynamics of intracellular phase separation.* Nature, 2020. **581**(7807): p. 209-214.
9. Wang, J., et al., *A Molecular Grammar Governing the Driving Forces for Phase Separation of Prion-like RNA Binding Proteins.* Cell, 2018. **174**(3): p. 688-699.e16.
10. Ginell, G.M. and A.S. Holehouse, *An Introduction to the Stickers-and-Spacers Framework as Applied to Biomolecular Condensates.* Methods Mol Biol, 2023. **2563**: p. 95-116.
11. Rubinstein, M. and A.V. Dobrynin, *Solutions of associative polymers.* Trends in Polymer Science, 1997. **5**(6): p. 181-186.
12. Boija, A., I.A. Klein, and R.A. Young, *Biomolecular Condensates and Cancer.* Cancer Cell, 2021. **39**(2): p. 174-192.
13. Molliex, A., et al., *Phase separation by low complexity domains promotes stress granule assembly and drives pathological fibrillization.* Cell, 2015. **163**(1): p. 123-33.
14. Nag, N., et al., *Phase separation of FG-nucleoporins in nuclear pore complexes.* Biochim Biophys Acta Mol Cell Res, 2022. **1869**(4): p. 119205.
15. Denning, D.P., et al., *Disorder in the nuclear pore complex: the FG repeat regions of nucleoporins are natively unfolded.* Proc Natl Acad Sci U S A, 2003. **100**(5): p. 2450-5.
16. Frottin, F., et al., *The nucleolus functions as a phase-separated protein quality control compartment.* Science, 2019. **365**(6451): p. 342-347.
17. Lyon, A.S., W.B. Peeples, and M.K. Rosen, *A framework for understanding the functions of biomolecular condensates across scales.* Nature Reviews Molecular Cell Biology, 2021. **22**(3): p. 215-235.
18. Soding, J., et al., *Mechanisms for Active Regulation of Biomolecular Condensates.* Trends Cell Biol, 2020. **30**(1): p. 4-14.
19. Boija, A., et al., *Transcription Factors Activate Genes through the Phase-Separation Capacity of Their Activation Domains.* Cell, 2018. **175**(7): p. 1842-1855 e16.
20. Boehning, M., et al., *RNA polymerase II clustering through carboxy-terminal domain phase separation.* Nature Structural & Molecular Biology, 2018.
21. Alberti, S. and A.A. Hyman, *Biomolecular condensates at the nexus of cellular stress, protein aggregation disease and ageing.* Nat Rev Mol Cell Biol, 2021. **22**(3): p. 196-213.
22. Patel, A., et al., *A Liquid-to-Solid Phase Transition of the ALS Protein FUS Accelerated by Disease Mutation.* Cell, 2015. **162**(5): p. 1066-77.
23. Goedert, M., *Tau protein and the neurofibrillary pathology of Alzheimer's disease.* Trends Neurosci, 1993. **16**(11): p. 460-5.
24. Avila, J., et al., *Role of tau protein in both physiological and pathological conditions.* Physiological reviews, 2004.

25. Ambadipudi, S., et al., *Liquid-liquid phase separation of the microtubule-binding repeats of the Alzheimer-related protein Tau.* Nature Communications, 2017. **8**(1): p. 1-13.
26. Wegmann, S., et al., *Tau protein liquid–liquid phase separation can initiate tau aggregation.* The EMBO Journal, 2018. **37**(7): p. e98049-e98049.
27. Zeng, Y., et al., *The structure and phase of tau: from monomer to amyloid filament.* Cell Mol Life Sci, 2021. **78**(5): p. 1873-1886.
28. Zhou, H.-X., J.-H. Spille, and P.R. Banerjee, *Phase-separated Biomolecular Condensates: Methods and Protocols*. 2022: Springer Nature.
29. Posey, A.E., A.S. Holehouse, and R.V. Pappu, *Phase Separation of Intrinsically Disordered Proteins*. 1 ed. Methods in Enzymology. Vol. 611. 2018: Elsevier Inc. 1-30.
30. Binder, K., *Theory of first-order phase transitions.* Reports on Progress in Physics, 1987. **50**(7): p. 783.
31. Alberti, S., A. Gladfelter, and T. Mittag, *Considerations and Challenges in Studying Liquid-Liquid Phase Separation and Biomolecular Condensates.* Cell, 2019. **176**(3): p. 419-434.
32. Alshareedah, I., T. Kaur, and P.R. Banerjee, *Methods for characterizing the material properties of biomolecular condensates*, in *Methods in enzymology*. 2021, Elsevier. p. 143-183.
33. Levin, B., et al., *Harnessing the power of fluorescence to characterize biomolecular condensates*, in *Methods in Microbiology*. 2021, Elsevier. p. 1-47.
34. Kanaan, N.M., et al., *Liquid-liquid phase separation induces pathogenic tau conformations in vitro.* Nature Communications, 2020. **11**(1).
35. Simon, J.R., et al., *Programming molecular self-assembly of intrinsically disordered proteins containing sequences of low complexity.* Nat Chem, 2017. **9**(6): p. 509-515.
36. Riback, J.A., et al., *Stress-Triggered Phase Separation Is an Adaptive, Evolutionarily Tuned Response.* Cell, 2017. **168**(6): p. 1028-1040 e19.
37. Avni, A., et al., *Single-droplet surface-enhanced Raman scattering decodes the molecular determinants of liquid-liquid phase separation.* Nat Commun, 2022. **13**(1): p. 4378.
38. Ahlers, J., et al., *The key role of solvent in condensation: Mapping water in liquid-liquid phase-separated FUS.* Biophys J, 2021. **120**(7): p. 1266-1275.
39. Linsenmeier, M., et al., *Analysis of biomolecular condensates and protein phase separation with microfluidic technology.* Biochimica et Biophysica Acta (BBA)-Molecular Cell Research, 2021. **1868**(1): p. 118823.
40. Keeler, J., *Understanding NMR spectroscopy*. 2010: John Wiley & Sons.
41. Ernst, R.R. and W.A. Anderson, *Application of Fourier transform spectroscopy to magnetic resonance.* Review of Scientific Instruments, 1966. **37**(1): p. 93-102.
42. Kumar, A. *Two-dimensional nuclear Overhauser effect in biomolecules*. in *Proceedings of the Indian Academy of Sciences-Chemical Sciences*. 1985. Springer.
43. Wüthrich, K., *Protein structure determination in solution by NMR spectroscopy.* Journal of Biological Chemistry, 1990. **265**(36): p. 22059-22062.
44. Rule, G.S. and T.K. Hitchens, *Fundamentals of protein NMR spectroscopy*. Vol. 5. 2006: Springer Science & Business Media.
45. Downing, A.K., *Protein NMR techniques*. Vol. 278. 2008: Springer Science & Business Media.
46. Kay, L.E., *Protein dynamics from NMR.* Biochemistry and cell biology, 1998. **76**(2-3): p. 145-152.
47. Khago, D., I.J. Fucci, and R.A. Byrd, *The Role of Conformational Dynamics in the Recognition and Regulation of Ubiquitination.* Molecules, 2020. **25**(24).
48. Bain, A.D., *Chemical exchange in NMR.* Progress in nuclear magnetic resonance spectroscopy, 2003. **43**(3): p. 63-104.
49. Kleckner, I.R. and M.P. Foster, *An introduction to NMR-based approaches for measuring protein dynamics.* Biochim Biophys Acta, 2011. **1814**(8): p. 942-68.

50. Sekhar, A. and L.E. Kay, *NMR paves the way for atomic level descriptions of sparsely populated, transiently formed biomolecular conformers.* Proceedings of the National Academy of Sciences, 2013. **110**(32): p. 12867-12874.
51. Zwahlen, C., et al., *Methods for measurement of intermolecular NOEs by multinuclear NMR spectroscopy: application to a bacteriophage λ N-peptide/boxB RNA complex.* Journal of the American Chemical Society, 1997. **119**(29): p. 6711-6721.
52. Zuiderweg, E.R., *Mapping protein− protein interactions in solution by NMR spectroscopy.* Biochemistry, 2002. **41**(1): p. 1-7.
53. Murthy, A.C., et al., *Molecular interactions underlying liquid–liquid phase separation of the FUS low-complexity domain.* Nature Structural and Molecular Biology, 2019. **26**(7): p. 637-648.
54. Brady, J.P., et al., *Structural and hydrodynamic properties of an intrinsically disordered region of a germ cell-specific protein on phase separation.* Proceedings of the National Academy of Sciences of the United States of America, 2017. **114**(39): p. E8194-E8203.
55. Kim, T.H., et al., *Interaction hot spots for phase separation revealed by NMR studies of a CAPRIN1 condensed phase.* Proceedings of the National Academy of Sciences of the United States of America, 2021. **118**(23): p. 1-11.
56. Toyama, Y., et al., *Mapping the per-residue surface electrostatic potential of CAPRIN1 along its phase-separation trajectory.* 2022.
57. Cowan, B. and B. Cowan, *Nuclear magnetic resonance and relaxation*. Vol. 427. 1997: Cambridge University Press Cambridge.
58. Toyama, Y., et al., *Surface electrostatics dictate RNA-binding protein CAPRIN1 condensate concentration and hydrodynamic properties.* Journal of Biological Chemistry, 2023. **299**(1).
59. Murthy, A.C. and N.L. Fawzi, *The (un)structural biology of biomolecular liquid-liquid phase separation using NMR spectroscopy.* Journal of Biological Chemistry, 2020. **295**(8): p. 2375-2384.
60. Mitrea, D.M., et al., *Modulating biomolecular condensates: a novel approach to drug discovery.* Nature Reviews Drug Discovery, 2022: p. 1-22.
61. Sang, D., et al., *Condensed-phase signaling can expand kinase specificity and respond to macromolecular crowding.* Mol Cell, 2022. **82**(19): p. 3693-3711 e10.
62. Kaufmann, H., J.E. Bailey, and M. Fussenegger, *Use of antibodies for detection of phosphorylated proteins separated by two-dimensional gel electrophoresis.* PROTEOMICS: International Edition, 2001. **1**(2): p. 194-199.
63. Amata, I., et al., *Multi-phosphorylation of the intrinsically disordered unique domain of c-Src studied by in-cell and real-time NMR spectroscopy.* ChemBioChem, 2013. **14**(14): p. 1820-1827.
64. Kartzmark, E., *System triethylamine–water: the equilibrium diagram and some physical properties.* Canadian Journal of Chemistry, 1967. **45**(10): p. 1089-1091.
65. Palmer, A.G., J. Williams, and A. McDermott, *Nuclear magnetic resonance studies of biopolymer dynamics.* The Journal of Physical Chemistry, 1996. **100**(31): p. 13293-13310.
66. Fabry, M.E. and R.C. San George, *Effect of magnetic susceptibility on nuclear magnetic resonance signals arising from red cells: a warning.* Biochemistry, 1983. **22**(17): p. 4119-4125.
67. Zamir, D., R. Wayne, and R. Cotts, *Anomalous nuclear magnetic resonance linewidth in lithium.* Physical Review Letters, 1964. **12**(12): p. 327.
68. Johns, M., *NMR studies of emulsions.* Current opinion in colloid & interface science, 2009. **14**(3): p. 178-183.
69. Brindle, K.M., et al., *Application of spin-echo nuclear magnetic resonance to whole-cell systems. Membrane transport.* Biochemical Journal, 1979. **180**(1): p. 37-44.
70. Callaghan, P.T., *Principles of nuclear magnetic resonance microscopy*. 1993: Oxford University Press on Demand.
71. Jeener, J., et al., *Investigation of exchange processes by two-dimensional NMR spectroscopy.* The Journal of chemical physics, 1979. **71**(11): p. 4546-4553.

72. Cavanagh, J., et al., *Protein NMR spectroscopy: principles and practice*. 1996: Academic press.
73. Vallurupalli, P., G. Bouvignies, and L.E. Kay, *Studying "invisible" excited protein states in slow exchange with a major state conformation.* Journal of the American Chemical Society, 2012. **134**(19): p. 8148-8161.
74. Yuwen, T., J.P. Brady, and L.E. Kay, *Probing Conformational Exchange in Weakly Interacting, Slowly Exchanging Protein Systems via Off-Resonance R1ρ Experiments: Application to Studies of Protein Phase Separation.* Journal of the American Chemical Society, 2018. **140**(6): p. 2115-2126.
75. Dumez, J.N., *Spatial encoding and spatial selection methods in high-resolution NMR spectroscopy.* Prog Nucl Magn Reson Spectrosc, 2018. **109**: p. 101-134.
76. Kozminski, W., *Application of spatially resolved NMR spectroscopy for high resolution of heterogeneous samples.* Polish Journal of Chemistry, 2000. **74**(8): p. 1185-1189.
77. Ogg, R.J., P.B. Kingsley, and J.S. Taylor, *WET, a T1- and B1-insensitive water-suppression method for in vivo localized 1H NMR spectroscopy.* J Magn Reson B, 1994. **104**(1): p. 1-10.
78. Wider, G. and L. Dreier, *Measuring protein concentrations by NMR spectroscopy.* J Am Chem Soc, 2006. **128**(8): p. 2571-6.
79. Bremer, A., et al., *Quantifying Coexistence Concentrations in Multi-Component Phase-Separating Systems Using Analytical HPLC.* Biomolecules, 2022. **12**(10).
80. Villois, A., et al., *Droplet Microfluidics for the Label-Free Extraction of Complete Phase Diagrams and Kinetics of Liquid–Liquid Phase Separation in Finite Volumes.* Small, 2022: p. 2202606-2202606.
81. Arter, W.E., et al., *Biomolecular condensate phase diagrams with a combinatorial microdroplet platform.* Nature Communications, 2022. **13**(1): p. 7845.
82. Wu, H. and M. Fuxreiter, *The structure and dynamics of higher-order assemblies: amyloids, signalosomes, and granules.* Cell, 2016. **165**(5): p. 1055-1066.
83. Hohmann, S., *Osmotic stress signaling and osmoadaptation in yeasts.* Microbiology and molecular biology reviews, 2002. **66**(2): p. 300-372.
84. Majumder, S. and A. Jain, *Osmotic Stress Triggers Phase Separation.* Mol Cell, 2020. **79**(6): p. 876-877.
85. Delarue, M., et al., *mTORC1 controls phase separation and the biophysical properties of the cytoplasm by tuning crowding.* Cell, 2018. **174**(2): p. 338-349. e20.
86. Illenberger, S., et al., *The endogenous and cell cycle-dependent phosphorylation of tau protein in living cells: implications for Alzheimer's disease.* Molecular biology of the cell, 1998. **9**(6): p. 1495-1512.
87. Young, R.J. and P.A. Lovell, *Introduction to polymers*. 2011: CRC press.
88. Ernst, R.R., G. Bodenhausen, and A. Wokaun, *Principles of nuclear magnetic resonance in one and two dimensions*. 1990: Oxford university press.
89. Levitt, M.H., *Spin dynamics: basics of nuclear magnetic resonance*. 2013: John Wiley & Sons.

PCCP

PAPER

View Article Online
View Journal | View Issue

Cite this: *Phys. Chem. Chem. Phys.*, 2022, **24**, 6169

Dynamical component exchange in a model phase separating system: an NMR-based approach†

Christian F. Pantoja, [a] Markus Zweckstetter *[ab] and Nasrollah Rezaei-Ghaleh *[bcd]

Received 4th January 2022,
Accepted 15th February 2022

DOI: 10.1039/d2cp00042c

rsc.li/pccp

Biomolecular phase separation plays a key role in the spatial organization of cellular activities. Dynamic formation and rapid component exchange between phase separated cellular bodies and their environment are crucial for their function. Here, we employ a well-established phase separating model system, namely, a triethylamine (TEA)–water mixture, and develop an NMR approach to detect the exchange of scaffolding TEA molecules between separate phases and determine the underlying exchange rate. We further demonstrate how the advantageous NMR properties of fluorine nuclei provide access to otherwise inaccessible exchange processes of a client molecule. The developed NMR-based approach allows quantitative monitoring of the effect of regulatory factors on component exchange and facilitates "exchange"-based screening and optimization of small molecules against druggable biomolecular targets located inside condensed phases.

Introduction

Liquid–liquid phase separation has emerged as a key physicochemical principle underlying the spatial organization of biomolecules within the cell, and thereby reinvigorated the interest in studying this classical physical chemistry phenomenon.[1–4] Several biophysical techniques have been developed to monitor biomolecular phase separation under *in vitro* and *in vivo* conditions and determine the structural dynamics of its constituents, including proteins, nucleic acids, ions and water molecules.[5–12] A remarkable feature of phase separated cellular bodies is their rapid formation and dissolution in response to regulatory signals and dynamic component exchange with the cellular environment.[13–15] The component exchange occurs not only for the so-called scaffold molecules whose phase behavior governs the formation of phase separated droplets, but also for the client molecules which enter the formed dropelts and undergo dynamic exchange with the environment.[16–18] These features are particularly advantageous in rapidly changing environments and are crucial for the functioning of several cellular bodies.[19–21]

Despite its importance in physiological and potentially pathological processes, little is known about how the component exchange of membrane-less phase separated bodies is regulated by biochemical factors, *e.g.* mutation or chemical modifications in phase-separating biomolecules, the presence of small molecules, *etc.* Progress in this direction requires the development of experimental methods for the quantitative determination of exchange rates. Here, we use a model system for phase separation, namely a triethylamine (TEA)–water mixture, and develop a multi-spin NMR approach to study the exchange process between separated phases at a quantitative level. TEA is a well-established phase separation model system, which undergoes a reversible temperature-dependent phase separation, exhibiting lower critical solution temperature (LCST) behaviour.[22–26] As a result of phase separation, two phases are formed: a TEA-enriched condensed phase and water-enriched phase. In addition to TEA as the scaffold molecule, we investigate the exchange of a fluorine-containing client molecule between separated phases and show how the use of ^{19}F NMR allows detection of the exchange process and quantification of its rate.

Results and discussion

Probing TEA phase separation by microscopy and NMR

First, we examined the temperature-dependent phase separation of a mixture of TEA and dextran using microscopy. The use of dextran as a crowding agent was to slow down the kinetics of the TEA phase separation process. In addition, fluorescently

[a] *Translational Structural Biology Group, German Center for Neurodegenerative Diseases (DZNE), Von-Siebold-Strasse 3a, D-37075 Göttingen, Germany. E-mail: Markus.Zweckstetter@dzne.de*
[b] *Department of NMR-based Structural Biology, Max Planck Institute for Multidisciplinary Sciences, Am Faßberg 11, D-37077 Göttingen, Germany*
[c] *Institut für Physikalische Biologie, Heinrich-Heine-Universität Düsseldorf, Universitätsstr. 1, D-40225 Düsseldorf, Germany. E-mail: Nasrollah.Rezaie.Ghaleh@hhu.de*
[d] *Institute of Biological Information Processing (IBI-7: Structural Biochemistry), Forschungszentrum Jülich, Wilhelm-Johnen-Straße, 52428 Jülich, Germany*

† Electronic supplementary information (ESI) available: Supplementary methods (chemicals, DIC and fluorescence imaging, NMR experiments and data analysis) and Fig. S1. See DOI: 10.1039/d2cp00042c

labeled dextran was used in order to monitor the phase separation process. As reported in the literature, the water–TEA and D_2O–TEA mixtures have LCSTs of *ca.* 18 and 15 °C, respectively.[26,27] As shown in Fig. 1A, at 278 K, the TEA sample exhibited a single dispersed phase, with a nearly uniform background fluorescence emission originating from the labeled dextran. We then increased the temperature to 298 K, resulting in the phase separation of the sample and the formation of a large number of variously sized spherical droplets with an approximate average radius of 4.5 ± 1.5 μm (Fig. 1A). Notably, the dextran was almost completely excluded from the formed droplets and remained in the dispersed phase.

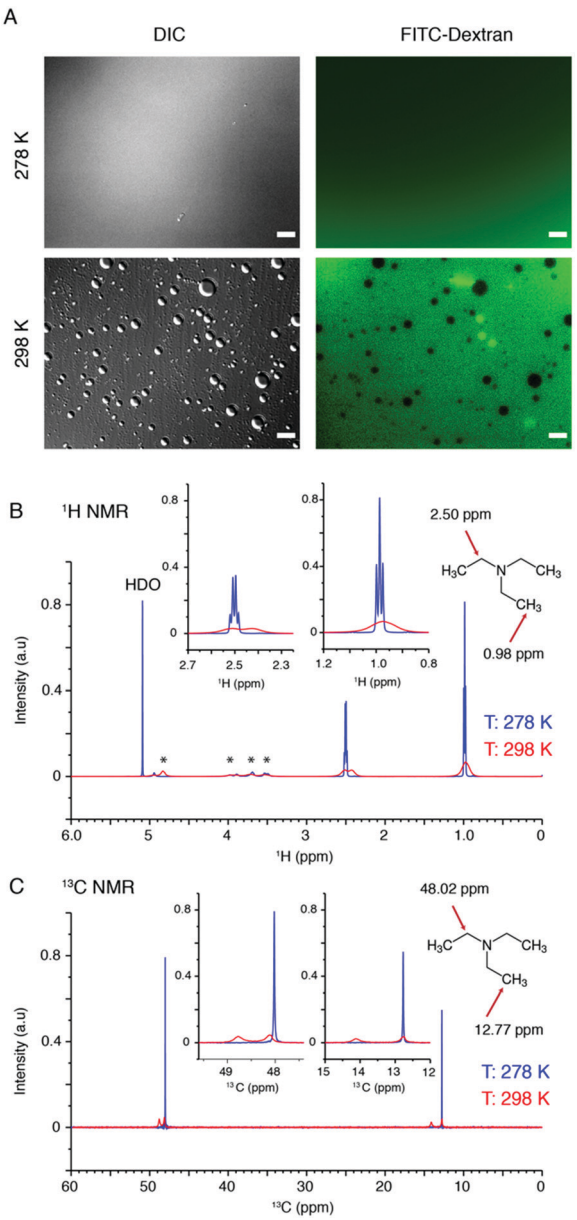

Fig. 1 Liquid–liquid phase separation of triethylamine (TEA)/water/dextran mixture, probed by differential interference contrast (DIC) and fluorescence microscopy (A), and ^{1}H (B) and ^{13}C (C) NMR spectroscopy. ^{1}H signals from dextran are marked by stars in (B). The phase separation-induced broadening in TEA's methylene and methyl ^{1}H (B) and ^{13}C (C) signals, as well as the emergence of new ^{13}C signals can be seen. Scale bars, 10 μm.

Next, we studied the phase separation of TEA using ^{1}H NMR. At 278 K, where the TEA sample displays a single dispersed phase (Fig. 1A), the 1D ^{1}H NMR spectrum showed signals at *ca.* 2.5 and 0.98 ppm, which belong to its methylene and methyl protons, respectively (Fig. 1B). The narrow linewidth of the TEA ^{1}H signals reflect the large level of mobility of this small-sized molecule within the spatially homogeneous dispersed phase. After increasing the temperature to 298 K, and the resultant phase separation, the TEA ^{1}H signals were strongly broadened, and consequently, the characteristic quartet and triplet splitting patterns of methylene and methyl signals were no longer observable. The phase separation-induced signal broadening was not limited to TEA signals, but also observed for the dextran signal. As dextran did not enter the formed droplets, the broadening of its signals seems to reflect the magnetic susceptibility inhomogeneity of the phase separated sample. Accordingly, the TEA signal broadening is potentially caused by three major factors: the altered mobility of TEA within the condensed interior of droplets, the chemical exchange between different phases, and sample inhomogeneity. In addition to signal broadening, the methylene, but not the methyl, signal showed the emergence of a new peak ~0.1 ppm upfield to the original signal.

Next, we investigated the phase separation of TEA using 1D ^{13}C NMR at natural abundance. As expected, the spectrum of the single-phase dispersed TEA sample at 278 K showed two sharp ^{13}C signals at *ca.* 48.02 and 12.77 ppm, belonging to methylene and methyl groups, respectively (Fig. 1C). Similar to the ^{1}H signals, the temperature-induced phase separation led to a significant broadening of TEA's ^{13}C signals and a decrease in their peak height, likely due to the induced alteration in mobility, exchange and sample homogeneity. Unlike the ^{1}H spectrum, however, the ^{13}C spectrum of the phase-separated TEA sample showed two well-resolved new signals downfield of the original methylene and methyl signals. The emergence of these new ^{13}C signals (and the new ^{1}H signal of the methylene group, see above) pointed to the presence of an exchange process between the dispersed and condensed phases of TEA, at a slow rate on the NMR chemical shift timescale, *i.e.* $<1300\ s^{-1}$ (see Fig. 2A).

NMR-based identification of the kinetic stages of TEA phase separation

As a prerequisite for the quantitative investigation of dynamical exchange processes underlying the phase separation of TEA, we established the kinetics of this process through real-time 1D ^{13}C NMR experiments, where we monitored the methyl signals belonging to the dilute and condensed phase. Immediately after the temperature jump from 278 to 298 K, the signal belonging to the dilute phase was significantly broadened and partially lost its peak height. However, further progression of the phase separation process led to the partial recovery of the linewidth and peak height of this signal (Fig. 2A). The broad

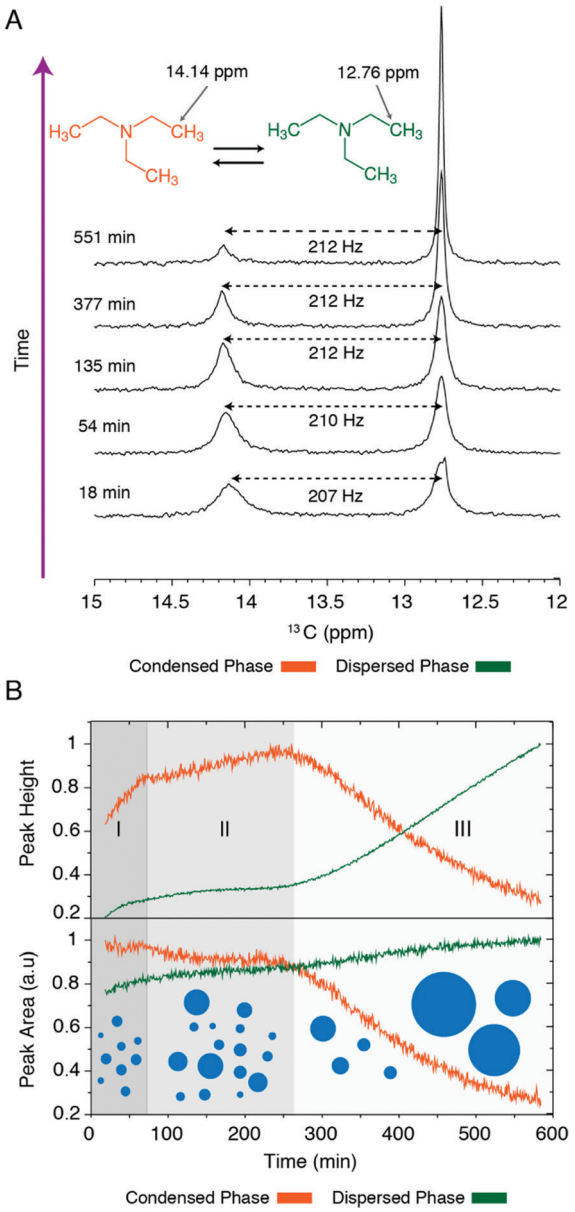

Fig. 2 Kinetics of liquid–liquid phase separation in triethylamine (TEA)/water (D_2O)/dextran mixture, monitored through ^{13}C methyl signals of TEA molecules. (A) Changes in the 1D ^{13}C NMR spectrum of the methyl group of TEA after inducing phase separation through a temperature jump from 278 to 298 K. The signals at 12.76 and 14.14 ppm originate from the dispersed and condensed phase, respectively. (B) Relative peak areas of ^{13}C methyl signals of TEA from the two phases (bottom panel) and the peak heights (top panel) as seen in (A). Three kinetic stages of phase separation (I–III, shaded areas, respectively showing formation, growth and precipitation of large droplets) can be distinguished.

signal belonging to the condensed phase followed a rather distinct trend: the gradual narrowing of the signal during the first 1–3 hours of the process was followed by a sharp decrease in peak height (Fig. 2B). The time-dependence of peak heights and areas (Fig. 2B) indicated the presence of three kinetic stages: an initial stage (around 60 minutes), when the condensed phase signal grew in height, a middle stage (around 60–260 minutes) during which the peak intensities remained relatively stable, and the final stage (*ca.* 260–600 minutes) when a sharp intensity loss was observed for the condensed phase signal. The final intensity loss of the condensed phase signal was due to the formation of large TEA droplets and their precipitation and exit from the detection zone of NMR coils. Notably, this precipitation is reverse, *i.e.* the TEA-enriched phase is not at the bottom but at the top of the sample, due to the lower density of TEA-enriched droplets when compared to the TEA-depleted phase. Accordingly, during kinetic stages I and III, the dominant processes are respectively droplet formation and precipitation, while the kinetic stage II represents a quasi-steady-state during which these two processes partially cancel the effect of each other on NMR signal intensities.

NMR-based investigation of the initial TEA exchange between phases

The study of phase separation-related exchange processes during later kinetic stages (*i.e.* stage III in Fig. 2B) is complicated by the (reverse) precipitation-induced NMR intensity changes. To minimize the interfering effects of (reverse) precipitation, we took advantage of the reversibility of phase separation and developed an experimental scheme, where cycles of heating–cooling were employed and NMR data were collected only during the initial kinetic stage of phase separation (typically the first 15–20 minutes, depending on the experiment). Using this scheme, we were able to measure a clean 2D projection plane of the ^{13}C, ^{1}H, ^{1}H HSQC-NOESY spectrum of TEA during phase separation. As shown in Fig. 3A, ^{13}C, ^{1}H correlation peaks were observed for TEA methylene and methyl groups from both the dispersed and condensed phases and several groups of dextran. Interestingly, the TEA ^{1}H signals belonging to the two phases showed nice correlation peaks, indicating either spatial proximity (and its consequent dipolar coupling-mediated correlation) or chemical exchange between them. The sign of cross-peaks in these and complementary 2D ^{1}H, ^{1}H ROESY spectra (Fig. 3B) excluded the dipolar coupling origin and confirmed the presence of chemical exchange. Notably, no correlation peaks were observed for dextran signals, consistent with the exclusion of dextran from the TEA droplets (Fig. 1A).

Then, we employed the heating–cooling cycles and measured the 2D ^{1}H, ^{1}H EXSY spectra of the phase separated sample at five different mixing times ranging from 15 to 120 ms (Fig. 3C). The EXSY spectra at each mixing time were collected during the first 20 minutes after the initiation of phase separation. The intensity of the exchange-induced correlation peaks displayed the characteristic dependence on mixing time. Analysis of the intensity build-up curves for the methylene and methyl groups provided an effective exchange rate, k_{ex}, of $31 \pm 5\ s^{-1}$, for the exchange of TEA molecules between two phases (Fig. 3D), *i.e.* an exchange process that is slow on the NMR chemical shift timescale.

Fluorine NMR-based investigation of the exchange of a client molecule between TEA phases

To further investigate the component exchange between the phase separated TEA droplets and their environment, we studied the exchange of hexafluoroisopropanol (HFiP) as a

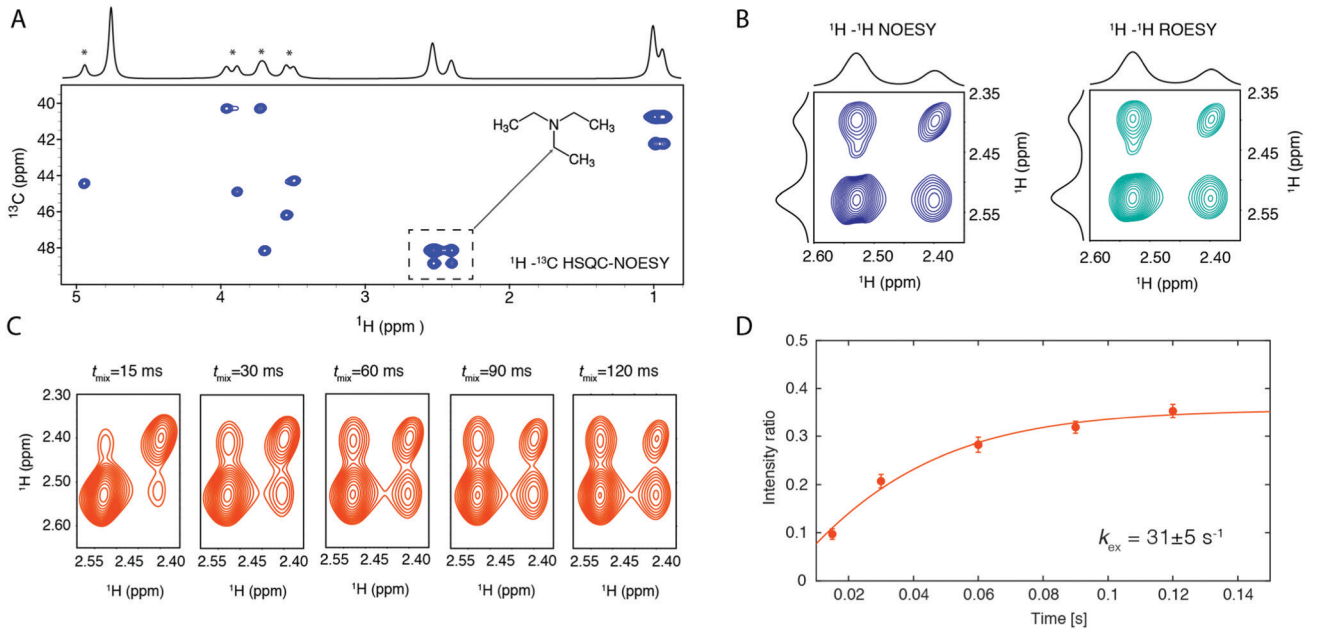

Fig. 3 Detection of chemical exchange of scaffold triethylamine (TEA) molecules between dispersed and condensed phases, through NOESY-type NMR experiments. (A) 2D ^{13}C, ^{1}H plane of an HSQC-NOESY experiment, revealing ^{1}H, ^{1}H correlation peaks for the two methylene and methyl ^{1}H signals of TEA molecules from the two phases. The signals belonging to the crowding agent dextran (marked by stars) did not show any correlation peak, consistent with the exclusion of dextran from the condensed phase. (B) 2D ^{1}H, ^{1}H NOESY and ROESY spectra, zoomed over the two methylene signals of TEA originating from the two phases. The same sign of correlation peaks in NOESY and ROESY spectra confirm "chemical exchange" as their source. (C) The methylene region of the ^{1}H, ^{1}H EXSY spectra of TEA, measured during the initial stage of phase separation at five different mixing times. (D) Quantitative analysis of the intensity build-up curves provides the exchange rate, k_{ex}, of TEA molecules between the two phases. Error bars are calculated by error propagation based on the spectral noise for each mixing time.

potential client molecule. The choice of HFiP was motivated by its fluorine content, as ^{19}F nuclei are highly sensitive to the chemical environment and consequently could act as sensitive probes of exchange processes.[28] After establishing that HFiP (1.6% m/v) did not perturb the phase separation of TEA (Fig. S1, ESI†), we monitored how ^{1}H and ^{19}F NMR signals of HFiP (Fig. 4A) were affected by TEA phase separation. Upon temperature increase and the consequent TEA phase separation, both the methine ^{1}H signal and the trifluoromethyl ^{19}F signal of HFiP displayed a small downfield shift together with significant signal broadening (Fig. 4B). In addition, a new signal appeared approximately 277 Hz away from the original peak in the ^{19}F NMR spectrum. The newly emerged peak originates from HFiP molecules inside the condensed phase, and its exchange between the two phases is expected to be slow on the NMR chemical shift timescale, *i.e.* slower than *ca.* 1700 s^{-1}. The presence of HFiP's exchange between the two TEA phases was subsequently supported by 2D ^{19}F, ^{19}F NOESY spectra, in which the two ^{19}F signals showed cross-peaks of the same sign, despite the rapid rotational dynamics of trifluoromethyl groups.

To quantify the kinetics of HFiP exchange between the two phases, we employed the heating–cooling cycles described above and performed 2D ^{19}F, ^{19}F EXSY experiments at five different mixing times from 15 to 120 ms (Fig. 4C and D). Analysis of the intensity build-up curves for the two exchange-related cross-peaks provided a k_{ex} of 16 ± 6 s^{-1}. The obtained k_{ex} value for the client HFiP is thus nearly half the value observed for the scaffold TEA molecules, suggesting that the exchange processes of the scaffold TEA and the client HFiP molecules are governed by different rate-determining steps.

In cells, the dynamic component exchange between membrane-less organelles and their environment enables their rapid formation and dissolution in response to regulatory signals.[19] In addition, the rapid recruitment and dynamic exchange of client molecules with the cellular environment are of utmost functional importance for some phase separated cellular bodies.[20,21] The exchange rates for the scaffold and client molecules are expected to vary over the course of non-equilibrium phase separation processes during which the size of phase-separated droplets, their number and consequently the total interface area between two phase changes (Fig. 4E).[4] Further changes in the exchange rates may be caused by droplet maturation processes, which affect the internal structure and properties of phase separated droplets.[29] Previous studies suggest that the phase separation of TEA obeys a nucleation-dependent kinetic regime,[30] resulting in alterations in the exchange rates depending on droplet size and numbers (Fig. 4E). Here, the reversibility of temperature-dependent TEA phase separation allowed us to develop a heating–cooling cycle experimental scheme and specifically target the "initial exchange rate" for both the scaffold TEA and the client HFiP molecules. Based on our results, we argue that it is important to carefully design exchange-related experiments and measure the

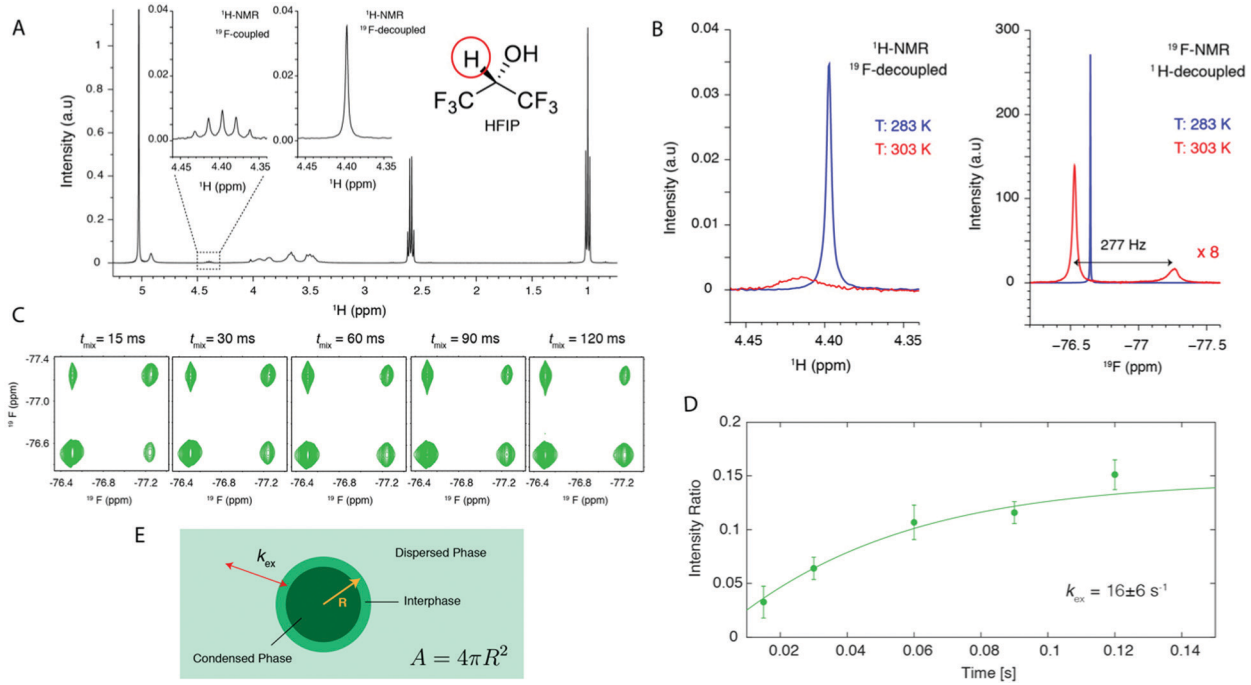

Fig. 4 ^{19}F-NMR based detection of chemical exchange of a fluorine-containing client molecule, HFiP, between dispersed and condensed triethylamine (TEA) phases. (A) 1D ^{1}H NMR spectrum of the TEA–water sample containing HFiP (1%, v/v), before induction of phase separation. The methine proton signal of HFiP is shown in ^{19}F-coupled or decoupled spectra. (B) The effect of TEA phase separation on the methine ^{1}H (left panel) and trifluoromethyl ^{19}F (right panel) signals of HFiP. (C) ^{19}F, ^{19}F EXSY spectra of HFiP, measured during the initial stage of TEA phase separation at five different mixing times, displaying mixing time-dependent intensity build-up of the correlation peak. (D) Quantitative analysis of intensity build-up curves yields the exchange rate, k_{ex}, of client molecules between two phases. Error bars are calculated by error propagation based on the spectral noise for each mixing time. (E) Schematic representation of the k_{ex} dependence on the size of droplets (*e.g.* their radius, R), hence the surface area, A, of the interphase between the two phases.

exchange rates at a clearly defined kinetic stage of the phase separation process. This will enable monitoring how various regulatory factors, *e.g.* (bio)chemical regulatory signals, alter the component exchange processes. Thus, comparison of the exchange rates between different client molecules and droplets provides mechanistic insights into the selective recruitment and spatial distribution of biomolecules inside cells.

Our results provide an example of how a multi-spin NMR approach can be employed in detecting and quantifying exchange processes during phase separation. In particular, we showed how a shift from more widely used nuclei such as ^{1}H and ^{13}C to ^{19}F may be beneficial in such studies. As shown for the client molecule HFiP (Fig. 4), the large sensitivity of ^{19}F nuclei to the chemical environment leads to a larger value for the chemical shift difference between the signals originated from the two phases ($\Delta\omega$, in s^{-1}), and at a given k_{ex}, by shifting the exchange regime further towards the slow-exchange regime (by decreasing the $k_{ex}/\Delta\omega$ ratio), facilitates exchange rate determination by NMR methods. In addition, the bio-orthogonality of fluorine atoms facilitates their use for biomolecular and biological samples, especially in the context of ''exchange-based'' small molecule screening against biomolecular targets inside membrane-less organelles.[28,31,32] The efficacy of drug candidates against biomolecular targets crucially relies on their pharmacokinetic properties ensuring their bio-availability.[33] Similar to the case of biomolecules located inside membrane-bound organelles, drugs have to be able to efficiently enter the phase separated membrane-less compartment. Quantitative determination of exchange rates of small molecules between separated phases is thus important. For example, it has been shown that the partitioning of anti-cancer drugs into nuclear condensates is determined by the physicochemical properties independent of their specific targets and influences their activity.[34] The NMR-based approach developed in the present study enables detection and quantification of the exchange processes between different phases and thereby is an important step towards ''exchange-based'' screening and optimization of small molecule drug candidates.

Conclusions

In summary, an NMR-based approach to study component exchange in phase separating systems is presented. Using triethylamine (TEA) as a model system exhibiting reversible temperature-induced phase separation, we detect and quantify the exchange processes for the scaffold TEA, as well as a client molecule. The developed approach allows the quantitative determination of the effects of regulatory factors on exchange processes and establishes

the basis for exchange-based small-molecule screening against biomolecular targets located inside the condensed phase.

Acronyms and symbols: TEA (triethylamine), HFIP (hexafluoroisopropanol), LLPS (liquid–liquid phase separation), LCST (lower critical solution temperature), LCST (lower critical solution temperature), DIC microscopy (differential interference contrast microscopy), NMR (nuclear magnetic resonance), HSQC (heteronuclear single quantum coherence), NOESY (nuclear Overhauser enhancement spectroscopy), ROESY (rotating frame Overhauser enhancement spectroscopy), EXSY (exchange spectroscopy), k_{ex} (chemical exchange rate), $\Delta\omega$ (chemical shift difference in s^{-1}).

Author contributions

C. F. P., M. Z. and N. R.-G.: conceptualization, funding acquisition, data curation; C. F. P.: investigation, visualization; C. F. P. and N. R.-G.: methodology, formal analysis; M. Z. and N. R.-G.: supervision; M. Z.: writing – review & editing; N. R.-G.: writing – original draft.

Conflicts of interest

There are no conflicts to declare.

Acknowledgements

C. F. P. acknowledges the Deutsche Akademischer Austauschdienst (DAAD) for Research Grants Doctoral programmes in Germany, 2019/20 (Personal ref. No. 91726791); M. Z. was supported by the European Research Council (ERC) under the EU Horizon 2020 research and innovation programme (grant agreement No. 787679). N. R.-G. acknowledges the Deutsche Forschungsgemeinschaft (German Research Foundation, DFG) for research grant RE 3655/2-3.

Notes and references

1 S. F. Banani, H. O. Lee, A. A. Hyman and M. K. Rosen, *Nat. Rev. Mol. Cell Biol.*, 2017, **18**, 285–298.
2 S. Alberti, *Curr. Biol.*, 2017, **27**, R1097–R1102.
3 E. Gomes and J. Shorter, *J. Biol. Chem.*, 2019, **294**, 7115–7127.
4 H. Falahati and A. Haji-Akbari, *Soft Matter*, 2019, **15**, 1135–1154.
5 S. Elbaum-Garfinkle, Y. Kim, K. Szczepaniak, C. C. Chen, C. R. Eckmann, S. Myong and C. P. Brangwynne, *Proc. Natl. Acad. Sci. U. S. A.*, 2015, **112**, 7189–7194.
6 J. Wang, J. M. Choi, A. S. Holehouse, H. O. Lee, X. Zhang, M. Jahnel, S. Maharana, R. Lemaitre, A. Pozniakovsky, D. Drechsel, I. Poser, R. V. Pappu, S. Alberti and A. A. Hyman, *Cell*, 2018, **174**, 688–699.
7 T. Yuwen, A. Bah, J. P. Brady, F. Ferrage, G. Bouvignies and L. E. Kay, *J. Phys. Chem. B*, 2018, **122**, 11206–11217.
8 S. Ambadipudi, J. G. Reddy, J. Biernat, E. Mandelkow and M. Zweckstetter, *Chem. Sci.*, 2019, **10**, 6503–6507.
9 L. Emmanouilidis, L. Esteban-Hofer, F. F. Damberger, T. de Vries, C. K. X. Nguyen, L. F. Ibanez, S. Mergenthal, E. Klotzsch, M. Yulikov, G. Jeschke and F. H. Allain, *Nat. Chem. Biol.*, 2021, **17**, 608–614.
10 J. C. Fuentes-Monteverde, S. Becker and N. Rezaei-Ghaleh, *Protein Sci.*, 2021, **30**, 1315–1325.
11 N. Rezaei-Ghaleh, F. Munari, S. Becker, M. Assfalg and C. Griesinger, *Chem. Commun.*, 2019, **55**, 12404–12407.
12 N. L. Fawzi, S. H. Parekh and J. Mittal, *Curr. Opin. Struct. Biol.*, 2021, **70**, 78–86.
13 C. P. Brangwynne, C. R. Eckmann, D. S. Courson, A. Rybarska, C. Hoege, J. Gharakhani, F. Julicher and A. A. Hyman, *Science*, 2009, **324**, 1729–1732.
14 P. R. Banerjee, A. N. Milin, M. M. Moosa, P. L. Onuchic and A. A. Deniz, *Angew. Chem., Int. Ed.*, 2017, **56**, 11354–11359.
15 L. Mediani, F. Antoniani, V. Galli, J. Vinet, A. D. Carra, I. Bigi, V. Tripathy, T. Tiago, M. Cimino, G. Leo, T. Amen, D. Kaganovich, C. Cereda, O. Pansarasa, J. Mandrioli, P. Tripathi, D. Troost, E. Aronica, J. Buchner, A. Goswami, J. Sterneckert, S. Alberti and S. Carra, *EMBO Rep.*, 2021, **22**, e51740.
16 S. F. Banani, A. M. Rice, W. B. Peeples, Y. Lin, S. Jain, R. Parker and M. K. Rosen, *Cell*, 2016, **166**, 651–663.
17 S. Ranganathan and E. Shakhnovich, *J. Phys. Chem. B*, 2021, **125**, 5035–5044.
18 K. M. Ruff, F. Dar and R. V. Pappu, *Proc. Natl. Acad. Sci. U. S. A.*, 2021, **118**, e2017184118.
19 Y. Shin and C. P. Brangwynne, *Science*, 2017, **357**, eaaf4382.
20 L. Galganski, M. O. Urbanek and W. J. Krzyzosiak, *Nucleic Acids Res.*, 2017, **45**, 10350–10368.
21 I. A. Sawyer, D. Sturgill, M. H. Sung, G. L. Hager and M. Dundr, *BioEssays*, 2016, **38**, 1197–1208.
22 F. Kohler and O. K. Rice, *J. Chem. Phys.*, 1957, **26**, 1614–1618.
23 B. J. Hales, G. L. Bertrand and L. G. Hepler, *J. Phys. Chem.*, 1966, **70**, 3970.
24 A. N. Campbell and E. M. Kartzmar, *Can. J. Chem.*, 1969, **47**, 619.
25 S. Kajimoto, N. H. Seong, H. Fukumura and D. D. Dlott, *Photochem. Photobiol. Sci.*, 2014, **13**, 891–897.
26 R. Behrends, T. Telgmann and U. Kaatze, *J. Chem. Phys.*, 2002, **117**, 9828–9837.
27 D. V. Fenby, Z. S. Kooner and J. R. Khurma, *Fluid Phase Equilib.*, 1981, **7**, 327–338.
28 J. L. Kitevski-LeBlanc and R. S. Prosser, *Prog. Nucl. Magn. Reson. Spectrosc.*, 2012, **62**, 1–33.
29 M. Feric, N. Vaidya, T. S. Harmon, D. M. Mitrea, L. Zhu, T. M. Richardson, R. W. Kriwacki, R. V. Pappu and C. P. Brangwynne, *Cell*, 2016, **165**, 1686–1697.
30 J. Hobley, S. Kajimoto, A. Takamizawa, K. Ohta, Q. Tran-Cong and H. Fukumura, *J. Phys. Chem. B*, 2003, **107**, 11411–11418.
31 A. Boeszoermenyi, B. Ogorek, A. Jain, H. Arthanari and G. Wagner, *J. Biomol. NMR*, 2020, **74**, 365–379.

32 C. R. Buchholz and W. C. K. Pomerantz, *RSC Chem. Biol.*, 2021, **2**, 1312–1330.
33 J. P. Hughes, S. Rees, S. B. Kalindjian and K. L. Philpott, *Br. J. Pharmacol.*, 2011, **162**, 1239–1249.
34 I. A. Klein, A. Boija, L. K. Afeyan, S. W. Hawken, M. Fan, A. Dall'Agnese, O. Oksuz, J. E. Henninger, K. Shrinivas, B. R. Sabari, I. Sagi, V. E. Clark, J. M. Platt, M. Kar, P. M. McCall, A. V. Zamudio, J. C. Manteiga, E. L. Coffey, C. H. Li, N. M. Hannett, Y. E. Guo, T. M. Decker, T. I. Lee, T. Zhang, J. K. Weng, D. J. Taatjes, A. Chakraborty, P. A. Sharp, Y. T. Chang, A. A. Hyman, N. S. Gray and R. A. Young, *Science*, 2020, **368**, 1386–1392.

How to cite: *Angew. Chem. Int. Ed.* **2023,** *62,* e202218078
International Edition: doi.org/10.1002/anie.202218078
German Edition: doi.org/10.1002/ange.202218078

NMR

Determining the Physico-Chemical Composition of Biomolecular Condensates from Spatially-Resolved NMR

*Christian F. Pantoja, Alain Ibáñez de Opakua, Maria-Sol Cima-Omori, and Markus Zweckstetter**

Abstract: Liquid-Liquid phase separation has emerged as fundamental process underlying the formation of biomolecular condensates. Insights into the composition and structure of biomolecular condensates is, however, complicated by their molecular complexity and dynamics. Here, we introduce an improved spatially-resolved NMR experiment that enables quantitative analysis of the physico-chemical composition of multi-component biomolecular condensates in equilibrium and label-free. Application of spatially-resolved NMR to condensates formed by the Alzheimer's disease-associated protein Tau demonstrates decreased water content, exclusion of the molecular crowding agent dextran, presence of a specific chemical environment of the small molecule DSS, and ≈150-fold increased concentration of Tau inside the condensate. The results suggest that spatially-resolved NMR can have a major impact in understanding the composition and physical chemistry of biomolecular condensates.

Biomolecular condensation of proteins and nucleic acids is implicated in a wide range of biological processes and human diseases.[1] Formation of biomolecular condensates in cells is linked to the physico-chemical process of liquid-liquid phase separation (LLPS) of molecular components.[2] Multivalent interactions involving intrinsically disordered proteins (IDPs) and low-complexity domains are often essential in promoting LLPS and biomolecular condensation.[3] Small-molecule therapeutics concentrate in protein condensates affecting drug activity.[4] Small molecule partitioning also affects the formation and properties of biomolecular condensates as demonstrated for adenosine triphosphate.[5] In addition, hydration plays an important role in the formation and regulation of biomolecular condensates.[6]

Due to the molecular complexity and dynamic nature of condensates, effective tools to investigate their composition and structure are required. This is the case for biomolecular condensates in cells, which often contain hundreds of proteins and nucleic acids.[1] Even for biomolecular condensates reconstituted in vitro from a limited number of components, however, it is challenging to obtain accurate component quantification.[7] This is particularly the case for water and other small molecules, which often cannot be labeled to allow their selective observation and thus quantification inside multicomponent condensates. In addition, available approaches for quantification of even single components are often performed under non-equilibrium conditions and thus do not fully capture the dynamic nature of biomolecular condensates. Here, we show that these challenges can be overcome through improved spatially-resolved NMR, providing quantitative insights into the composition of multicomponent condensates in equilibrium and label-free.

To be able to study biomolecular condensates in equilibrium, we phase separated the 441-residue IDP Tau (Figure S1; Table S1) with the molecular crowding agent dextran, centrifuged the sample and formed a macroscopic condensate at the bottom of the NMR tube (Figure 1a, left). In contrast to previous approaches,[8] the Tau condensate does not cover the full length of the NMR tube, but the condensate as well as the dilute phase contribute to the NMR signal. To achieve high sample and temperature stability, we used a coaxial NMR sample setup combining an inner Shigemi tube and an external tube filled with methanol-d_4 for temperature control (Figure 1a left; Figure S2). We then mapped the signal intensity of the water signal along the z-axis by applying a permanent gradient during the NMR acquisition period (Figure S3). For a uniformly mixed, non-phase separated sample, we observed the typical bell-shaped profile that represents the spin density along the z-axis (Figure 1a, right, grey). In the case of the Tau condensate sample, an intensity drop occurred in the region from ≈9–13 mm (Figure 1a, right, black). The intensity drop suggests a reduction of 18.8 ± 0.5 % water content in the protein-rich phase compared to the protein-dilute upper phase (Figure S4).

An additional challenge for spatially-resolved NMR of biomolecular condensates, is the suppression of the water resonance. Highly efficient water suppression is necessary,

[*] C. F. Pantoja, Dr. A. Ibáñez de Opakua, M.-S. Cima-Omori, Prof. Dr. M. Zweckstetter
German Center for Neurodegenerative Diseases (DZNE)
Von-Siebold-Str. 3a, 37075 Göttingen (Germany)
E-mail: Markus.Zweckstetter@dzne.de
Prof. Dr. M. Zweckstetter
Max Planck Institute for Multidisciplinary Sciences
Am Faßberg 11, 37077 Göttingen (Germany)

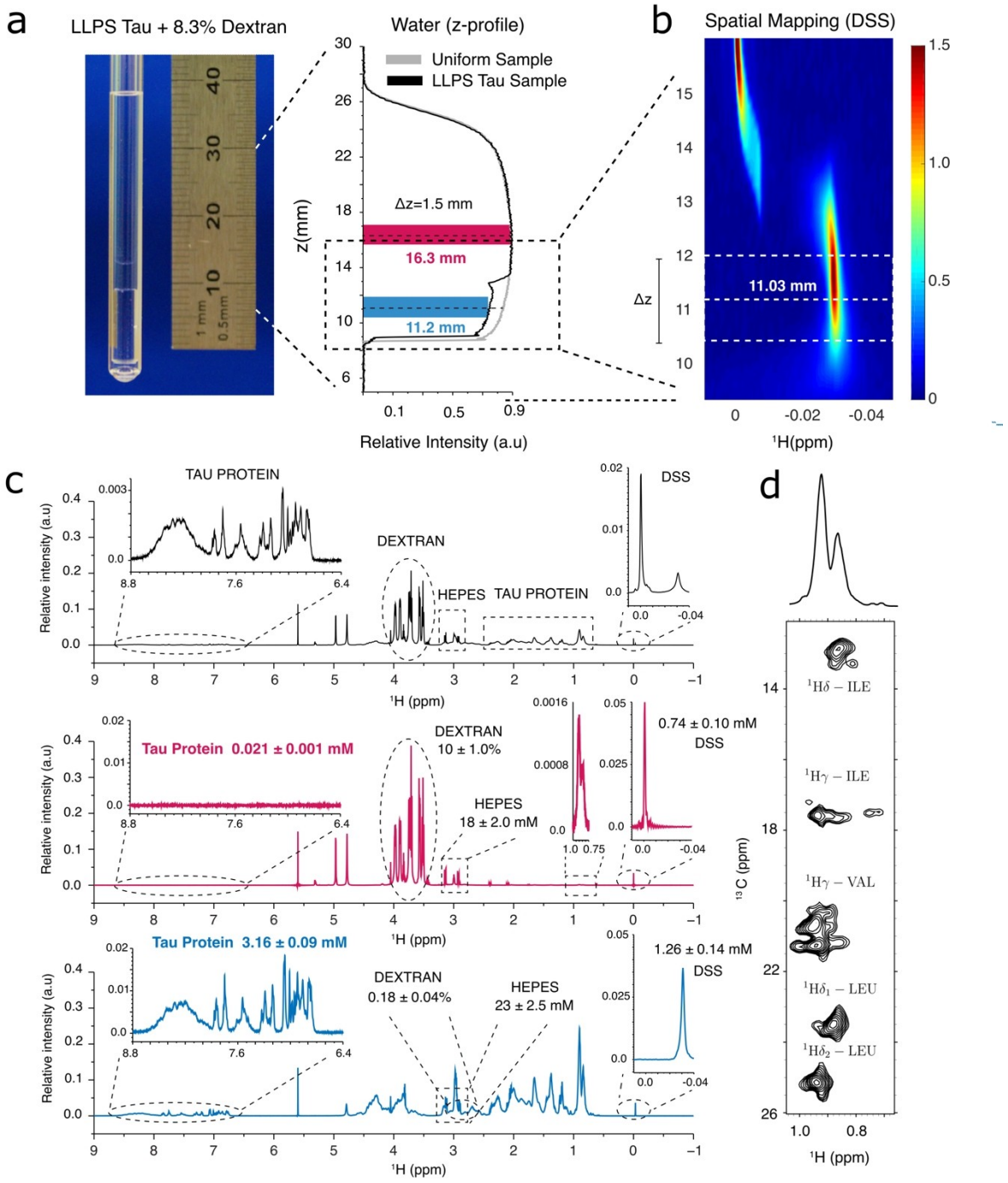

Figure 1. Label-free multi-component quantification of Tau condensates by spatially-resolved NMR spectroscopy. a) Slice-selective detection of NMR spectra of the condensed and dilute protein phase in equilibrium. Tau phase separation was promoted with 8.3% dextran (left). (Right) z-profile experiment monitoring the signal of water along the NMR coil in a uniformly mixed reference sample (grey) and the Tau condensate sample (black). The positions and widths of the gradient-selected slices of the dilute (pink) and condensed phase (blue) are marked. b) DSS signal along the *z*-axis monitored by slice-selective WET-DPFGSE. The ^{1}H chemical shift of DSS in the dilute phase was set to 0 ppm. Signal intensities are color coded from blue to red. c) ^{1}H NMR spectra of the condensed (blue) and dilute phase (pink) recorded with WET-DPFGSE at 25 °C. A standard ^{1}H WET NMR spectrum without slice selection (black) is shown for comparison. Concentrations of the individual components are indicated. d) Non-selective ^{1}H-^{13}C HSQC of the methyl region of the Tau condensate sample. The observed cross peaks arise mostly from the protein-dense lower phase.

in order to be able to quantify the $\approx 10^{5}$–10^{6} lower concentrated protein and small molecule components in the condensate. However, most of the well-known water suppression methods are not compatible with spatial encod-

ing elements. To overcome this limitation, we introduced the water suppression enhanced through T_1 effects (WET) pulse sequence element[9] into the slice-selective Doubled Pulsed Field Gradient Selective Echo (DPFGSE) pulse sequence[10] (Figure S5). The WET block is placed before the slice selection element and avoids saturation of the protein resonances.

We then applied the spatially-resolved WET-DPFGSE NMR pulse sequence to the two-phase condensate sample of Tau. Using a magnetic field gradient together with selective NMR pulses, we selectively detected 1.5 mm thick slices along the *z*-axis of the phase-separated sample (Figure 1a, right). The slice thickness chosen covers a spectral width of 10 ppm ($\Delta\omega \approx 7$ kHz at 700 MHz) ensuring a good compromise between signal-to-noise ratio and spatial selectivity. The two slices were positioned near the center of each phase, where maximum magnetic field homogeneity was present (Figure 1a). This is important, because in phase separated systems magnetic susceptibility changes at the interphase region cause NMR line broadening associated with B_0 inhomogeneities.[11] In addition, non-negligible slice thicknesses require careful positioning of the slices in order to ensure that the acquired NMR signals belong to the desired phase. To further support the selection of the slice positions, we mapped the NMR signal of the reference compound sodium 3-(trimethylsilyl) propane-1-sulfonate (DSS) along the *z*-axis. In a slice of $\approx$1.5 mm, we detected the maximum signal intensity of DSS inside the Tau condensate (Figure 1b).

We then recorded slice-selective, one-dimensional ^{1}H NMR spectra in the condensed lower and the dilute upper phase of the Tau condensate (Figure 1c). In the dilute upper phase, we detected the NMR signals of Tau, dextran, DSS, and 4-(2-hydroxyethyl)-1-piperazineethanesulfonic acid (HEPES). In the condensed lower phase, the NMR signals of Tau, DSS and HEPES were present (Figure 1c). Only very weak signals of dextran were observed in the Tau condensate, indicating that the molecular crowding agent is largely excluded from the condensate (Figure S5). In contrast, the Tau protein was strongly enriched in the condensate (Figure 1c). For quantification (see Methods section), we selected Tau's methyl signals that can provide the most favorable signal-to-noise ratio and retain high mobility even in the condensate (Figure 1c,d; Table S2). The analysis determined the Tau concentration in the dilute and condensed phase as 0.021 ± 0.001 mM and 3.16 ± 0.09 mM, respectively (Figure 1c and S6). The Tau concentration in the condensate is thus 150-fold higher than in the dilute phase.

The improved spatially-resolved NMR experiment also allowed us to quantifiy the concentrations of dextran, DSS and buffer in both phases (Figure 1c and S6; Table S2): 10 ± 1 % and 0.18 ± 0.04 % dextran in the upper and lower phase, respectively; 0.74 ± 0.10 mM and 1.26 ± 0.14 mM DSS, respectively, corresponding to a partition coefficient of 1.7 ± 0.3 in the condensed lower phase; 18.0 ± 1.9 mM and 23.0 ± 2.5 mM HEPES, i.e. a $\approx$30 % enrichment of HEPES in the condensed phase. We further note that the DSS signal is shifted by $\approx$0.03 ppm to lower chemical shift compared to the dilute phase, demonstrating that DSS experiences a distinct chemical environment in the protein-dense lower phase.

Next, we investigated the temperature-dependence of Tau condensation. To this end, we prepared a Tau condensate without crowding agent. Consistent with previous studies,[12] we observed Tau phase separation in a low ionic strength buffer. Supported by centrifugation, two stable phases were formed. The phase-separated sample was then stored at 4 °C for one week to ensure that the system reached equilibrium. The concentrations of Tau in both the condensate and the dilute phase were subsequently quantified using the novel WET-DPFGSE NMR experiment at stepwise increasing temperatures (Figure 2a). Raising the temperature from 5 to 10 °C and from 10 to 15 °C, increased the Tau concentration in the condensed phase by 2.4–7.4 % in each step (Figure 2a; blue lower row). In parallel, the concentration of Tau in the dilute phase was decreased (Figure 2a, red upper row). Increase of the temperature to 20, 25, 30 and 35 °C further increased the Tau concentration in the condensed phase. At 35 °C, the Tau concentration in the condensate was $\approx$46 % higher than at 5 °C (Figure 2a).

Real time monitoring of the Tau concentration during the temperature jump experiment using spatially-resolved NMR, further highlights the importance of reaching equilibrium prior to determining phase diagrams. After raising the temperature by 5 °C, approximately 2 hrs were required before a stable Tau concentration in the condensate was reached (Figure 2b). Even after 5 hrs, the concentration in the dilute phase was still slightly decreasing at temperatures $<$25 °C (Figure 2a, upper row). In addition, the differences between peak height and peak intensity changes in the condensed phase when raising the temperature suggest that chemical exchange processes or temperature-induced sample inhomogeneities contribute to peak broadening and thus affect more strongly the peak height.[13]

Previous studies showed that Tau can experience lower critical solution temperature (LCST) or upper critical solution temperature (UCST) phase separation in a context-dependent manner[14] This assessment has profound implications related to the kinetic process. For systems that undergo LCST, the system is undergoing, after temperature increase, demixing driven by nucleation or spinodal decomposition.[15] Contrary, in systems that display UCST the next equilibrium condition is reached mainly by diffusion. Visual inspection showed that the Tau-rich phase turned turbid when the temperature was raised (Figure S7). This observation is consistent with an entropy-driven nucleation process driven by water in the condensed phase. Nucleation sites rich in water are formed and after fusion are expelled from the protein-rich phase. Consequently, the protein concentration increases along with a "dehydration process" of the lower phase. In the dilute upper phase, no turbidity was visible likely because of less extensive protein nucleation due to the lower Tau concentration.

After reaching constant Tau signal intensities, a z-profile experiment was recorded at each temperature (Figure 2c). The temperature-dependent z-profiles of the water resonance showed that the height of the condensed phase

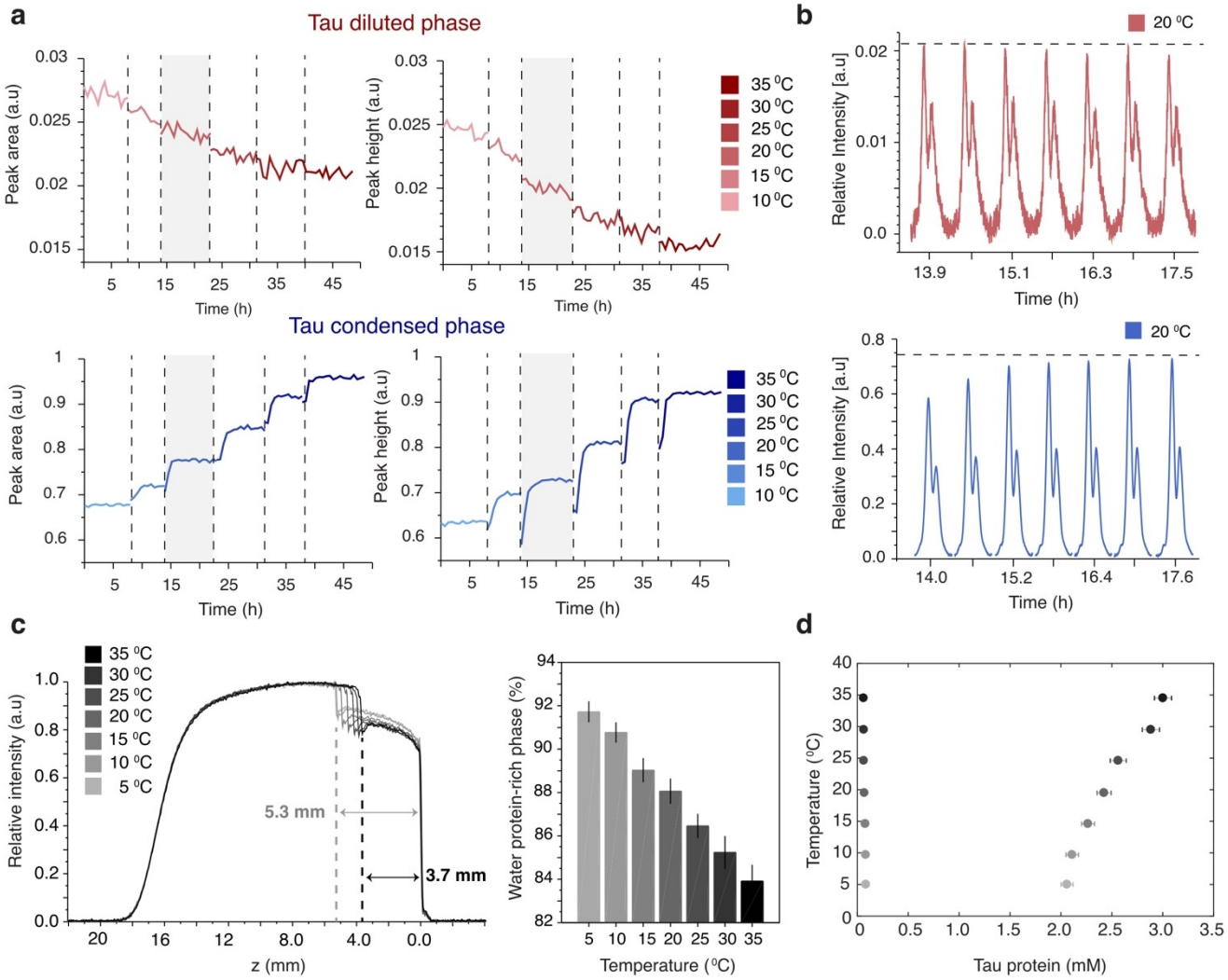

Figure 2. Kinetics of Tau condensation followed by spatially-resolved NMR. a), b) Time-dependent area and height of the methyl signals of Tau in the condensed (blue, lower panels) and dilute (red, upper panels) phase in temperature-jump experiments. The Tau condensate was formed at low ionic strength without dextran. NMR spectra of the two phases were recorded using the slice-selective WET-DPFGSE experiment. Vertical dashed lines mark temperature changes (see legend). b) Time-dependent WET-DPFGSE methyl signals observed after temperature jump from 15 to 20 °C (marked in grey in (a)). Dashed lines indicate near equilibrium condition. c) z-profile experiments recorded after the system reached near equilibrium. (Right) Relative amount of water in the protein-rich phase calculated from the normalized z-profile. d) Phase diagram of Tau determined by spatially-resolved NMR. Tau concentrations in the diluted and condensed phase (at/near equilibrium) determined in the slice-selective NMR spectra are displayed (see also Table S3). Error bars are based on signal-to-noise ratios in the spectra and the uncertainty in the concentration of the reference Tau sample. All NMR spectra were recorded at a 700 MHz NMR spectrometer.

decreased with increasing temperature. At 35 °C, the height was 30 % smaller than at 5 °C (0.3736 ± 0.0002 cm at 35 °C vs 0.5324 ± 0.0002 cm at 5 °C; Figure 2c). Using the information provided by the z-profile experiment, the amount of water in the Tau condensed phase was then estimated. At 5 °C, we observed an 8.28 % decrease in water content in the condensed phase when compared with the dilute phase. At 35 °C, the decrease in water content in the condensed phase reached 16 %. The compaction of the condensed phase thus likely arises from the decrease in water content in the condensed phase with increasing temperature, in agreement with the importance of dehydration for LLPS.[16]

In order to determine the phase diagram of Tau, the areas under the methyl proton signals, which were measured after reaching equilibrium, were converted into Tau concentrations (see Methods section). The Tau concentrations in the condensed and dilute phase represent the high and low concentration part of the phase diagram (Figure 2d). At 5 °C, the Tau molar concentration is ≈32 % lower than at 35 °C ($[Tau]_{35°C}$: 3.0 mM and $[Tau]_{5°C}$: 2.0 mM), in agreement with the percentage of compaction observed by the z-profile experiments (Figure 2c). In parallel, the Tau concentration in the dilute phase was decreased by ≈26 % in the studied temperature range (Figure 2c).

We showed that improved spatially-resolved NMR enables the quantification of multiple components in biomolecular condensates in equilibrium and label-free. Protein, small molecules and water can be simultaneously quantified with high reliability in both the condensed and dilute phase. Multi-component quantification can be performed in a temperature-dependent manner in real time providing insight into the kinetics of condensation processes. The improved WET-DPFGSE NMR experiment thus complements and extends previous NMR approaches that relied on the use of fluorinated molecules for quantification of protein or small molecule concentrations in phase-separated systems.[13,17] In addition, Raman microscopy can be useful to quantify protein concentrations, on the basis of the signals emerging from the different amounts of water present in the condensed and dilute phase.[18]

The improved spatially-resolved NMR is applicable to effectively any IDP as long as its NMR resonances are observable. Protein concentrations determined by spatially-resolved NMR characterize protein phase diagrams with high reliability. This will be important to better understand the mechanisms that drive the phase separation of IDPs and their modulation by disease-associated mutations and post-translational modifications. The high reliability of phase diagrams determined by spatially-resolved NMR will also be important to improve current computational methods which explore the molecular forces that govern biomolecular phase transitions.[19] We further expect that the ability to simultaneously observe proteins, small molecules and water will provide critical guidance in understanding the partitioning into and modulation of biomolecular condensates by small molecules. Importantly, spatially resolved NMR is not restricted to the simultaneous quantification of the concentration of proteins, small molecules and water in phase separated systems, but is also sensitive to differences in the chemical environment in the two phases.

Acknowledgements

C.F.P. acknowledges the Deutscher Akademischer Austauschdienst (DAAD) for the Research Grants Doctoral program in Germany, 2019/20 (personal ref. no. 91726791). M.Z. was supported by the European Research Council (ERC) under the EU Horizon 2020 research and innovation program (grant agreement no. 787679). Open Access funding enabled and organized by Projekt DEAL.

Conflict of Interest

The authors declare no conflict of interest.

Data Availability Statement

The data that support the findings of this study are available in the Supporting Information of this article.

Keywords: Biomolecular condensates · Spatially-resolved NMR · Multicomponent quantification · Phase diagram · Tau protein

[1] a) S. F. Banani, H. O. Lee, A. A. Hyman, M. K. Rosen, *Nat. Rev. Mol. Cell Biol.* **2017**, *18*, 285–298; b) S. Alberti, A. A. Hyman, *Nat. Rev. Mol. Cell Biol.* **2021**, *22*, 196–213.

[2] A. A. Hyman, C. A. Weber, F. Jülicher, *Annu. Rev. Cell Dev. Biol.* **2014**, *30*, 39–58.

[3] J. M. Choi, A. S. Holehouse, R. V. Pappu, *Annu. Rev. Biophys.* **2020**, *49*, 107–133.

[4] I. A. Klein, A. Boija, L. K. Afeyan, S. W. Hawken, M. Fan, A. Dall'Agnese, O. Oksuz, J. E. Henninger, K. Shrinivas, B. R. Sabari, I. Sagi, V. E. Clark, J. M. Platt, M. Kar, P. M. McCall, A. V. Zamudio, J. C. Manteiga, E. L. Coffey, C. H. Li, N. M. Hannett, Y. E. Guo, T. M. Decker, T. I. Lee, T. Zhang, J. K. Weng, D. J. Taatjes, A. Chakraborty, P. A. Sharp, Y. T. Chang, A. A. Hyman, N. S. Gray, R. A. Young, *Science* **2020**, *368*, 1386–1392.

[5] a) A. Patel, L. Malinovska, S. Saha, J. Wang, S. Alberti, Y. Krishnan, A. A. Hyman, *Science* **2017**, *356*, 753–756; b) N. A. Yewdall, A. A. M. Andre, M. H. I. van Haren, F. H. T. Nelissen, A. Jonker, E. Spruijt, *Biophys. J.* **2022**, *121*, 3962–3974.

[6] a) Y. Dorone, S. Boeynaems, E. Flores, B. Jin, S. Hateley, F. Bossi, E. Lazarus, J. G. Pennington, E. Michiels, M. De Decker, K. Vints, P. Baatsen, G. W. Bassel, M. S. Otegui, A. S. Holehouse, M. Exposito-Alonso, S. Sukenik, A. D. Gitler, S. Y. Rhee, *Cell* **2021**, *184*, 4284–4298; b) J. Ahlers, E. M. Adams, V. Bader, S. Pezzotti, K. F. Winklhofer, J. Tatzelt, M. Havenith, *Biophys. J.* **2021**, *120*, 1266–1275.

[7] a) A. V. Ceballos, C. J. McDonald, S. Elbaum-Garfinkle, *Methods Enzymol.* **2018**, *611*, 31–50; b) N. M. Milkovic, T. Mittag, *Methods Mol. Biol.* **2020**, *2141*, 685–702; c) G. A. Mountain, C. D. Keating, *Methods Enzymol.* **2021**, *646*, 115–142; d) A. Bremer, A. E. Posey, M. B. Borgia, W. M. Borcherds, M. Farag, R. V. Pappu, T. Mittag, *Biomol. Eng.* **2022**, *12*, 1480.

[8] a) A. C. Murthy, N. L. Fawzi, *J. Biol. Chem.* **2020**, *295*, 2375–2384; b) L. E. Wong, T. H. Kim, D. R. Muhandiram, J. D. Forman-Kay, L. E. Kay, *J. Am. Chem. Soc.* **2020**, *142*, 2471–2489; c) B. E. Ackermann, G. T. Debelouchina, *Angew. Chem. Int. Ed.* **2019**, *58*, 6300–6305; *Angew. Chem.* **2019**, *131*, 6366–6371; d) J. C. Fuentes-Monteverde, S. Becker, N. Rezaei-Ghaleh, *Protein Sci.* **2021**, *30*, 1315–1325; e) A. C. Murthy, G. L. Dignon, Y. Kan, G. H. Zerze, S. H. Parekh, J. Mittal, N. L. Fawzi, *Nat. Struct. Mol. Biol.* **2019**, *26*, 637–648; f) J. P. Brady, P. J. Farber, A. Sekhar, Y. H. Lin, R. Huang, A. Bah, T. J. Nott, H. S. Chan, A. J. Baldwin, J. D. Forman-Kay, L. E. Kay, *Proc. Natl. Acad. Sci. USA* **2017**, *114*, E8194–E8203.

[9] a) R. J. Ogg, P. B. Kingsley, J. S. Taylor, *J. Magn. Reson. Ser. B* **1994**, *104*, 1–10; b) S. H. Smallcombe, S. L. Patt, P. A. Keifer, *J. Magn. Reson. Ser. A* **1995**, *117*, 295–303.

[10] a) W. Kozminski, *Pol. J. Chem.* **2000**, *74*, 1185–1189; b) K. Stott, J. Stonehouse, J. Keeler, T.-L. Hwang, A. J. Shaka, *J. Am. Chem. Soc.* **1995**, *117*, 4199–4200; c) J. N. Dumez, *Prog. Nucl. Magn. Reson. Spectrosc.* **2018**, *109*, 101–134.

[11] B. T. Martin, G. C. Chingas, O. M. McDougal, *J. Magn. Reson.* **2012**, *218*, 147–152.

[12] T. Ukmar-Godec, S. Hutten, M. P. Grieshop, N. Rezaei-Ghaleh, M. S. Cima-Omori, J. Biernat, E. Mandelkow, J. Soding, D. Dormann, M. Zweckstetter, *Nat. Commun.* **2019**, *10*, 2909.

[13] a) C. F. Pantoja, M. Zweckstetter, N. Rezaei-Ghaleh, *Phys. Chem. Chem. Phys.* **2022**, *24*, 6169–6175; b) J. E. Bramham, A. P. Golovanov, *Nat. Commun.* **2022**, *13*, 1767.

[14] a) Y. Lin, J. McCarty, J. N. Rauch, K. T. Delaney, K. S. Kosik, G. H. Fredrickson, J. E. Shea, S. Han, *eLife* **2019**, *8*, e42571; b) S. Najafi, Y. Lin, A. P. Longhini, X. Zhang, K. T. Delaney, K. S. Kosik, G. H. Fredrickson, J. E. Shea, S. Han, *Protein Sci.* **2021**, *30*, 1393–1407; c) S. K. Rai, A. Savastano, P. Singh, S. Mukhopadhyay, M. Zweckstetter, *Protein Sci.* **2021**, *30*, 1294–1314.
[15] K. Binder, *Rep. Prog. Phys.* **1987**, *50*, 783–859.
[16] S. Park, R. Barnes, Y. Lin, B.-j. Jeon, S. Najafi, K. T. Delaney, G. H. Fredrickson, J. E. Shea, D. S. Hwang, S. Han, *Commun. Chem.* **2020**, *3*, 83.
[17] J. Niu, C. Qiu, N. L. Abbott, S. H. Gellman, *J. Am. Chem. Soc.* **2022**, *144*, 10386–10395.
[18] K. Yokosawa, S. Kajimoto, D. Shibata, K. Kuroi, T. Konno, T. Nakabayashi, *J. Phys. Chem. Lett.* **2022**, *13*, 5692–5697.
[19] a) Y.-H. Lin, J. Song, J. D. Forman-Kay, H. S. Chan, *J. Mol. Liq.* **2017**, *228*, 176–193; b) J. McCarty, K. T. Delaney, S. P. O. Danielsen, G. H. Fredrickson, J.-E. Shea, *J. Phys. Chem. Lett.* **2019**, *10*, 1644–1652; c) X. Zeng, A. S. Holehouse, A. Chilkoti, T. Mittag, R. V. Pappu, *Biophys. J.* **2020**, *119*, 402–418.

Manuscript received: December 7, 2022
Accepted manuscript online: February 27, 2023
Version of record online: March 15, 2023

Molecular Cell

Article

Condensed-phase signaling can expand kinase specificity and respond to macromolecular crowding

Graphical abstract

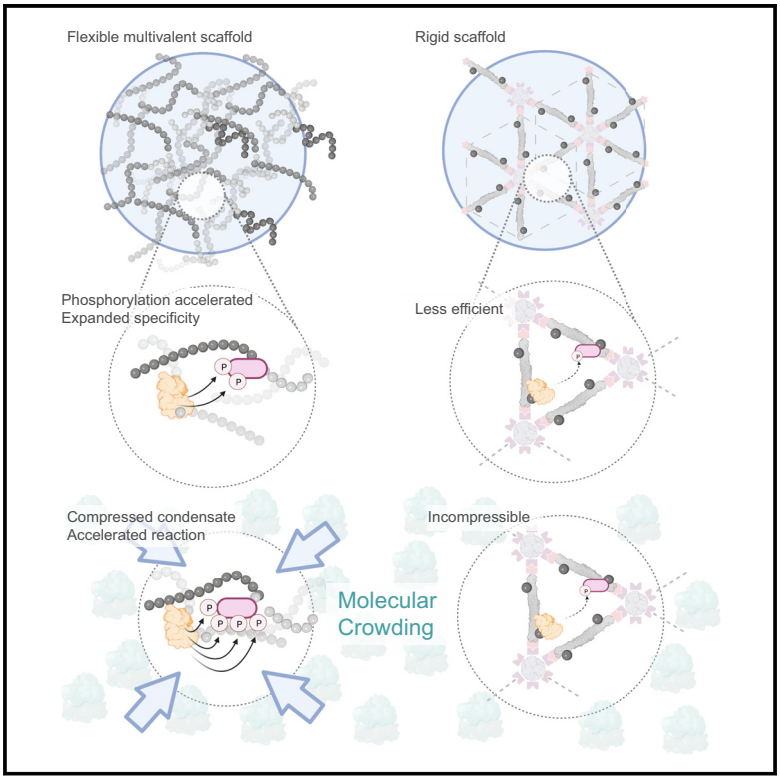

Authors

Dajun Sang, Tong Shu, Christian F. Pantoja, Alain Ibáñez de Opakua, Markus Zweckstetter, Liam J. Holt

Correspondence

mazw@mpinat.mpg.de (M.Z.), liam.holt@nyulangone.org (L.J.H.)

In brief

Sang et al. use synthetic biology to demonstrate that phase-separated biomolecular condensates can potentiate kinase signaling. Synthetic condensates allow the systematic exploration of features required for efficient signaling and responsiveness to biophysical cues. Finally, phase separation accelerates Alzheimer's-associated phosphorylation events.

Highlights

- Synthetic condensates enable the creation of dynamic phosphoregulation
- Kinases in condensates can phosphorylate unexpected peptides
- Kinases in condensates can convert biophysical information to chemical signals
- Alzheimer's-associated phosphorylation is accelerated by phase separation

Sang et al., 2022, Molecular Cell *82*, 3693–3711
October 6, 2022
https://doi.org/10.1016/j.molcel.2022.08.016

CellPress

Molecular Cell

CellPress
OPEN ACCESS

Article

Condensed-phase signaling can expand kinase specificity and respond to macromolecular crowding

Dajun Sang,[1] Tong Shu,[1] Christian F. Pantoja,[2] Alain Ibáñez de Opakua,[2] Markus Zweckstetter,[2,3,*] and Liam J. Holt[1,4,*]
[1]Institute for Systems Genetics, New York University Langone Medical Center, 435 E 30th Street, New York, NY 10010, USA
[2]German Center for Neurodegenerative Diseases (DZNE), Von-Siebold-Str. 3a, 37075 Göttingen, Germany
[3]Max Planck Institute for Multidisciplinary Sciences, Department of NMR-based Structural Biology, Am Fassberg 11, 37077 Göttingen, Germany
[4]Lead contact
*Correspondence: mazw@mpinat.mpg.de (M.Z.), liam.holt@nyulangone.org (L.J.H.)
https://doi.org/10.1016/j.molcel.2022.08.016

SUMMARY

Phase separation can concentrate biomolecules and accelerate reactions. However, the mechanisms and principles connecting this mesoscale organization to signaling dynamics are difficult to dissect because of the pleiotropic effects associated with disrupting endogenous condensates. To address this limitation, we engineered new phosphorylation reactions within synthetic condensates. We generally found increased activity and broadened kinase specificity. Phosphorylation dynamics within condensates were rapid and could drive cell-cycle-dependent localization changes. High client concentration within condensates was important but not the main factor for efficient phosphorylation. Rather, the availability of many excess client-binding sites together with a flexible scaffold was crucial. Phosphorylation within condensates was also modulated by changes in macromolecular crowding. Finally, the phosphorylation of the Alzheimer's-disease-associated protein Tau by cyclin-dependent kinase 2 was accelerated within condensates. Thus, condensates enable new signaling connections and can create sensors that respond to the biophysical properties of the cytoplasm.

INTRODUCTION

Eukaryotic cells use membrane bound organelles for spatiotemporal control of complex biochemical reactions, and there is increasing evidence for the importance of membraneless subcellular compartments, such as nucleoli or stress granules (Banani et al., 2017). These biomolecular condensates can be highly dynamic and sometimes form through liquid-liquid phase separation (LLPS) (Shin and Brangwynne, 2017). Recent research has revealed mechanisms of condensate formation, but it has been more difficult to demonstrate the importance of LLPS for the modulation of biochemical reactions.

It is difficult to understand the impact of condensation on biological regulation because mutations that disrupt LLPS or that perturb recruitment of clients to condensates can have pleiotropic effects. For example, although it is possible to mutate a protein sequence such that it fails to undergo LLPS, any associated loss of activity could be due to this loss of condensation or equally could be due to an unrelated loss of intrinsic protein function. A handful of studies have attempted to address this problem through orthogonal reconstitution of the condensation behavior. For example, chimeras of NELF condensates that recovered condensate formation and basic function but lost stress inducibility (Rawat et al., 2021). However, there are few examples, and they failed to fully rescue biological functions, illustrating our incomplete understanding of principles.

Synthetic biology is a powerful approach to investigate general principles while avoiding pleiotropic effects that can confound interpretation. For example, synthetic optogenetic systems, including "OptoDroplets" and "Corelets," were developed to exert spatiotemporal control of phase transitions in cells, permitting quantitative mapping of intracellular phase diagrams (Bracha et al., 2019; Shin et al., 2017).

The complex cellular environment can strongly affect LLPS. The cell interior is crowded, both in the cytosol and nucleus. Up to 40% of the cell volume is excluded by macromolecules (Delarue et al., 2018; Ellis and Minton, 2003; Luby-Phelps, 1999). Recent studies revealed that mTORC1 modulates cytoplasmic crowding by tuning ribosome concentration, and this has strong effects on phase separation (Delarue et al., 2018). In the nucleus, the chromatin network can mechanically suppress the coalescence of OptoDroplets, impacting condensate number, size, and placement (Lee et al., 2021; Zhang et al., 2021b). Since the crowded, active cell interior modulates phase

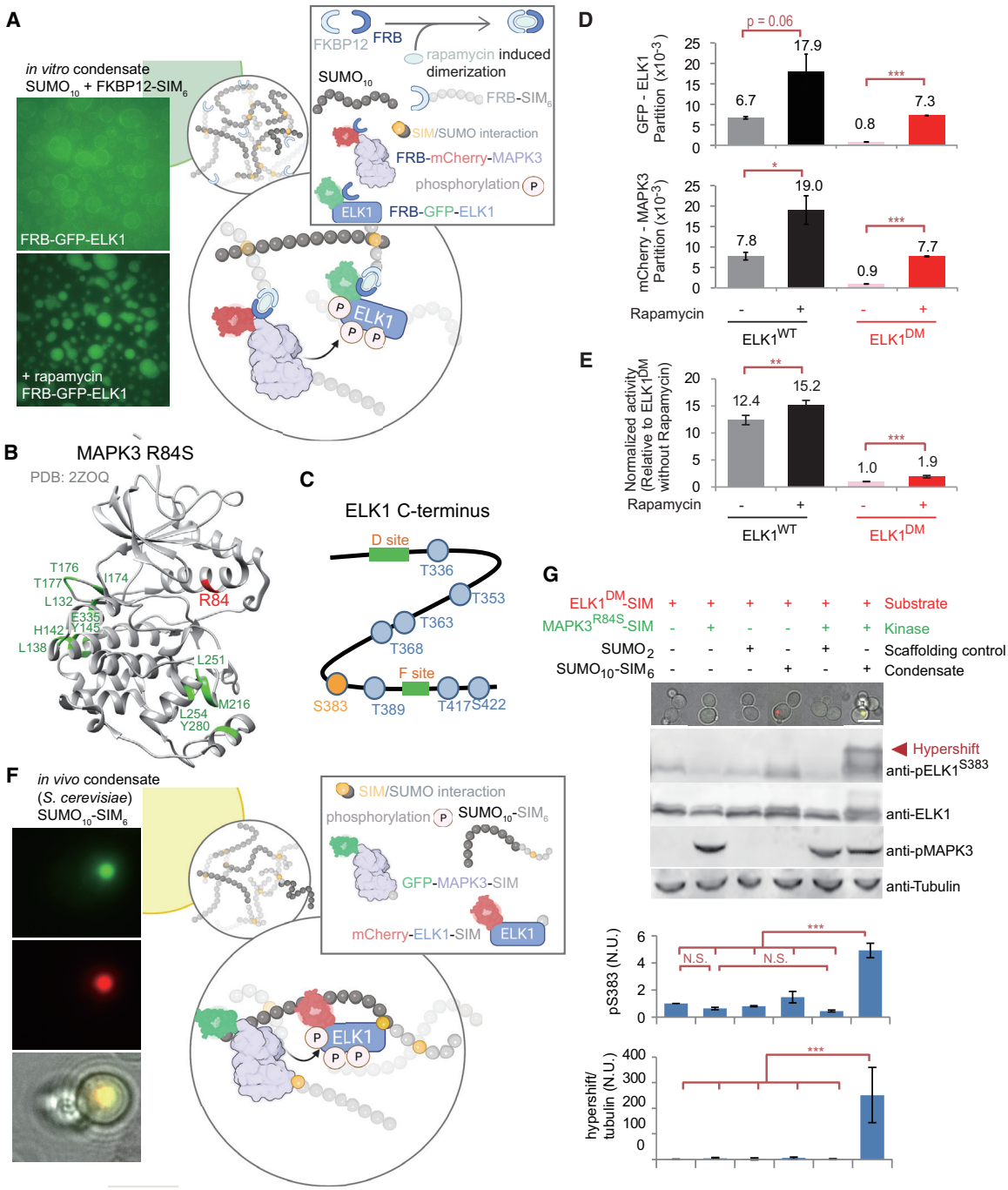

Figure 1. Recruitment into synthetic condensates increases phosphorylation rates

(A) Schematic of chemical dimerization approach. Mixture of $SUMO_{10}$ and SIM_6 leads to condensate formation. Rapamycin induces recruitment of MAPK3 (kinase) and ELK1 (substrate) into condensates.

(B) Structure MAPK3: R84 constitutive activation mutation, red; docking sites, green.

(C) Structure of the ELK1 C terminus. Blue circles are known phosphorylation sites targeted by MAPK3; phosphoepitope at S383, orange; docking motifs, green.

(D) ELK1 can be recruited to condensates. Total fraction of client that partitions into $SUMO_{10}$ + SIM_6 condensates ± rapamycin. n = 2.

(E) Recruitment to condensates increases phosphorylation *in vitro*. The C termini of ELK1 ($ELK1^{WT}$) or an ELK1 docking motif mutant ($ELK1^{DM}$) were used as substrates. n = 3.

(F) Schematic showing the approach to recruit clients into condensates in *S. cerevisiae*. $SUMO_{10}$-SIM_6 formed condensates. MAPK3 and ELK1 (clients) were tagged with SIM for recruitment into condensates.

(legend continued on next page)

separation, it follows that condensates should be capable of sensing crowding and transducing this information to chemical signals such as protein phosphorylation. However, there is little direct evidence of this biophysical sensing phenomenon.

Protein kinases regulate most aspects of eukaryotic cell biology. Kinase activity is strictly regulated, and kinases must discriminate between numerous proteins to find appropriate substrates. Defects in kinase activity regulation or loss of specificity can lead to human diseases such as cancer (Cicenas et al., 2018). Kinases exploit multiple mechanisms to achieve specificity, including subcellular localization, docking motif interactions, and recognition of consensus phosphorylation sites (Alexander et al., 2011; Howard et al., 2014; Mok et al., 2010; Reményi et al., 2006). For example, mitogen-associated protein kinases (MAP kinases) and cyclin-dependent kinase (CDK) family kinases prefer consensus phosphorylation motifs with a proline residue C-terminal to the phospho-acceptor site (Howard et al., 2014; Mok et al., 2010). Kinases can also use docking interactions for additional selectivity (Faustova et al., 2021; Howard et al., 2014; Miller and Turk, 2018; Örd and Loog, 2019; Örd et al., 2019). Several recent studies showed that a large number of kinases reside in condensates (Wippich et al., 2013; Zhang et al., 2021a), but it remains poorly understood how kinase activity is modified by recruitment to these structures. Therefore, it is of great interest to understand how kinase reaction specificity and activity can be affected within condensates.

Here, we use synthetic biology approaches to begin to uncover principles of condensed-phase signaling. We recruited the MAP kinases, MAPK3 and Fus3, and the cyclin-dependent kinase 1 (Cdk1) into multiple types of synthetic condensates formed of multivalent "scaffolds." We found that phosphorylation was increased by client recruitment into condensates both *in vitro* and *in vivo*. Kinase specificity was expanded in condensates, indicating that condensation can facilitate the creation of new links in phosphoregulatory networks. Substrates were phosphorylated in the absence of a docking motif and on non-consensus phospho-acceptor sequences. Phosphorylation within condensates could respond to dynamic changes in kinase activity within minutes. Systematic variation of scaffold and client properties revealed that beyond increasing client concentration (mass action), the availability of excess client-binding sites within the condensates and the flexibility of scaffolds strongly impacted reaction acceleration in condensates. We also found that phosphorylation within condensates can respond to molecular crowding, thus creating a biophysical sensor. Finally, we found that phosphorylation of the microtubule-binding protein, Tau, by cyclin-dependent kinase 2 (Cdk2) was accelerated in the condensed phase at sites associated with Alzheimer's disease, thus relating our insights from synthetic biology to possible new mechanisms for neurodegenerative disease.

RESULTS

Recruitment to synthetic condensates increases phosphorylation *in vitro*

Initially, we recruited a kinase and substrate to a synthetic condensate *in vitro*. The synthetic condensate was based on multivalent interactions between a tandem repeat of ten small ubiquitin-like modifier (SUMO) domains ($SUMO_{10}$) and a second polypeptide with six repeats of a SUMO Interacting Motif (SIM_6) (Figure 1A). $SUMO_{10}$ and SIM_6 readily undergo LLPS when mixed (Banani et al., 2016). Throughout this paper, we refer to proteins that form condensates as "scaffolds," proteins that are recruited to synthetic condensates as "clients."

The first clients we tested were the human Mitogen-Activated Protein kinase, MAPK3 (also called ERK1), and a C-terminal fragment of one of its substrates, ELK1. We took advantage of a constitutively active R84S mutant of MAPK3 (Figure 1B; Levin-Salomon et al., 2008) to simplify the system. The ELK1 C terminus contains multiple MAPK3 consensus phosphorylation motifs (Mylona et al., 2016) and two docking motifs (D site and F site) that bind to the surface of MAPK3. We tested the wild-type (WT) ELK1 C terminus (Figure 1C; residues 206–428, hereafter referred to as ELK1) and a version in which these two docking motifs were mutated (hereafter referred to as $ELK1^{DM}$; Figure S1A). To enable rapid recruitment of clients into condensates, we fused an FKBP12 domain to the N terminus of SIM_6 and an FRB domain and fluorescent protein (green fluorescent protein [GFP], or mCherry, for visualization) to the N terminus of each client. Dimerization of FKBP12 and FRB can be chemically induced by rapamycin. Initially, there was low binding of clients to the surface of condensates, but addition of rapamycin recruited FRB-GFP-ELK1 and FRB-mCherry-MAPK3 into the condensates (Figures 1A, 1D, and S1B).

Upon ELK1 and MAPK3 recruitment into condensates, phosphorylation of $ELK1^{WT}$ increased by 22% compared with control (Figure 1E). The $ELK1^{DM}$ mutant had lower baseline phosphorylation, as expected, but the relative increase rate upon recruitment into condensates nearly doubled (Figures 1E and S1C). Together, these results indicate that recruitment of MAPK3 kinase and the ELK1 substrate into a condensed phase accelerates phosphorylation, especially for substrates that lack docking motifs. The reaction acceleration in this experiment appears relatively small (22% for $ELK1^{WT}$, 91% for $ELK1^{DM}$); however, the condensate phase only constituted a tiny fraction of the total reaction volume (less than 3%). Therefore, as previously reported, for similar experiments (Peeples and Rosen, 2021), we

(G) Recruitment to condensates increased phosphorylation levels *in vivo*. Top: micrographs *S. cerevisiae* cells with various combinations of $MAPK3^{DM}$ (green), ELK1 (red), and scaffold controls or $SUMO_{10}$-SIM_6 condensates (no fluorescent tag). Scale bars, 5 μm. Bottom: representative western blots for ELK1-S383 phosphoepitope; total ELK1; activation-loop phosphates on the MAPK3 kinase (pT202/pY204), and tubulin loading control. Red arrowheads indicate hypershifted bands. Quantification of ELK1 S383 phosphorylation (pS383) and the hyperphosphorylation (hypershift/tubulin) are shown in bottom graphs. For S383 phosphorylation, band intensities of total phosphorylated ELK1 were normalized to total ELK1 levels, and this value was further normalized to the phosphorylation level of ELK1 in the control strain (leftmost). For hyperphosphorylation (hypershift/tubulin) quantification, the intensity signal of hypershifted band (detected by anti-p-ELK1-S383) was normalized to tubulin levels in the bottom graph, and the values were further normalized to the control strain. Error bars indicate ± SD (n = 3). Statistical comparisons are by Tukey-Kramer test: *p < 0.05, **p < 0.01, ***p < 0.001, N.S., not significant.

believe the actual acceleration in condensates is far greater than apparent in the bulk reaction.

Recruitment to synthetic condensates increases phosphorylation *in vivo*

We next used the budding yeast *Saccharomyces cerevisiae* as a model system to see if synthetic condensates could potentiate phosphorylation *in vivo*. We expressed a single polypeptide consisting of $SUMO_{10}$ fused to SIM_6 ($SUMO_{10}$-SIM_6) (Banani et al., 2016). This approach ensures that there are excess SUMO domains available as client-binding sites within the condensate. Rapamycin changes the biophysical properties of *S. cerevisiae* (Delarue et al., 2018); therefore, we did not use the FKBP12/FRB system to recruit clients. Instead, we recruited the constitutively active $MAPK3^{R84S}$ kinase (henceforth simply referred to as MAPK3) and its substrate ELK1 by fusion of a single SIM motif to their C termini (Figure 1F). We expressed combinations of SIM-tagged $ELK1^{WT}$ or $ELK1^{DM}$ (henceforth $ELK1^{WT}$-SIM or $ELK1^{DM}$-SIM) with $SUMO_{10}$-SIM_6 in *S. cerevisiae* and analyzed phosphorylation levels by western blotting using an ELK1 Serine-383-phospho-specific antibody. We observed basal phosphorylation of ELK1-SIM without MAPK3-SIM expression, indicating that yeast kinases can phosphorylate ELK1-SIM at low levels. Co-expression of MAPK3-SIM slightly increased $ELK1^{WT}$-SIM phosphorylation (Figure S1D) but did not increase $ELK1^{DM}$-SIM phosphorylation levels in the absence of the $SUMO_{10}$-SIM_6 condensate (Figure 1G). However, $ELK1^{WT}$-SIM and $ELK1^{DM}$-SIM phosphorylation at S383 was substantially increased when co-recruited with MAPK3-SIM into condensates (3.8-fold and 4.9-fold, respectively, $p < 0.001$; Figure 1G, top graph, Figure S1D). Consistent with *in vitro* experiments, $ELK1^{DM}$-SIM showed a greater relative increase in phosphorylation upon condensate recruitment. To control for scaffolding effects (i.e., the simultaneous binding of MAPK3-SIM and ELK1-SIM to adjacent SUMO domains in the dispersed solute phase), we also used a SUMO dimer ($SUMO_2$) that did not form condensates. $SUMO_2$ expression did not significantly increase $ELK1^{WT}$-SIM or $ELK1^{DM}$-SIM phosphorylation, indicating that recruitment to a condensed phase was required for increased phosphorylation. Taken together, and combined with the *in vitro* results above, these experiments indicate that recruitment to condensates increases phosphorylation rates *in vivo*.

Interestingly, we observed an increase in ELK1-SIM phosphorylation in the presence of $SUMO_{10}$-SIM_6 even without MAPK3-SIM expression (Figure 1G), suggesting the possibility that endogenous yeast kinases may be recruited into these condensates. We searched for SIM motifs in yeast CMGC family members, which are primarily proline-directed serine/threonine kinases. Surprisingly, most of these kinases harbor putative SIM motif (Table S1; Beauclair et al., 2015). We focused on yeast MAPK family members and a CDK family member Pho85. We found that deletion of the MAP kinases *FUS3 or KSS1*, and the CDK *PHO85* partly reduced phosphorylation. A *fus3Δ*, *kss1Δ*, and *pho85Δ* triple knockout mutant completely lost the increase in ELK1-SIM phosphorylation in the presence of $SUMO_{10}$-SIM_6 condensates (Figure S1E). These results suggest that *Fus3p*, *Kss1p*, and *Pho85p* acquire the ability to phosphorylate ELK1-SIM upon recruitment to $SUMO_{10}$-SIM_6 condensates.

Recruitment to synthetic condensates leads to novel multi-site phosphorylation *in vivo*

In addition to increased intensity of phospho-ELK1 bands, we noticed prominent slower migrating species when clients were recruited to condensates. ELK1 is known to be phosphorylated at multiple sites by MAPK3. Therefore, we hypothesized that the slowly migrating bands on the western blot were due to multi-site phosphorylation. Lambda phosphatase treatment resulted in almost complete loss of the hypershifted bands, whereas phosphatase inhibitor addition maintained the hypershifted band, confirming that phosphorylation caused the slow migration pattern (Figure S1F). ELK1 contains eleven serines or threonines immediately followed by proline, corresponding to consensus MAPK3 phosphorylation sites (Cruzalegui et al., 1999). Substitution all of these serines/threonines (Figure S1G) with alanine (ELK1-11A mutant) led to the loss of almost all hypershifted bands (Figure S1H). Quantification of slow-migrating bands indicated a 220-fold increase in hyperphosphorylation when $ELK1^{DM}$-SIM was recruited to condensates (Figure 1G, bottom graph, $p < 0.001$) and a 380-fold increase in the hypershifted band for $ELK1^{WT}$-SIM (Figure S1D, bottom graph, $p < 0.001$). ELK1 was previously shown to be phosphorylated at different sites with different kinetics (Mylona et al., 2016). Serine 383 (Serine 384 in mouse Elk-1) is the most rapidly phosphorylated residue, perhaps leading to partial reaction saturation even when $ELK1^{WT}$-SIM and MAPK3-SIM are co-expressed without $SUMO_{10}$-SIM_6 and explaining the modest increase in phosphorylation of this residue when $ELK1^{WT}$-SIM is recruited to condensates. On the other hand, condensate recruitment seems to have a far more pronounced effect on the phosphorylation of residues that are normally inefficiently phosphorylated (Mylona et al., 2016). Therefore, we focused on these hypershifted bands for our study.

Condensates facilitate dynamic new links between kinases and substrates

We hypothesized that recruitment into condensates might create a permissive environment for phosphorylation, potentially expanding kinase specificity. To test this idea, we investigated whether other kinases that did not evolve with ELK1 as a substrate could phosphorylate ELK1-SIM when recruited to $SUMO_{10}$-SIM_6 condensates. We first selected Fus3, the yeast kinase most closely evolutionarily related to MAPK3 (Figure 2A). The addition of the α-factor mating peptide activates a signaling pathway that greatly increases Fus3 kinase activity (Elion, 2000). We first added a single SIM tag to the endogenous *FUS3* gene and found that α-factor caused a slight increase in ELK1-SIM phosphorylation as predicted (Figures S2A–S2D). However, recruitment to condensates was weak. We therefore tagged the *FUS3* gene with a double SIM tag (gene product hereafter, Fus3-2xSIM) to more strongly recruit it into $SUMO_{10}$-SIM_6 condensates (Figures 2B and S2A–S2D). Western blot results showed that ELK1-SIM phosphorylation on S383 increased ~7-fold when Fus3-2xSIM was co-localized in $SUMO_{10}$-SIM_6 condensates even prior to addition of α-factor (Figure 2B, top graph, third lane, $p < 0.01$). This result indicates that basal activity of Fus3-2xSIM can drive significant phosphorylation of a novel substrate in condensates. However, the level of ELK1-SIM S383 phosphorylation was further increased to ~15-fold above background upon activation of

CellPress
OPEN ACCESS

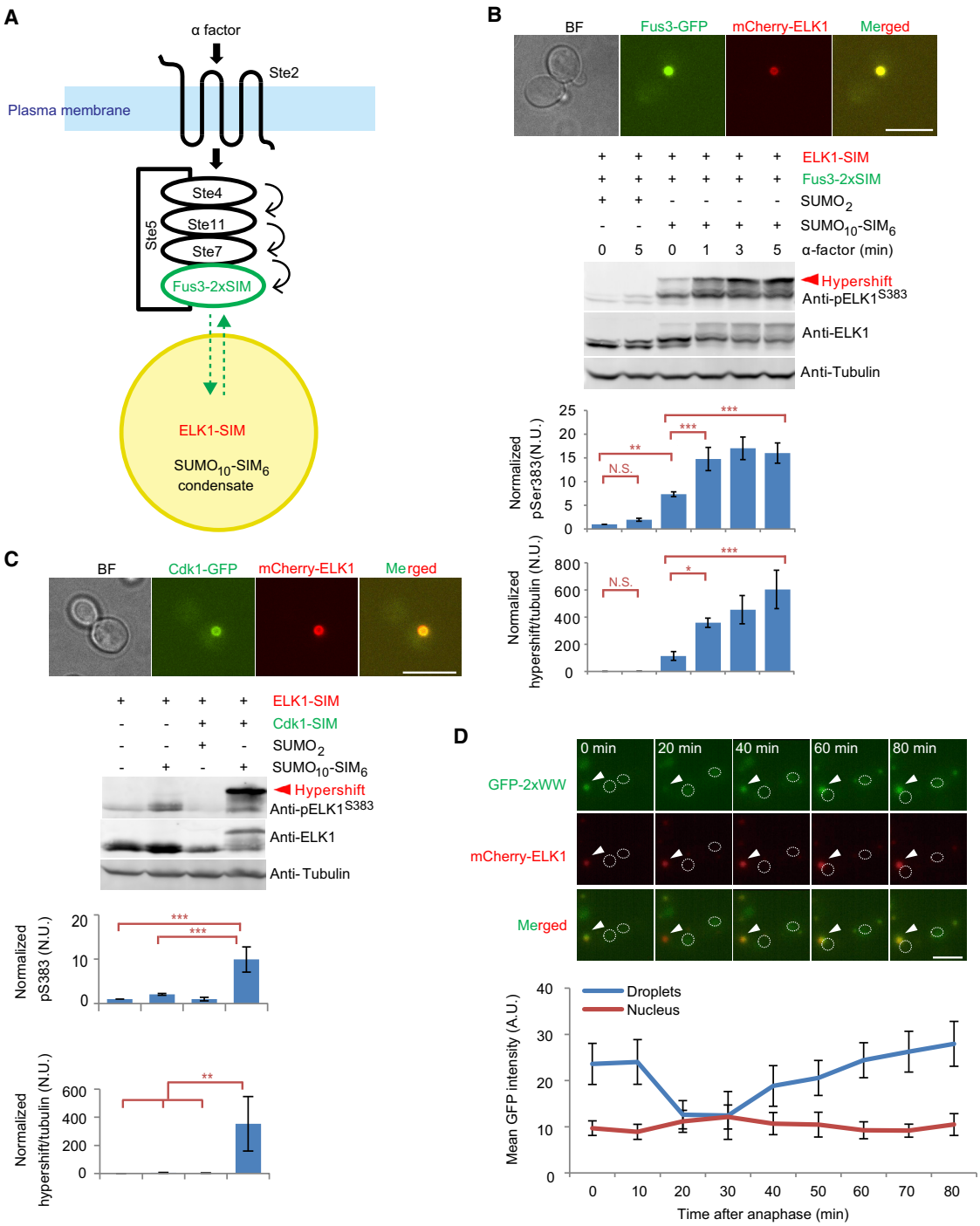

Figure 2. Condensates facilitate new links between kinases and substrates

(A) Schematic of ELK1 phosphorylation by Fus3 in condensates.

(B) Phosphorylation of ELK1 by Fus3 is accelerated in the condensed phase. Cells were treated with 2 μM α-factor to activate Fus3. Top: representative micrographs; bottom: representative western blots. Antibodies, quantification, and normalization of ELK1 S383 phosphorylation (pS383) and hyperphosphorylation (hypershift/tubulin) are as in Figure 1. n = 3.

(C) Phosphorylation of ELK1 by Cdk1 is accelerated in the condensed phase. Micrographs, western blots, and quantification are as in (B).

(D) The NLS-GFP-2xWW reporter dynamically changes localization during mitosis. Average projections of representative micrographs (GFP-2xWW, green; mCherry-ELK1, red) are shown. White dotted line indicates the position of the nucleus as detected by a 2xNLS-BFP reporter. White arrowheads indicate condensates. Mean intensities of GFP in condensates and in the nucleus are plotted. n = 10. Scale bars, 5 μm. Error bars indicate ± SD. Statistical comparisons are by Tukey-Kramer test, *p < 0.05, **p < 0.01, ***p < 0.001, N.S., not significant.

Fus3 by addition of α-factor for 5 min (Figure 2B, top graph, $p < 0.001$). Furthermore, the hypershifted bands were even more strongly induced by α-factor (~600-fold, $p < 0.001$, Figure 2B, bottom graph). Expression of ELK1-SIM and Fus3-2xSIM together with a simple $SUMO_2$ scaffold did not result in significantly increased phosphorylation of ELK1-SIM, regardless of α-factor addition. These results indicate that a novel kinase-substrate connection can be induced by recruitment to a condensate and that information from upstream signaling can still be received within this condensed phase within 1 min.

In processive phosphorylation, multiple phosphorylation events occur in a single kinase/substrate interaction (where a scaffold can also be considered part of the interaction), whereas in distributive phosphorylate, phosphates are added to the substrate over the course of several interactions. The prediction of processive phosphorylation is that, in a time-course, the uppermost hyper-phosphorylated bands should appear immediately and then get more abundant with time (Kõivomägi et al., 2011). The prediction of distributive phosphorylation is that intermediate bands should appear first and then higher and higher bands appear over time in a ''ladder-like'' fashion. We found that Fus3 activation led to immediate appearance of a completely hypershifted band (after 1 min) that proceeded to gets darker. There was no significant accumulation of intermediate phosphorylated forms after α-factor addition at 1 or 3 min, indicating that ELK1-SIM phosphorylation in $SUMO_{10}$-SIM_6 condensates was processive (Figures 2B, S2D, and S2E).

Next, we tested if a more evolutionarily distant kinase could phosphorylate ELK1-SIM within condensates. We chose the CDK Cdk1 (encoded by the *CDC28* gene in *S. cerevisiae*). Cdk1 is still proline directed but is structurally and functionally distinct from MAP kinases and recognizes different docking motifs (Howard et al., 2014; Mok et al., 2010; Schulman et al., 1998). We tagged the endogenous Cdk1 with a single SIM peptide (Cdk1-SIM) and observed robust recruitment into $SUMO_{10}$-SIM_6 condensates (Figure 2C, top). Co-recruitment of ELK1-SIM and Cdk1-SIM led to high levels of phosphorylation of ELK1-SIM, both in terms of S383 phosphorylation (~10-fold increase, $p < 0.001$; Figure 2C, top graph) and levels of hypershifted bands (~300-fold increase, $p < 0.01$; Figure 2C, bottom graph). Expression of ELK1-SIM and Cdk1-SIM together with a simple $SUMO_2$ scaffold did not increase ELK1-SIM phosphorylation over background levels.

To gain insight into the kinetics of this reaction, we engineered an induced dimerization system based on plant gibberellic acid (GA) signaling (Miyamoto et al., 2012) to recruit clients into $SUMO_{10}$-SIM_6 condensates in *S. cerevisiae* cells (Figure S2F). GA addition induced mCherry-ELK1 recruitment into $SUMO_{10}$-SIM_6 condensates in which Cdk1-GFP-SIM was localized (Figure S2G) and increased ELK1 phosphorylation (Figure S2H). The GA-induced reaction was slower than Fus3, and hypershifted bands were only significantly induced after 30 min. Nevertheless, as for the Fus3 system, there was no ladder-like accumulation of intermediate phosphorylated forms detected after GA addition but rather the hypershifted band appeared immediately and grew more intense with time, consistent with a processive multi-site phosphorylation reaction.

Cdk1 regulates the cell division cycle (Malumbres, 2014). Cdk1 is most active during mitosis and is inactivated during mitotic exit by degradation of cyclins (Enserink and Kolodner, 2010). In addition, the CDC14 phosphatase that counteracts Cdk1 is specifically activated during mitotic exit (Stegmeier and Amon, 2004). Therefore, substrates of Cdk1 are dynamically phosphorylated and dephosphorylated as the cell cycle progresses. To further investigate the ability of synthetic condensates to create novel kinase connections while allowing dynamic regulation, we built a reporter system to visualize phosphorylation of ELK1-SIM by Cdk1 in real time in single cells.

To create a live-cell reporter of ELK1-SIM phosphorylation, we fused two WW domains from the *Homo sapiens* PIN1 protein to GFP (GFP-2xWW). The WW domain specifically interacts with phosphorylated serine-proline motifs (Verdecia et al., 2000). We hypothesized that ELK1-SIM phosphorylation within synthetic condensates would create WW-domain binding sites leading to reporter recruitment to the condensates (Figure S3A). Indeed, we found that co-expression of MAPK3-SIM and ELK1-SIM led to the translocation of the GFP-2xWW reporter into $SUMO_{10}$-SIM_6 condensates (Figure S3B, top). As a control, we expressed a catalytically dead MAPK3 mutant (MAPK3-K71R) and found very little recruitment of the reporter into $SUMO_{10}$-SIM_6 (Figures S3B, bottom and S3C). These results suggested that the reporter was recruited to synthetic condensates in a phosphorylation-dependent manner.

We next modified the reporter to attempt to reveal dynamic phosphorylation of ELK1-SIM by Cdk1. We added an SV40 nuclear localization signal (NLS) to the N terminus (NLS-2xWW-GFP), such that when the reporter and ELK1-SIM were co-expressed with $SUMO_{10}$-SIM_6 but Cdk1 was not tagged with SIM, most of the reporter was nuclear, and very little was recruited to condensates (Figure S3D). However, when Cdk1 was tagged with SIM, a significant number of cells had strong reporter recruitment to condensates (Figure S3E). We next examined the dynamics of reporter recruitment to condensates during the cell cycle by time-lapse imaging (Figure 2D). Reporter intensity within condensates was highest immediately prior to anaphase, the point at which Cdk1 activity is highest (Enserink and Kolodner, 2010). Approximately 20–30 min after anaphase, reporter signal was reduced within condensates and relocalized to the nucleus (Figure 2D; Video S1). This corresponds to the timing of mitotic exit, when Cdk1 is rapidly inactivated by cyclin degradation and expression of the Cdk1 inhibitor Sic1 (Enserink and Kolodner, 2010). In addition, the phosphatase Cdc14 is activated at this time, leading to rapid dephosphorylation of phosphorylated S-P and T-P motifs (Visintin et al., 1998). Subsequently, after 10–20 min, a time when Cdk1 activity is rising, the reporter intensity in condensates also started to increase (Figures 2D and S3F). Collectively, these results suggest that recruitment of Cdk1-SIM to a synthetic condensate can create a new kinase-substrate connection, with dynamics that closely follow the cell cycle.

We next wondered if recruitment to condensates would relax the primary specificity of kinases, enabling phosphorylation of a broader range of peptides. First, we used a short peptide flanking serine383 in ELK1 as a substrate (residues 370–394, referred to as min383 hereafter) to completely remove the D box and F box docking sites. We fused this peptide and MAPK3 to a 5xSIM tag

to obtain strong enrichment within condensates (Figure S4A). This resulted in strong phosphorylation (Figures S4B–S4D), suggesting that docking motifs are not required for MAPK3 phosphorylation within condensates. Interestingly, condensates were also formed when 5xSIM-tagged-clients were co-expressed with $SUMO_2$ (Figure S4C), resulting in increased min383 phosphorylation, and these condensates also drove phosphorylation.

We noticed that there were multiple hypershifted bands, accounting for almost 50% of total min383 (Figure S4D) within $SUMO_{10}$-SIM_6 condensates. These bands disappeared after lambda phosphatase treatment (Figure S4E), suggesting that phosphorylation caused this slow migration pattern. There is only one additional MAPK3 consensus phospho-acceptor site (S/T-P motif, serine389) in min383 (Figure S4F); therefore, we hypothesized that other non-consensus sites could also be phosphorylated. We generated point mutant and truncation constructs to identify the residues responsible for the hypershifted bands (Figure S4G). Deletion of four consecutive serines at the N terminus almost completely abolished slowly migrating bands (Figure S4H), suggesting that these four non-consensus serines were phosphorylated by MAPK3. Thus, MAPK3 can phosphorylate non-consensus sequences when within condensates.

We next investigated the ability of Cdk1 to phosphorylate non-canonical substrates within condensates. Cdk1 is also a proline-directed kinase; hence, we generated a synthetic construct that fused short peptides from the human P53 and RPS6 proteins (Figures S4I and S4J, referred to PR hereafter), none of which contain any known primary specificity determinants for Cdk1 (Mok et al., 2010). Western blot results showed that peptides from serine9 and serine37 in P53 were more highly phosphorylated by Cdk1 when recruited to condensates (Figures S4K–S4M). Serine235/236 in RPS6 was also phosphorylated by Cdk1 in condensates. Note, in some cases, we believe that recruitment into synthetic condensates stabilizes clients, for example, leading to the high anti-HA signal in lanes 3 and 5 of Figure S4L. To control for these effects, we normalized the phosphorylation signal to the total anti-HA signal. Collectively, these results show that the primary specificity of MAPK3 and Cdk1 is relaxed when recruited to condensates.

Multiple factors contribute to hyperphosphorylation in condensates

A major advantage of synthetic biology is the possibility of systematically varying parameters in an attempt to understand general principles. Therefore, we varied the properties of both the condensate scaffold proteins and the clients to investigate which factors impact phosphorylation of ELK1 by MAPK3 within condensates (Figures 3A and 3B).

First, we characterized the effect of client-binding affinity on phosphorylation in condensates. A single substitution in the SIM peptide (substitution of Isoleucine 9 with proline, referred to as SIM^{I9P} hereafter) decreases the affinity of the interaction between SIM and SUMO (Namanja et al., 2012). We tagged the ELK1 substrate with either WT SIM (SIM^{WT}) or SIM^{I9P}, whereas the MAPK3 kinase was always tagged with SIM^{WT}. The concentration of ELK1-SIM^{I9P}-tagged substrate was dramatically reduced in $SUMO_{10}$-SIM_6 condensates (Figures 3B and S5A). Western blotting showed that hyperphosphorylation of ELK1-SIM^{I9P} in condensates was reduced by almost 80% compared with ELK1-SIM^{WT} (Figures 3B and S5B). We hypothesized that the reduced substrate concentration led to the decreased hyperphosphorylation. To test this idea, we used a stronger promoter to increase the expression level of ELK1-SIM^{I9P} and restore the concentration of ELK1-SIM^{I9P} in condensates. Indeed, this higher substrate concentration within condensates partly restored ELK1-SIM^{I9P} hyperphosphorylation. However, when ELK1-SIM^{I9P} was present at equivalent concentration to ELK1-SIM^{WT}, there was still a 2-fold decrease in hyperphosphorylation. One possible explanation is that the binding kinetics of client SUMO domains within the condensate plays an important role. The unbinding rate (k_{off}) of ELK1-SIM^{I9P} is likely to be higher than ELK1-SIM^{WT}. Therefore, we speculated that lower k_{off} might favor hyperphosphorylation. Increasing valency can also reduce k_{off} (Tang et al., 2012). We therefore fused both kinase and substrate with two SIM-tags (2xSIM) to investigate the effect of client valence on hyperphosphorylation in condensates. The 2xSIM-tag led to a slightly higher (~20%) MAPK3 concentration in condensates compared the single SIM tag but had no effect on ELK1 concentrations (Figures 3B and S5A). However, western blotting showed that ELK1 hyperphosphorylation almost doubled (Figures 3B and S5B). We compared the 2xSIM-tagged substrate phosphorylation to strongly overexpressed kinase and substrate with a single SIM tag. This strong overexpression led to higher client concentrations in condensates and slightly higher ELK1 hyperphosphorylation. Together, these results suggest that both client concentration and binding kinetics modulate the degree of hyperphosphorylation within condensates.

The number of excess client-binding sites strongly impacts hyperphosphorylation

We next investigated how the properties of synthetic condensates could impact hyperphosphorylation. The presence of excess SUMO domains within the $SUMO_{10}$-SIM_6 condensates has been shown to be important for client recruitment (Banani et al., 2016). We therefore tested the effect of reducing the number of free SUMO domains by comparing $SUMO_7$-SIM_6 to $SUMO_{10}$-SIM_6 condensates. We screened for cells with client recruitment into $SUMO_7$-SIM_6 condensates that were similar to $SUMO_{10}$-SIM_6 condensates (Figures 3B and S5A). However, ELK1-SIM hyperphosphorylation within $SUMO_7$-SIM_6 condensates was reduced by almost 90% (Figures 3B and S5B). Next, we asked whether we could restore hyperphosphorylation in $SUMO_7$-SIM_6 condensates by increasing client concentration in condensates. Interestingly, hyperphosphorylation was still ~3-fold lower in strains expressing $SUMO_7$-SIM_6 condensates when the expression of both clients was increased such that client concentration in $SUMO_7$-SIM_6 was higher than in $SUMO_{10}$-SIM_6 condensates. This suggests that the excess SUMO domains in condensates potentiates hyperphosphorylation through a mechanism beyond simple mass action.

Condensate scaffold flexibility is crucial for hyperphosphorylation

The SUMO-SIM condensates are based on highly flexible polymers that can assemble in many conformations. We wondered whether this flexibility, which appears to be a frequent feature

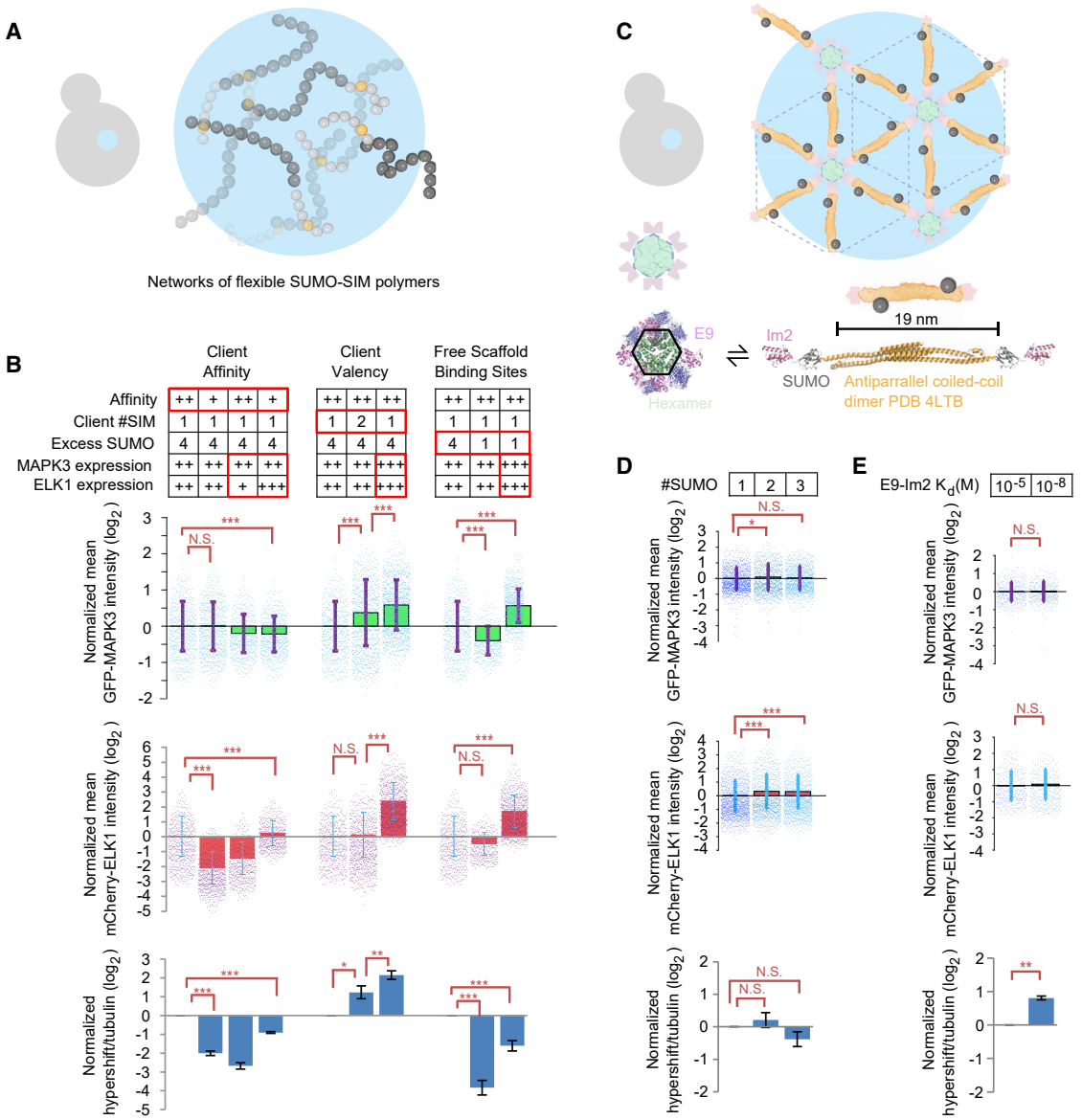

Figure 3. Multiple factors contribute to hyperphosphorylation in condensates

(A) Schematic of $SUMO_n$-SIM_n condensates in *S. cerevisiae* cells.

(B) Affinity: interaction strength altered using SIM variants with low K_d (higher affinity, ++) or high K_d (lower affinity, +). Client # SIM: one or two SIMs on clients. Excess SUMO: $SUMO_{10}$-SIM_6 has 4 excess SUMO per scaffold, and $SUMO_7$-SIM_6 has 1 excess SUMO per scaffold. MAPK3 expression; ELK1 expression: different promoters for high (+++), medium (++), or low expression levels (+). Relative concentrations of clients within condensates are shown in red and green bar graphs, where each point is the quantification of one condensate. Bottom: blue bar graph shows the quantification of hyperphosphorylation levels from western blots. Values normalized to the median of the leftmost strain.

(C) Schematic of a synthetic two-component condensate. One component consists of a homodimerizing scaffold fused to one or more SUMO to recruit SIM-tagged client proteins and an Im2 domain. The other component consists of a homohexamerizing scaffold fused to BFP and an E9 domain. The Im2 and E9 domains interact with one another.

(D) One, two, or three SUMO domains were inserted into the dimer-forming component. Client concentrations within condensates were estimated as above and normalized to leftmost strain. Bottom: blue bar graph shows the quantification of hyperphosphorylation levels from western blots.

(E) Characterization of the effect of the affinity of the Im2/E9 interaction. Client concentrations and hyperphosphorylation quantified as above. n = 3 for all experiments. Error bars indicate ± SD; statistics in 3B and 3D by Tukey-Kramer test, statistics in 3E by Student's t test, *p < 0.05, **p < 0.01, ***p < 0.001; N.S., not significant.

of biological condensates (Alberti and Hyman, 2021; Hastings and Boeynaems, 2021; Li et al., 2012), was important for the potentiation of phosphorylation. We took advantage of a recently described design strategy (Heidenreich et al., 2020) based on a well-structured synthetic two-component system (Figure 3C). One component consists of a homo-hexamer. The other component is a homo-dimer consisting of a long (18 nm), rigid, antiparallel coiled-coil domain from the TRIM25 protein. Interaction between these two components was engineered using a well-characterized heterodimeric interaction between the colicin E9 (henceforth simply E9) and the immunity protein, Im2 (Li et al., 1998). We fused E9 to the C terminus of the hexamer and Im2 to the N terminus of the dimer. An important design feature is that the dimer is too long to bind twice to the same hexamer, thereby making lattice assembly within the condensate more predictable. We additionally fused a SUMO domain to the N terminus of the dimer. The topology of the dimer is such that the N termini are distant from one another at the opposite ends of each dimer. This synthetic condensate is predicted to assemble in a limited set of local geometries from rigid components that hold individual SUMO domains relatively distant from one another.

When expressed in yeast, the synthetic two-component-system-formed condensates that recruited ELK1-SIM and MAPK3-SIM clients (Figure S5C). We screened for yeast strains that recruited clients to these two-component-system-formed condensates at similar levels as SUMO-SIM condensates (Figure S5D). We found that recruitment of ELK1-SIM and MAPK3-SIM to SUMO domains within this ordered condensate led to a slight increase in total phosphorylation levels at S383 (~50%) and a similar increase hyperphosphorylation (~35-fold) (Figure S5E) to $SUMO_7$-SIM_6, but ~10-fold less than in $SUMO_{10}$-SIM_6 condensates. Thus, scaffold flexibility appears to be important for efficient phosphorylation within condensates.

Three adjacent client-binding sites are insufficient for efficient phosphorylation in rigid condensates

A major feature of the two-component system is that the SUMO binding sites are held at a slight distance from one another within a relatively rigid network. This is distinct from the SUMO-SIM condensates, where multiple adjacent SUMO domains can be available for client binding in a single polymer, and the scaffold flexibility potentially allows for even more extensive clusters of SUMOs to occur. Indeed, the fact that the availability of excess SUMO domains has the largest effect on the efficiency of hyperphosphorylation (Figure 3B, right) suggests that the availability of local clusters of client-binding sites is crucial for efficient condensed-phase signaling. Control experiments demonstrate that dimers of SUMO in solution are insufficient for reaction acceleration (Figures 1G, 2B, 2C, and S1D) Hence, we investigated if adding pairs or triads of SUMO domains to the dimer in the two-component condensate could better drive condensed-phase phosphorylation. We screened for cells with similar client concentrations within condensates to simplify interpretation (Figure S5E). We fused the dimer component to 2xSUMO and 3xSUMO. Again, each 2xSUMO or 3xSUMO is held 18 nm distant from its partner by the rigid antiparallel coiled-coil of the dimer and can be within 9–12 nm of a set of SUMO sites on an adjacent dimer head (Figure 3C). We found no increase in S383 phosphorylation or hyperphosphorylation of ELK1-SIM with 2xSUMO or 3xSUMO relative to 1xSUMO within these rigid condensates (Figures 3D and S5F). These results suggest that even with a huge concentration of 3xSUMO domains, the inability of the rigid scaffold network to generate larger SUMO clusters may limit the efficiency of this condensate as a catalyst of hyperphosphorylation. Therefore, local pockets of high client-binding site concentration (>3 SUMO sites), and perhaps scaffold polymer dynamics *per se*, may play an important role in condensed-phase signaling.

Scaffold material properties do not greatly affect phosphorylation within ordered condensates

A useful feature of the two-component system is the availability of Im2 variants with varying affinity to E9 (Heidenreich et al., 2020; Li et al., 1998). We engineered two interaction strengths between the two scaffold components, either in the micromolar ($K_d \sim 3 \times 10^{-5}$ M) or nanomolar ($K_d \sim 1.2 \times 10^{-8}$ M) range. This approach was previously shown to create liquid- and solid-like condensates, respectively (Heidenreich et al., 2020). We screened for yeast strains expressing each of these variants that had similar condensate sizes and client concentrations in the condensates (Figures 3E and S5G). Western blotting showed a slight increase (~2-fold) in hyperphosphorylation in the strain expressing the high-affinity (10^{-8}M) Im2 variant over that of the lower affinity (10^{-5}M) variant (Figures 3E, VG, and S5H). This result suggests the material states and dynamics of the condensed scaffold only play a minor role in condensed-phase phosphorylation within these well-structured networks.

Synthetic condensed-phase signaling can respond to osmotic compression

Osmotic compression reduces cell size, increases macromolecular crowding, and decreases molecular diffusion. On a microscopic scale, the assembly, dynamics, and network structure of condensates could all be impacted by macromolecular crowding, as could the dynamics of client interactions and motion within the condensed phase. We speculate that client molecules exist in two states within condensates: some in the fluid phase that permeates the condensate, others bound to the condensate scaffolds. As macromolecular crowding alters the condensate network, both the motion through the fluid phase and the binding kinetics of clients could be impacted. Thus, it is possible that phosphorylation within condensates could be sensitive to changes in the biophysical properties of the cell and provide a mechanism to convert physical states such as macromolecular crowding to chemical signals. We took advantage of our synthetic condensates to test this idea and investigate factors important for this physical sensing.

We used *hog1Δ* strains that are deleted for the main osmotic stress response kinase. This mutation prevents osmoadaption and mitigates changes in signaling due to *Hog1p* activation upon osmotic stress (Hohmann, 2002). We tested condensates that varied in the two factors that we previously determined to have the greatest effect on phosphorylation efficiency: condensate network flexibility, and the availability of excess SUMO (i.e., $SUMO_{10}$-SIM_6 versus $SUMO_7$-SIM_6).

First, we tested the effect of osmotic compression of $SUMO_{10}$-SIM_6 condensates. We osmotically compressed cells with 1M

sorbitol for 1 h and quantified client recruitment, condensate size, and hyperphosphorylation of ELK1-SIM. Average condensate area decreased by around 35%, likely due to oncotic compression, and recruitment of GFP-MAPK3-SIM increased ~70% (Figures S6A and S6B), but ELK1-SIM hyperphosphorylation was only increased about 10% (Figure S6C, lanes 3 and 4). We reasoned that this could be because $SUMO_{10}$-SIM_6 condensates already give the most efficient hyperphosphorylation of any synthetic condensate; therefore, the reaction is essentially saturated and difficult to further accelerate. We therefore next tested the effect of osmotic compression of $SUMO_7$-SIM_6 condensates. The change in condensate area and client concentration was similar to that in $SUMO_{10}$-SIM_6 condensates (35% area decrease and ~70% increase in GFP-MAPK3-SIM; Figures S6A and S6B). However, the degree of ELK1-SIM hyperphosphorylation in $SUMO_7$-SIM_6 condensates was increased ~2-fold (Figure S6C, lanes 1 and 2). In conclusion, hyperphosphorylation within the efficient $SUMO_{10}$-SIM_6 condensates is relatively insensitive to osmotic compression, but hyperphosphorylation becomes sensitive to osmotic stress within the less efficient $SUMO_7$-SIM_6 condensates.

When *HOG1* is deleted, crosstalk from osmotic stress pathway to the *Fus3* kinase has been reported (O'Rourke and Herskowitz, 1998). We demonstrated above that *Fus3* can phosphorylate ELK1-SIM when recruited to condensates (Figure 2B). Therefore, it was important to rule out the possibility that osmotic stress leads to activation of *Fus3* and its recruitment to condensates. However, ELK1-SIM hyperphosphorylation increased similarly upon osmotic shock in *hog1Δ; fus3Δ* double-mutant strains and *hog1Δ* strains (Figure S6D). Therefore, *Fus3* does not appear to play a role in the change in hyperphosphorylation that we observe after osmotic compression.

In a control strain containing a soluble $SUMO_2$ scaffold control without condensates, osmotic shock led to reduced levels of mCherry-ELK1-SIM (Figure S6E). In cases with significant changes in ELK1-SIM levels, we normalized phosphoELK1-SIM levels to total ELK1-SIM levels to allow for meaningful comparisons. ELK1-SIM S383 phosphorylation was almost undetectable upon sorbitol treatment in the $SUMO_2$ scaffold control strain. Additionally, we tested a $SUMO_2$ scaffold control in which SUMO was fused the coiled-coil domain from TRIM25. The levels of ELK1-SIM S383 phosphorylation relative to total ELK1-SIM protein were decreased by almost 80% in this soluble $SUMO_2$ dimer scaffold strain (Figure S6F). This decrease may be caused by reduced molecular diffusion upon the increase in macromolecular crowding. There was less change in ELK1-SIM levels in all strains that recruited mCherry-ELK1-SIM to condensates. ELK1 is known to be regulated through proteolysis (Evans et al., 2011); therefore, we speculate that condensates can protect ELK1 from proteolysis.

The initial client concentration was higher in $SUMO_{10}$-SIM_6 condensates than in $SUMO_7$-SIM_6 condensates (Figure S6A). This led to the hypothesis that the hyperphosphorylation is almost saturated in $SUMO_{10}$-SIM_6 condensates, whereas $SUMO_7$-SIM_6 condensates remain sensitive to concentration changes. To test this idea, we used stronger promoters to increase client concentration in $SUMO_7$-SIM_6 condensates. Consistent with the hypothesis, there was no significant change in ELK1-SIM hyperphosphorylation upon osmotic compression in these strains (Figure S6C, lanes 5 and 6). Therefore, condensed-phase signaling can respond to osmotic compression when the system is appropriately tuned; hyperphosphorylation responds to osmotic compression within $SUMO_7$-SIM_6 condensates that contain a low enough client concentration that reaction rates are not saturated.

Next, we investigated the effect of osmotic compression on phosphorylation within the more rigid two-component condensates. We used the lower affinity Im2 variant that creates a more liquid-like condensate, which we reasoned would be more likely to respond to compression (Heidenreich et al., 2020). Upon osmotic compression, condensate area was only slightly decreased (~10%; Figure 4C), but the concentration of GFP-MAPK3-SIM clients increased in the condensates to a similar degree as in $SUMO_7$-SIM_6 condensates, by ~60% (Figure 4B). Strikingly, osmotic compression did not increase hyperphosphorylation in the two-component condensates but rather the degree of ELK1-SIM hyperphosphorylation was decreased by ~50% upon osmotic compression ($p < 0.05$; Figures 4D and 4E). We screened for colonies with a lower concentration of clients in two-component condensates to rule out the possibility that the phosphorylation rates were initially saturated. The degree of hyperphosphorylation in these strains was still reduced upon osmotic compression (Figures S6G and S6H). We also compared client recruitment between flexible $SUMO_7$-SIM_6 and the more rigid two-component condensates. The recruitment difference is small between the two condensates: mCherry-ELK1-SIM recruitment was similar, whereas GFP-MAPK3-SIM was recruitment to $SUMO_7$-SIM_6 condensates was ~65% that of two-component condensates (Figures S7A and S7B). Together, these results suggest that rigid condensates respond to osmotic compression in the opposite way to flexible condensates and suggest that the flexibility of SUMO-SIM condensates is important for their ability to transduce osmotic stress to changes in hyperphosphorylation.

To further investigate the hypothesis that structural rigidity explains the opposite response of the two-component condensates to osmotic compression, we modified this two-component system to connect each hexamer subunit with a flexible $SUMO_{10}$ polypeptide. In place of the Im2-E9 interaction, we simply placed a SIM peptide at the C terminus of the hexamer subunits, such that the network was crosslinked by SUMO-SIM interactions (Figure S7C). Co-expression of the hexamer-SIM with $SUMO_{10}$ led to condensate formation and client recruitment (Figure S7D). The area of these condensates area was reduced by 25% upon sorbitol treatment, significantly more than that for rigid two-component condensates ($p < 0.001$; Figures 4C and S7E). This increase in condensate compression is consistent with the idea that polymer flexibility is important for mesoscale structural changes to synthetic condensates upon changes to the physical environment. Western blotting showed that the relative amount of ELK1-SIM hyperphosphorylation in the hexamer-SIM + $SUMO_{10}$ condensate slightly increased, but not significantly (Figures 4D and 4E). Therefore, this mixed system with one structured and one flexible component shows intermediate behavior. These results further support the hypothesis that condensate

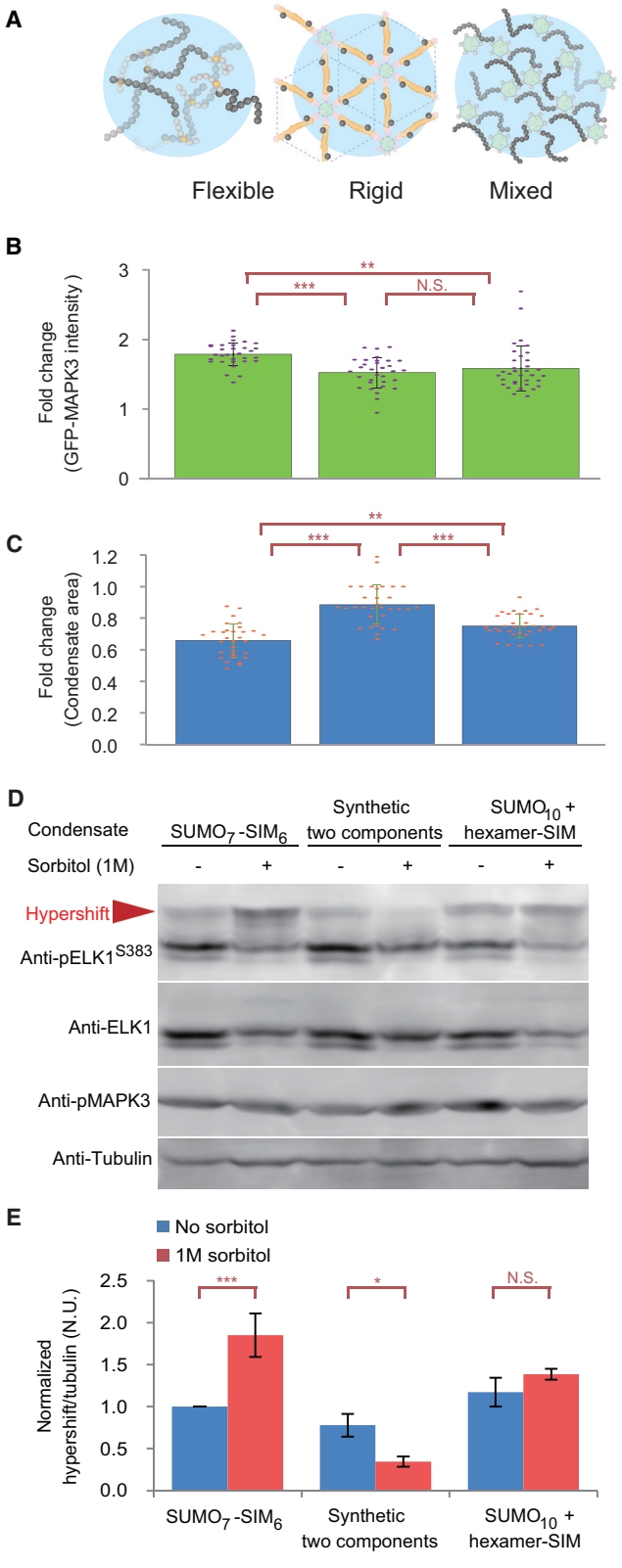

Figure 4. Synthetic condensed-phase signaling can respond to osmotic compression

(A) Schematic showing three different types of synthetic condensate: (left) rigid two-component condensate, (middle) flexible $SUMO_7$-SIM_6 condensate, and (right) mixed system.

(B) GFP intensity in condensates before and after 1 h osmotic compression with 1 M sorbitol.

(C) Condensate volumes decrease to varying degrees upon osmotic compression, depending on scaffold flexibility. Same condensates were measured before and after 1 h osmotic compression with 1 M sorbitol.

(D) Representative western blots.

(E) Osmotic compression increases hyperphosphorylation in flexible condensates and decreases hyperphosphorylation in rigid condensates. Quantification of degree of hyperphosphorylation from western blots, normalized as in previous figures. *hog1Δ* strains were used to prevent osmoadaptation. Error bars indicate ± SD (n = 3). Statistical comparisons are by Tukey-Kramer test: *p < 0.05, **p < 0.01, ***p < 0.001, N.S., not significant.

compressibility and scaffold linker flexibility are important for the response of condensed-phase phosphorylation to osmotic compression.

Synthetic condensed-phase signaling responds to changes in macromolecular crowding

We next investigated macromolecular crowding as a possible mechanism osmotic sensing by $SUMO_7$-SIM_6 condensates. We previously found that the mTORC1 pathway influenced the phase separation of $SUMO_{10}$-SIM_6 synthetic condensates through modulation of the concentration of ribosomes in the cytosol (Delarue et al., 2018). Ribosomes are the main mesoscale crowder in the cytosol. When mTORC1 is inhibited by rapamycin, the concentration of ribosomes decreases ~2-fold, and the phase separation of $SUMO_{10}$-SIM_6 is substantially reduced (Delarue et al., 2018). A similar effect is observed in the *sfp1Δ* mutant, which lacks the *Sfp1p* transcription factor that drives high levels of ribosome biogenesis downstream of active mTORC1; this mutant has low baseline crowding and therefore low $SUMO_{10}$-SIM_6 phase separation. Rapamycin has no further effect on ribosome concentration in this mutant, but crowding and condensation can be rescued by osmotic compression. We explored these conditions and mutants to test the hypothesis that condensed-phase signaling in $SUMO_7$-SIM_6 condensates respond to changes in macromolecular crowding.

We took advantage of 40-nm diameter genetically encoded multimeric nanoparticles (40nm-GEMs) to quantify macromolecular crowding (Delarue et al., 2018). We imaged cells at 100 Hz to obtain tracks of the motion of 40nm-GEMs (Figures 5A and 5B; Video S2). From the effective diffusion coefficient of 40 nm GEMs, we can infer properties of the intracellular environment, including the degree of macromolecular crowding at the length-scale of ribosomes. The Doolittle equation can be adapted to predict 40nm-GEM D_{eff} as a function of relative ribosome concentration and vice versa (Delarue et al., 2018; Doolittle, 1951). Using the same method (Figure S8A), we found that the baseline D_{eff} for W303 *hog1Δ* was 0.157 $\mu m^2\ s^{-1}$ (predicting 23 μM ribosomes) and that this value increased to ~0.462 $\mu m^2\ s^{-1}$ upon 2 h treatment with 1 μM rapamycin (Figure 5C), consistent with an almost one third reduction of ribosome concentration to 15.5 μM (Figure 5C). Deletion of *SFP1* (*sfp1Δ* mutant)

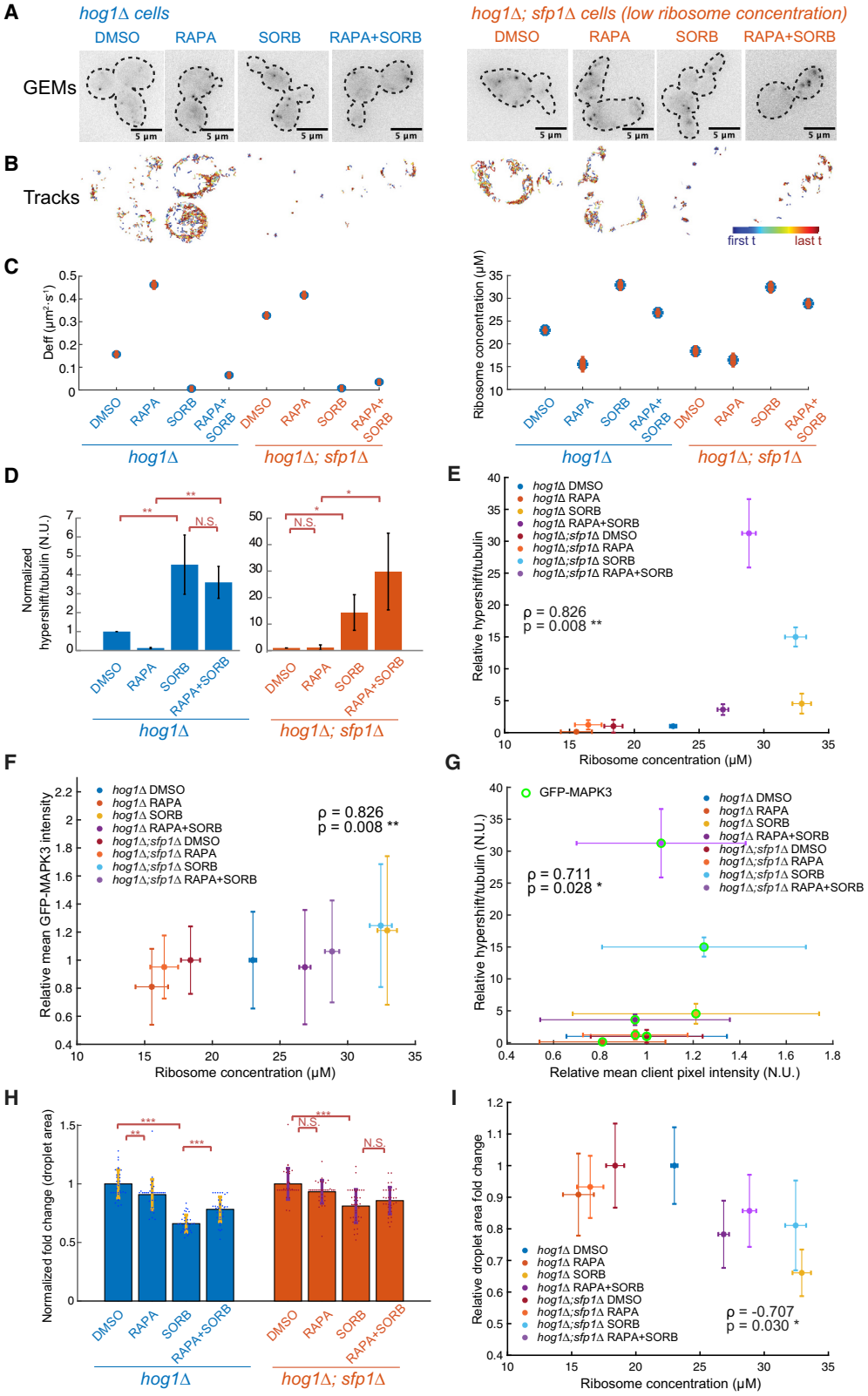

(legend on next page)

gave a similar decrease in ribosome concentration, to 16.4 μM, but in this case, without perturbation to mTORC1 kinase activity (Figure 5C). Osmotic compression of cells with 1M sorbitol for 1 h led to more than 10-fold decrease in 40nm-GEM D_{eff} in all conditions (Figures 5B and 5C), consistent with increased macromolecular crowding to ~ 32 μM ribosome concentration.

To prevent loss of condensates from dominating our results, we expressed sufficient $SUMO_7$-SIM_6 to favor condensate formation even when cytosolic crowding is reduced (Figure S8B). We then quantified hyperphosphorylation of ELK1-SIM in condensates in cells with different levels of crowding (Figures 5D and S8C). Note, total ELK1 levels were affected by rapamycin, osmotic compression, and *SFP1* deletion (Figure S8D); to control for this effect, phosphorylated ELK1 and hypershifted bands were normalized to total ELK1 levels. Hyperphosphorylation was reduced in conditions with decreased macromolecular crowding (e.g., 5-fold decease after rapamycin treatment) and increased in conditions with increased macromolecular crowding (e.g., >4-fold increase after osmotic compression). Plotting hyperphosphorylation as a function of ribosome concentration showed a significant positive correlation (Figure 5E; Spearman's rank $\rho = 0.826$, $p = 0.008 < 0.01$).

We considered mechanisms by which $SUMO_7$-SIM_6 condensates could sense crowding. Our first hypothesis was that the partitioning of clients into condensates could respond to macromolecular crowding, either due to changes in the condensate per se, or due to changes in interactions between the clients and scaffolds (Nakashima et al., 2019). In support of this model, there was a significant positive monotonic correlation between GFP-MAPK3-SIM concentration in condensates and ribosome concentration ($\rho_{GFP-MAPK3} = 0.826$, $p_{GFP-MAPK3} = 0.008 < 0.01$; Figure 5F), and a corresponding correlation between GFP-MAPK3-SIM concentration and fraction hyperphosphorylation ($\rho_{GFP-MAPK3} = 0.711$, $p_{GFP-MAPK3} = 0.028 < 0.05$; Figure 5G). There was also a slight, but not significant positive correlation between mCherry-ELK1-SIM concentration and ribosome concentration ($\rho_{mCherry-ELK1} = 0.347$, $p_{Cherry-ELK1} = 0.198 > 0.05$; Figure S8E) or hyperphosphorylation ($\rho_{mCherry-ELK1} = 0.615$, $p_{Cherry-ELK1} = 0.056 > 0.05$; Figure S8F). Together, these results support the hypothesis that macromolecular crowding tunes GFP-MAPK3-SIM kinase concentration in condensates, leading to modulation of hyperphosphorylation of ELK1-SIM.

We considered compression of condensates as a second mechanism that might couple macromolecular crowding to hyperphosphorylation. We quantified the area of condensates in the same cells before and after 2 h treatment with DMSO (solvent control) or rapamycin (Figures 5H and S8G). Macromolecular crowding impacted both the degree of phase separation of $SUMO_7$-SIM_6 and the area of condensates. The most striking effect was that condensate area was substantially reduced when macromolecular crowding was increased. Increased macromolecular crowding is predicted to increase phase separation and thus increase condensate area. The fact that condensate area is decreased upon osmotic compression suggests that increased macromolecular crowding actually compresses condensates. This hypothesis predicts that condensate area should be negatively correlated with macromolecular crowding. Indeed, we see a significant negative correlation ($\rho_{area} = -0.707$, $p_{area} = 0.03 < 0.05$; Figure 5I). Together, these results support the hypothesis that macromolecular crowding leads to condensate compression, which could increase the density of client-binding sites and therefore drive more efficient hyperphosphorylation.

Phosphorylation of the Alzheimer's disease protein Tau is accelerated in condensates

Aggregation of the microtubule-associated protein, Tau, is tightly linked to the development of Alzheimer's and other neurodegenerative diseases termed tauopathies (Kovacs, 2017; Soria Lopez et al., 2019). The pathological hallmark of tauopathies are neurofibrillary tangles of hyper-phosphorylated Tau (Ihara et al., 1986). Phosphorylation destabilizes the interaction of Tau with microtubules causing mislocalization of Tau from axons to the somatodendritic compartment in neurons (Zempel and Mandelkow, 2015). It has been suggested that the concentration of Tau into liquid-like condensates could promote its conversion into fibrillar structures and thus be a critical step in Tau-induced neurotoxicity (Ambadipudi et al., 2017; Wegmann et al., 2018; Zhang et al., 2017). Multiple kinases have been reported to phosphorylate Tau (Wesseling et al., 2020), including the CDK2/Cyclin A1 complex (CDK2/CycA1) (Lee et al., 2017). However, little is known about the ability of kinases to phosphorylate Tau inside condensates and whether Tau condensation might promote Tau phosphorylation. Based on our results from synthetic

Figure 5. Synthetic condensed-phase signaling responds to changes in macromolecular crowding

(A) Representative micrographs of cells with 40 nm GEMs.

(B) Projections of GEM trajectories. Scale bars, 5 μm.

(C) Median effective diffusion coefficients D_{eff} of GEMs (left) and estimated ribosome concentrations (right) of each condition. Error bars are standard error of mean (SEM).

(D) ELK1 hyperphosphorylation levels of each strain are normalized to the mean value in DMSO; bar graphs show mean ± standard deviation (SD) (n = 3).

(E) ELK1 hyperphosphorylation shows a significant positive correlation with ribosome concentrations. Vertical error bars, SD; horizontal error bars, SEM.

(F) GFP-MAPK3-SIM intensity in condensates of each strain are normalized to the mean value of DMSO condition. There is significant positive correlation between GFP-MAPK3-SIM intensity in condensates and ribosome concentration. Vertical error bars, SD; horizontal error bars, SEM.

(G) Significant positive Spearman's rank correlation between ELK1 hyperphosphorylation and GFP-MAPK3-SIM intensity in condensates. Both vertical and horizontal error bars are SD.

(H) Fold change of $SUMO_7$-SIM_6 condensate area was measured for the same droplet before and after each treatment, and then the values were normalized to the mean value of DMSO condition of each strain. Left: mean value ± SD of normalized area fold change; each point represents a single droplet (n > 30).

(I) Significant negative Spearman's rank correlation between droplet area fold change and ribosome concentration. Vertical error bars are SD; horizontal error bars are SEM. All statistical comparisons are performed using pairwise Tukey-Kramer test: *p < 0.05, **p < 0.01, ***p < 0.001, N.S., not significant.

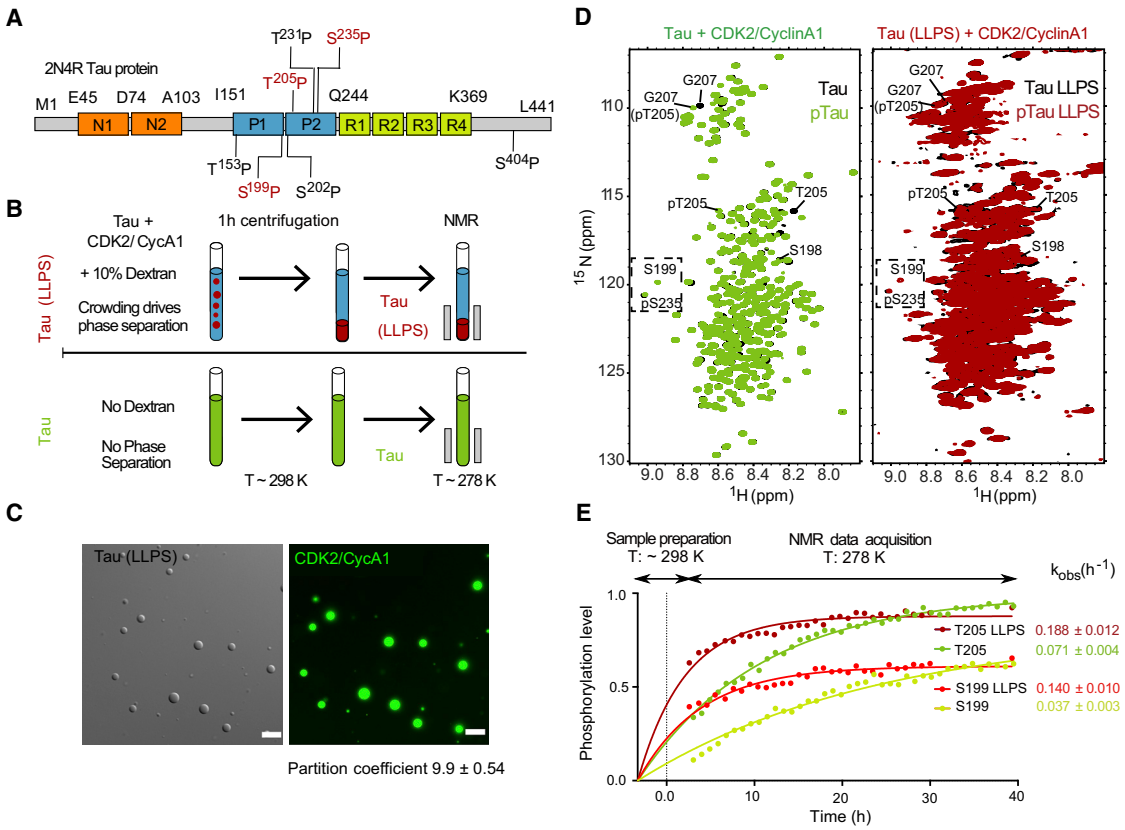

Figure 6. Phosphorylation of the Alzheimer's disease protein Tau is accelerated in condensates

(A) Domain organization of 2N4R Tau protein. Phosphorylation sites targeted by CDK2/CyclinA1 are indicated. Phosphorylated residues analyzed are displayed in red.

(B) Schematic of sample preparation. Phase separation only occurs in samples with dextran crowding agent.

(C) Fluorescence microscopy demonstrating recruitment of CDK2/CyclinA1-Alexa 488 into Tau droplets. Phase separation of Tau (40 μM) was promoted with 10% dextran. Tau and CDK2/CyclinA1-Alexa 488 were mixed using the identical molar ratio as used for the NMR experiments. The partition coefficient of CDK2/CycA1-Alexa 488 inside the tau droplets was 9.9 ± 0.54 based on fluorescence intensity analysis. Scale bars, 10 μm.

(D) Two-dimensional ^{1}H-^{15}N NMR spectroscopy. ^{1}H-^{15}N correlation spectra of Tau immediately after centrifugation are displayed in black (left panel: dispersed phase; right panel: Tau condensate). The last recorded spectrum (after ~40 h) is displayed in green (left panel, dispersed phase) or red (right panel, tau condensate). Cross-peaks of phosphorylated S235 and S199 are boxed and labeled as pS235 and pS199.

(E) Phosphorylation kinetics of S199 and T205 inside Tau condensates (red: S199; magenta: T205) and in the dispersed phase (light green: S199; green: T205). Note that the fit is extrapolated to a negative time value as a consequence of the temperature difference between sample preparation (T: 298 K) and NMR data acquisition (T: 278 K) and the phosphorylation that occurs during the centrifugation period.

condensates, we hypothesized that Tau phosphorylation might be accelerated in the condensed phase.

We used high-resolution NMR spectroscopy to compare Tau phosphorylation rates in the dispersed and condensed phases. We prepared ^{15}N-labeled 4R Tau (Figure 6A) without or with the molecular crowding agent dextran (Figure 6B). In our buffer conditions, which include approximately physiological levels of magnesium and ATP (5.6 mM $MgCl_2$, 5.6 mM ATP), phase separation only occurred in the sample with 10% dextran (Ukmar-Godec et al., 2019). CDK2/CycA1 was then added to both samples. CDK2/CycA1 phosphorylates Tau *in vitro* at phosphoepitopes associated with Alzheimer's disease (Kovacs, 2017; Savastano et al., 2021; Soria Lopez et al., 2019). We labeled CDK2/CycA1 with Alexa 488 and found strong enrichment in the condensed phase of the dextran-containing sample (partition coefficient 9.9 ± 0.54, Figure 6C). Prior to NMR measurement both samples were centrifuged for 1 h to sediment the Tau condensate in the dextran-containing sample at the bottom of the NMR tube (Figure 6B). The identical protocol in the absence of dextran created a sample without condensate allowing us to evaluate the influence of Tau condensation on Tau phosphorylation.

We recorded two-dimensional ^{1}H–^{15}N correlation spectra to quantify phosphorylation of specific Tau residues in real time (Figure 6D). Without dextran, the NMR cross-peaks displayed line shapes previously reported for Tau in the dilute phase (Figure 6D, left) (Mukrasch et al., 2009). Comparison of the first spectrum recorded after the one 1 h centrifugation period (black spectrum Figure 6D, left) with previously reported NMR spectra of unmodified Tau revealed a phosphorylation-specific cross peak for the serine residue S235 (labeled as pS235). Tau was

thus already mostly phosphorylated at S235 during sample preparation; therefore, we did not further analyze S235. In contrast, we were able to analyze phosphorylation kinetics at S199 and T205 (see green spectrum in Figure 6D, left). Cdk2/CycA1 thus rapidly phosphorylates Tau at S235, followed by phosphorylation at T205 and S199. Notably, the NMR experiments were performed at 278K (4.85°C) to improve spectral quality (due to decreased solvent exchange at low temperature) and to slow down the kinetics of phosphorylation. The changes of NMR signal position and intensity of all nonoverlapping residues indicated that CDK2/CycA1-phosphorylation only induces small, mostly local changes near the phosphorylation sites to the ensemble of Tau conformations (Figures S9A and S9B), that this lower temperature did not disrupt condensation, and that condensates did not age detectably during the experiment (Figures S9A and B). Continuous repetition of the NMR experiments over a time period of 40 h allowed the site-specific quantification of Tau phosphorylation.

Two-dimensional ^{1}H–^{15}N correlation spectra were also obtained for the sample containing the Tau condensate (right panel of Figure 6D). In agreement with previous NMR studies of condensates of intrinsically disordered proteins (e.g., Burke et al., 2015), the NMR signals were broadened due to the altered physicochemical environment (Abyzov et al., 2022). Nevertheless, we still observed the phosphorylation-specific cross peak of S235 in the spectrum recorded immediately after the 1 h centrifugation period (marked as pS235 in the black spectrum in Figure 6D, right). Thus, both in the dispersed and condensed phase, S235, which is part of the AT180 epitope, is most rapidly phosphorylated by CDK2/CycA1.

Next, we quantified the rate of phosphorylation of S199 and T205 from 40 h of repetitive ^{1}H–^{15}N correlation spectra measurements (Figure 6E). All four kinetic curves (S199 and T205 in the dispersed and condensed states) were simultaneously fit to a mono-exponential function. The fit includes a fixed phosphorylation level of 0.0 at a "negative" time point, which accounts for the 1 h of sample preparation time before the first ^{1}H–^{15}N correlation spectrum could be collected. Kinetic traces (Figure 6E) clearly showed that rates of phosphorylation of both sites were increased in the condensed phase (~3.8-fold at S199 and ~2.6-fold at T205). Thus, phosphorylation of S199 and T205, part of the Alzheimer's-disease-characteristic AT8 epitope, is accelerated in Tau condensates.

DISCUSSION

Condensates facilitate phosphoregulatory network rewiring

We found that new, dynamic kinase-substrate connections can be generated more easily within condensates than in solution, including at non-consensus phospho-acceptor motifs. It will be interesting to investigate whether the activity and substrate specificity of endogenous kinases is altered in natural condensates. The consensus sequences that are often used to predict kinase substrates may be less important in the context of condensed-phase signaling, and a larger number of possible phosphorylation sites may need to be investigated. For example, it has been shown that the crucial regulatory sites of some kinase substrates are actually at non-canonical sites; for example, degradation of the yeast cell cycle regulator Sic1 is triggered by multi-site phosphorylation including non-consensus Cdk1 sites (Kõivomägi et al., 2011; Nash et al., 2001). By extension, kinase-substrate interactions within condensates could lead to unexpected modes of phosphoregulation.

A further prediction of the ease with which we generated dynamic phosphorylation within condensates is that recruitment to condensates may facilitate the evolution of new links in phosphoregulatory networks. Phosphorylation can occur in condensates even in the absence of any obvious docking or consensus sites. It is possible that these initial phosphorylation events could provide a starting point from which useful regulation could evolve.

When mutations lead to new recruitment of kinases or substrates into condensates, more promiscuous phosphorylation could lead to gain or loss of function. For example, useful new links in phosphoregulatory networks could increase fitness, or toxic, off-target phosphorylation events, could decrease fitness. Intuitively, it seems that loss of fitness would be very likely, but in fact, we previously demonstrated that expansion of kinase specificity can be surprisingly well tolerated (Howard et al, 2014). On the other hand, our results in this study show that phosphorylation events associated with Alzheimer's disease are accelerated within Tau condensates.

Beyond mass action: Condensate flexibility and high densities of client-binding sites are important for efficient condensed-phase signaling

Recently, a number of studies have reported acceleration of biochemical activities in condensates (Huang et al., 2019; Peeples and Rosen, 2021; Poudyal et al., 2019). A recent study (Peeples and Rosen, 2021) found that reactions were accelerated by mass action. In addition, they found that certain scaffolds decreased the effective K_M of the reaction, suggesting that molecular organization was important for strong activity enhancement. Our results suggest that a flexible scaffold molecule and a large excess of client-binding sites are the most important determinants of hyperphosphorylation. We speculate that dense local clusters of binding sites organize clients within local reaction crucibles that enable processive multi-site phosphorylation.

Synthetic condensed-phase signaling can respond to biophysical changes

Recently, we found that macromolecular crowding can strongly affect biomolecular condensation (Delarue et al., 2018). Several recent examples of endogenous condensates have been reported to respond to macromolecular crowding (Cai et al., 2019). This leads to the hypothesis that there is an axis of control spanning from the global biophysical state of the cell, to mesoscale phase separation, and finally to molecular-scale biochemical reactions. We found that the degree of hyperphosphorylation in condensates responded to changes in macromolecular crowding. The ability of condensed-phase chemical reactions to respond to macromolecular crowding presents exciting new possibilities for both synthetic biology and the elucidation of new mechanisms of biological regulation and homeostasis. For example, the mechanisms that sense mechanical compression

remain poorly understood (Delarue et al., 2018), but mechanical compression leads to increases in macromolecular crowding (Alric et al., 2022); we have now demonstrated that the macromolecular crowding can modulate phosphorylation rates within condensates.

Condensed-phase phosphorylation could contribute to disease

Finally, we investigated whether naturally occurring condensates could modulate phosphorylation kinetics. Our synthetic condensates greatly increased the hyperphosphorylation of proteins. We therefore sought endogenous proteins that are associated with both condensates and hyperphosphorylation. The microtubule-associated protein Tau was a strong candidate: neurofibrillary tangles (aggregates) of hyper-phosphorylated Tau are a pathological hallmark of Alzheimer's disease (Ihara et al., 1986). Furthermore, it has been suggested that the concentration of Tau into liquid-like condensates could be an initial step in the conversion to neurofibrillary tangles (Ambadipudi et al., 2017; Wegmann et al., 2018; Zhang et al., 2017). We found phosphorylation of the Alzheimer's disease-associated AT8 epitope was accelerated 3-fold within the condensed phase. Notably, molecular crowding was required to see these effects in our reconstituted *in vitro* system. This result relates our insights from synthetic biology to possible new mechanisms for neurodegenerative disease.

Limitations of the study

In our *in vitro* experiments, we initially tried to pre-form condensates and then start reactions by addition of ATP. However, it was difficult to mix the reactions properly without disrupting the condensates. Therefore, to get reproducible results, we simultaneously formed droplets and started the kinase reaction. This approach conflates droplet formation kinetics with the kinase reaction kinetics, but condensation was similar between all conditions, allowing meaningful comparisons.

We found that p53, RPS6, and non-consensus Ser in ELK1 could all be phosphorylated by MAPK3 within synthetic condensates. The sequences surrounding the phosphorylation sites are all distinct. We currently do not understand if there are rules or patterns for kinase specificity in condensates or whether kinases like MAPK3 phosphorylate any exposed serine or threonine. However, in Figure S4H, we are able to mostly abrogate slowly migrating species in the western blot by mutating four of 100 possible phosphor-acceptor residues (77 serines, 23 threoninies) in the sequence, suggesting that phosphorylation of the min383 substrate in the condensed phase is not completely promiscuous. In future work, it will be interesting to undertake phosphoproteomics studies to get a sense of the degree to which kinase specificity is expanded.

We attempted fluorescence recovery after photobleaching (FRAP) and photoconversion experiments to quantify diffusion of clients within synthetic condensates. However, the small size of the condensates and rapid diffusion dynamics made it very difficult for us to get reliable results.

We would have liked to gain information about non-canonical phosphorylation events within Tau condensates, but the peak broadening in the condensed phase limited our ability to quantify phosphorylation of additional sites.

Compared with our synthetic systems, we have limited understanding of the mechanisms of reaction acceleration in Tau condensates, and whether mass action is sufficient to explain the effect.

Differences in *in vivo* hyperphosphorylation *in vivo* were on the order of 100-fold, whereas *in vitro* effects were smaller (2-fold to 3-fold). We speculate that systems-level effects, such as competition with phosphatases, magnify differences *in vivo*.

STAR★METHODS

Detailed methods are provided in the online version of this paper and include the following:

- KEY RESOURCES TABLE
- RESOURCE AVAILABILITY
  - Lead contact
  - Materials availability
  - Data and code availability
- EXPERIMENTAL MODEL AND SUBJECT DETAILS
  - Escherichia coli strains
  - Yeast strains
- METHOD DETAILS
  - Yeast transformation
  - Plasmid construction
  - Protein purification
  - *In vitro* kinase assays
  - MAPK3-GFP total partition calculation
  - Western blots
  - Cell perturbations
  - Phosphatase treatment of yeast lysates
  - Imaging and quantification of fluorescence intensity inside condensates and condensate size
  - HILO imaging of GEMs
  - Calculation of effective diffusion constant
  - Relative ribosome concentration calculation
  - NMR Methods
- CDK2/CyclinA1-ALEXA 488 LABELLING
- QUANTIFICATION AND STATISTICAL ANALYSIS

SUPPLEMENTAL INFORMATION

Supplemental information can be found online at https://doi.org/10.1016/j.molcel.2022.08.016.

ACKNOWLEDGMENTS

We thank Michael Rosen, Allyson Rice, and members of the HHMI Summer Institute at the Marine Biology Institute in Woods Hole for discussions that initiated this project. We thank Jef Boeke, David Engelberg, Meta Heidenreich, and Emmanuel D. Levy for sharing yeast strains and plasmids, and Greg Brittingham for help with imaging and analysis. We thank Lance Denes and Srinjoy Sil for critical reading of the manuscript. We thank the rest of the Holt lab for helpful discussions. We thank Maria-Sol Cima-Omori for preparation of ^{15}N-labeled Tau. C.F.P. acknowledges the Deutsche Akademischer Austauschdienst (DAAD) for the Research Grants Doctoral program in Germany, 2019/20 (personal ref. no. 91726791) and M.Z. was supported by the European Research Council (ERC) under the EU Horizon 2020 research and innovation program (grant agreement no. 787679). L.J.H. was funded by NIH R01 GM132447 and R37 CA240765, a donation to the American Cancer Society from the Cornelia T. Bailey Foundation, the Pershing Square Sohn Cancer

Research Award, the Chan Zuckerberg Initiative, the NIH Director's Transformative Research Award TR01 NS127186, and the Air Force Office of Scientific Research (AFoSR) Multidisciplinary University Research Initiative (MURI) competition (grant FA9550-21-1-3503 0091).

AUTHOR CONTRIBUTIONS

D.S. and T.S. undertook all experiments and analysis except NMR, supervised by L.J.H. C.F.P. undertook NMR experiments with analysis help from AIdO, supervised by M.Z. All authors contributed to writing and editing the manuscript.

DECLARATION OF INTERESTS

The authors declare no competing interests.

Received: December 8, 2021
Revised: May 18, 2022
Accepted: August 12, 2022
Published: September 14, 2022

REFERENCES

Abyzov, A., Blackledge, M., and Zweckstetter, M. (2022). Conformational dynamics of intrinsically disordered proteins regulate biomolecular condensate chemistry. Chem. Rev. *122*, 6719–6748.

Agmon, N., Mitchell, L.A., Cai, Y., Ikushima, S., Chuang, J., Zheng, A., Choi, W.J., Martin, J.A., Caravelli, K., Stracquadanio, G., and Boeke, J.D. (2015). Yeast golden gate (yGG) for the efficient assembly of *S. cerevisiae* transcription units. ACS Synth. Biol. *4*, 853–859.

Alberti, S., and Hyman, A.A. (2021). Biomolecular condensates at the nexus of cellular stress, protein aggregation disease and ageing. Nat. Rev. Mol. Cell Biol. *22*, 196–213.

Alexander, J., Lim, D., Joughin, B.A., Hegemann, B., Hutchins, J.R., Ehrenberger, T., Ivins, F., Sessa, F., Hudecz, O., Nigg, E.A., et al. (2011). Spatial exclusivity combined with positive and negative selection of phosphorylation motifs is the basis for context-dependent mitotic signaling. Sci. Signal. *4*, ra42.

Alric, B., Formosa-Dague, C., Dague, E., Holt, L.J., and Delarue, M. (2022). Macromolecular crowding limits growth under pressure. Nat. Phys. *18*, 411–416.

Ambadipudi, S., Biernat, J., Riedel, D., Mandelkow, E., and Zweckstetter, M. (2017). Liquid-liquid phase separation of the microtubule-binding repeats of the Alzheimer-related protein Tau. Nat. Commun. *8*, 275.

Amberg, D.C., Burke, D.J., and Strathern, J.N. (2006). High-efficiency transformation of yeast. CSH Protoc *2006*. pdb.prot4145.

Bähler, J., Wu, J.Q., Longtine, M.S., Shah, N.G., McKenzie, A., 3rd, Steever, A.B., Wach, A., Philippsen, P., and Pringle, J.R. (1998). Heterologous modules for efficient and versatile PCR-based gene targeting in *Schizosaccharomyces pombe*. Yeast *14*, 943–951.

Banani, S.F., Lee, H.O., Hyman, A.A., and Rosen, M.K. (2017). Biomolecular condensates: organizers of cellular biochemistry. Nat. Rev. Mol. Cell Biol. *18*, 285–298.

Banani, S.F., Rice, A.M., Peeples, W.B., Lin, Y., Jain, S., Parker, R., and Rosen, M.K. (2016). Compositional control of phase-separated cellular bodies. Cell *166*, 651–663.

Beauclair, G., Bridier-Nahmias, A., Zagury, J.F., Saïb, A., and Zamborlini, A. (2015). JASSA: a comprehensive tool for prediction of SUMOylation sites and SIMs. Bioinformatics *31*, 3483–3491.

Borchers, H.W., and Borchers, M.H.W. (2021). Package 'pracma'. (CRAN).

Bracha, D., Walls, M.T., Wei, M.T., Zhu, L., Kurian, M., Avalos, J.L., Toettcher, J.E., and Brangwynne, C.P. (2019). Mapping local and global liquid phase behavior in living cells using photo-oligomerizable seeds. Cell *176*, 407.

Burke, K.A., Janke, A.M., Rhine, C.L., and Fawzi, N.L. (2015). Residue-by-residue view of in vitro FUS granules that bind the C-terminal domain of RNA polymerase II. Mol. Cell *60*, 231–241.

Cai, D., Feliciano, D., Dong, P., Flores, E., Gruebele, M., Porat-Shliom, N., Sukenik, S., Liu, Z., and Lippincott-Schwartz, J. (2019). Phase separation of YAP reorganizes genome topology for long-term YAP target gene expression. Nat. Cell Biol. *21*, 1578–1589.

Cicenas, J., Zalyte, E., Bairoch, A., and Gaudet, P. (2018). Kinases and cancer. Cancers (Basel) *10*, 63.

Cruzalegui, F.H., Cano, E., and Treisman, R. (1999). ERK activation induces phosphorylation of Elk-1 at multiple S/T-P motifs to high stoichiometry. Oncogene *18*, 7948–7957.

Delaglio, F., Grzesiek, S., Vuister, G.W., Zhu, G., Pfeifer, J., and Bax, A. (1995). NMRPipe: a multidimensional spectral processing system based on UNIX pipes. J. Biomol. NMR *6*, 277–293.

Delarue, M., Brittingham, G.P., Pfeffer, S., Surovtsev, I.V., Pinglay, S., Kennedy, K.J., Schaffer, M., Gutierrez, J.I., Sang, D., Poterewicz, G., et al. (2018). mTORC1 controls phase separation and the biophysical properties of the cytoplasm by tuning crowding. Cell *174*, 338–349.e20.

Doolittle, A.K. (1951). Studies in Newtonian flow. II. The dependence of the viscosity of liquids on free-space. J. Appl. Phys. *22*, 1471–1475.

Elion, E.A. (2000). Pheromone response, mating and cell biology. Curr. Opin. Microbiol. *3*, 573–581.

Ellis, R.J., and Minton, A.P. (2003). Join the crowd. Nature *425*, 27–28.

Enserink, J.M., and Kolodner, R.D. (2010). An overview of Cdk1-controlled targets and processes. Cell Div *5*, 11.

Evans, E.L., Saxton, J., Shelton, S.J., Begitt, A., Holliday, N.D., Hipskind, R.A., and Shaw, P.E. (2011). Dimer formation and conformational flexibility ensure cytoplasmic stability and nuclear accumulation of Elk-1. Nucleic Acids Res *39*, 6390–6402.

Faustova, I., Bulatovic, L., Matiyevskaya, F., Valk, E., Örd, M., and Loog, M. (2021). A new linear cyclin docking motif that mediates exclusively S-phase CDK-specific signaling. EMBO J *40*, e105839.

Gibson, D.G., Young, L., Chuang, R.Y., Venter, J.C., Hutchison, C.A., 3rd, and Smith, H.O. (2009). Enzymatic assembly of DNA molecules up to several hundred kilobases. Nat. Methods *6*, 343–345.

Hastings, R.L., and Boeynaems, S. (2021). Designer condensates: a toolkit for the biomolecular architect. J. Mol. Biol. *433*, 166837.

Heidenreich, M., Georgeson, J.M., Locatelli, E., Rovigatti, L., Nandi, S.K., Steinberg, A., Nadav, Y., Shimoni, E., Safran, S.A., Doye, J.P.K., and Levy, E.D. (2020). Designer protein assemblies with tunable phase diagrams in living cells. Nat. Chem. Biol. *16*, 939–945.

Hohmann, S. (2002). Osmotic stress signaling and osmoadaptation in yeasts. Microbiol. Mol. Biol. Rev. *66*, 300–372.

Howard, C.J., Hanson-Smith, V., Kennedy, K.J., Miller, C.J., Lou, H.J., Johnson, A.D., Turk, B.E., and Holt, L.J. (2014). Ancestral resurrection reveals evolutionary mechanisms of kinase plasticity. eLife *3*, e04126.

Huang, W.Y.C., Alvarez, S., Kondo, Y., Lee, Y.K., Chung, J.K., Lam, H.Y.M., Biswas, K.H., Kuriyan, J., and Groves, J.T. (2019). A molecular assembly phase transition and kinetic proofreading modulate Ras activation by SOS. Science *363*, 1098–1103.

Ihara, Y., Nukina, N., Miura, R., and Ogawara, M. (1986). Phosphorylated Tau protein is integrated into paired helical filaments in Alzheimer's disease. J. Biochem. *99*, 1807–1810.

Kõivomägi, M., Valk, E., Venta, R., Iofik, A., Lepiku, M., Balog, E.R., Rubin, S.M., Morgan, D.O., and Loog, M. (2011). Cascades of multisite phosphorylation control Sic1 destruction at the onset of S phase. Nature *480*, 128–131.

Kovacs, G.G. (2017). Tauopathies. Handb. Clin. Neurol. *145*, 355–368.

Lee, D.S.W., Wingreen, N.S., and Brangwynne, C.P. (2021). Chromatin mechanics dictates subdiffusion and coarsening dynamics of embedded condensates. Nat. Phys. *17*, 531–538.

Lee, K.H., Lee, S.J., Lee, H.J., Choi, G.E., Jung, Y.H., Kim, D.I., Gabr, A.A., Ryu, J.M., and Han, H.J. (2017). Amyloid beta1-42 (Abeta1-42) induces the CDK2-mediated phosphorylation of Tau through the activation of the

mTORC1 signaling pathway while promoting neuronal cell death. Front. Mol. Neurosci. *10*, 229.

Lee, W., Tonelli, M., and Markley, J.L. (2015). NMRFAM-SPARKY: enhanced software for biomolecular NMR spectroscopy. Bioinformatics *31*, 1325–1327.

Levin-Salomon, V., Kogan, K., Ahn, N.G., Livnah, O., and Engelberg, D. (2008). Isolation of intrinsically active (MEK-independent) variants of the ERK family of mitogen-activated protein (MAP) kinases. J. Biol. Chem. *283*, 34500–34510.

Li, P., Banjade, S., Cheng, H.C., Kim, S., Chen, B., Guo, L., Llaguno, M., Hollingsworth, J.V., King, D.S., Banani, S.F., et al. (2012). Phase transitions in the assembly of multivalent signalling proteins. Nature *483*, 336–340.

Li, W., Hamill, S.J., Hemmings, A.M., Moore, G.R., James, R., and Kleanthous, C. (1998). Dual recognition and the role of specificity-determining residues in colicin E9 DNase-immunity protein interactions. Biochemistry *37*, 11771–11779.

Luby-Phelps, K. (1999). Cytoarchitecture and physical properties of cytoplasm: volume, viscosity, diffusion, intracellular surface area. In International review of cytology, H. Walter, D.E. Brooks, and P.A. Srere, eds. (Academic Press), pp. 189–221.

Malumbres, M. (2014). Cyclin-dependent kinases. Genome Biol *15*, 122.

Miller, C.J., and Turk, B.E. (2018). Homing in: mechanisms of substrate targeting by protein kinases. Trends Biochem. Sci. *43*, 380–394.

Miyamoto, T., DeRose, R., Suarez, A., Ueno, T., Chen, M., Sun, T.P., Wolfgang, M.J., Mukherjee, C., Meyers, D.J., and Inoue, T. (2012). Rapid and orthogonal logic gating with a gibberellin-induced dimerization system. Nat. Chem. Biol. *8*, 465–470.

Mok, J., Kim, P.M., Lam, H.Y., Piccirillo, S., Zhou, X., Jeschke, G.R., Sheridan, D.L., Parker, S.A., Desai, V., Jwa, M., et al. (2010). Deciphering protein kinase specificity through large-scale analysis of yeast phosphorylation site motifs. Sci. Signal. *3*, ra12.

Mukrasch, M.D., Bibow, S., Korukottu, J., Jeganathan, S., Biernat, J., Griesinger, C., Mandelkow, E., and Zweckstetter, M. (2009). Structural polymorphism of 441-residue Tau at single residue resolution. PLoS Biol *7*, e34.

Mylona, A., Theillet, F.X., Foster, C., Cheng, T.M., Miralles, F., Bates, P.A., Selenko, P., and Treisman, R. (2016). Opposing effects of Elk-1 multisite phosphorylation shape its response to ERK activation. Science *354*, 233–237.

Nakashima, K.K., Vibhute, M.A., and Spruijt, E. (2019). Biomolecular chemistry in liquid phase separated compartments. Front. Mol. Biosci. *6*, 21.

Namanja, A.T., Li, Y.J., Su, Y., Wong, S., Lu, J., Colson, L.T., Wu, C., Li, S.S., and Chen, Y. (2012). Insights into high affinity small ubiquitin-like modifier (SUMO) recognition by SUMO-interacting motifs (SIMs) revealed by a combination of NMR and peptide array analysis. J. Biol. Chem. *287*, 3231–3240.

Nash, P., Tang, X., Orlicky, S., Chen, Q., Gertler, F.B., Mendenhall, M.D., Sicheri, F., Pawson, T., and Tyers, M. (2001). Multisite phosphorylation of a CDK inhibitor sets a threshold for the onset of DNA replication. Nature *414*, 514–521.

Örd, M., and Loog, M. (2019). How the cell cycle clock ticks. Mol. Biol. Cell *30*, 169–172.

Örd, M., Möll, K., Agerova, A., Kivi, R., Faustova, I., Venta, R., Valk, E., and Loog, M. (2019). Multisite phosphorylation code of CDK. Nat. Struct. Mol. Biol. *26*, 649–658.

O'Rourke, S.M., and Herskowitz, I. (1998). The Hog1 MAPK prevents cross talk between the HOG and pheromone response MAPK pathways in *Saccharomyces cerevisiae*. Genes Dev *12*, 2874–2886.

Peeples, W., and Rosen, M.K. (2021). Mechanistic dissection of increased enzymatic rate in a phase-separated compartment. Nat. Chem. Biol. *17*, 693–702.

Poudyal, R.R., Guth-Metzler, R.M., Veenis, A.J., Frankel, E.A., Keating, C.D., and Bevilacqua, P.C. (2019). Template-directed RNA polymerization and enhanced ribozyme catalysis inside membraneless compartments formed by coacervates. Nat. Commun. *10*, 490.

Rawat, P., Boehning, M., Hummel, B., Aprile-Garcia, F., Pandit, A.S., Eisenhardt, N., Khavaran, A., Niskanen, E., Vos, S.M., Palvimo, J.J., et al. (2021). Stress-induced nuclear condensation of NELF drives transcriptional downregulation. Mol. Cell *81*, 1013–102.6.e11.

Reményi, A., Good, M.C., and Lim, W.A. (2006). Docking interactions in protein kinase and phosphatase networks. Curr. Opin. Struct. Biol. *16*, 676–685.

Savastano, A., Flores, D., Kadavath, H., Biernat, J., Mandelkow, E., and Zweckstetter, M. (2021). Disease-associated Tau phosphorylation hinders tubulin assembly within Tau condensates. Angew. Chem. Int. Ed. Engl. *60*, 726–730.

Schindelin, J., Arganda-Carreras, I., Frise, E., Kaynig, V., Longair, M., Pietzsch, T., Preibisch, S., Rueden, C., Saalfeld, S., Schmid, B., et al. (2012). Fiji: an open-source platform for biological-image analysis. Nat. Methods *9*, 676–682.

Schindelin, J., Rueden, C.T., Hiner, M.C., and Eliceiri, K.W. (2015). The ImageJ ecosystem: an open platform for biomedical image analysis. Mol. Reprod. Dev. *82*, 518–529.

Schulman, B.A., Lindstrom, D.L., and Harlow, E. (1998). Substrate recruitment to cyclin-dependent kinase 2 by a multipurpose docking site on cyclin A. Proc. Natl. Acad. Sci. USA *95*, 10453–10458.

Shin, Y., Berry, J., Pannucci, N., Haataja, M.P., Toettcher, J.E., and Brangwynne, C.P. (2017). Spatiotemporal control of intracellular phase transitions using light-activated optoDroplets. Cell *168*, 159–171.e14.

Shin, Y., and Brangwynne, C.P. (2017). Liquid phase condensation in cell physiology and disease. Science *357*, eaaf4382.

Shivanandan, A., Radenovic, A., and Sbalzarini, I.F. (2013). MosaicIA: an ImageJ/Fiji plugin for spatial pattern and interaction analysis. BMC Bioinformatics *14*, 349.

Sikorski, R.S., and Hieter, P. (1989). A system of shuttle vectors and yeast host strains designed for efficient manipulation of DNA in *Saccharomyces cerevisiae*. Genetics *122*, 19–27.

Soria Lopez, J.A., González, H.M., and Léger, G.C. (2019). Alzheimer's disease. Handb. Clin. Neurol. *167*, 231–255.

Stegmeier, F., and Amon, A. (2004). Closing mitosis: the functions of the Cdc14 phosphatase and its regulation. Annu. Rev. Genet. *38*, 203–232.

Tang, X., Orlicky, S., Mittag, T., Csizmok, V., Pawson, T., Forman-Kay, J.D., Sicheri, F., and Tyers, M. (2012). Composite low affinity interactions dictate recognition of the cyclin-dependent kinase inhibitor Sic1 by the SCFCdc4 ubiquitin ligase. Proc. Natl. Acad. Sci. USA *109*, 3287–3292.

Tinevez, J.Y., Perry, N., Schindelin, J., Hoopes, G.M., Reynolds, G.D., Laplantine, E., Bednarek, S.Y., Shorte, S.L., and Eliceiri, K.W. (2017). TrackMate: an open and extensible platform for single-particle tracking. Methods *115*, 80–90.

Ukmar-Godec, T., Hutten, S., Grieshop, M.P., Rezaei-Ghaleh, N., Cima-Omori, M.S., Biernat, J., Mandelkow, E., Söding, J., Dormann, D., and Zweckstetter, M. (2019). Lysine/RNA-interactions drive and regulate biomolecular condensation. Nat. Commun. *10*, 2909. https://doi.org/10.1038/s41467-019-10792-y.

Verdecia, M.A., Bowman, M.E., Lu, K.P., Hunter, T., and Noel, J.P. (2000). Structural basis for phosphoserine-proline recognition by group IV WW domains. Nat. Struct. Biol. *7*, 639–643.

Visintin, R., Craig, K., Hwang, E.S., Prinz, S., Tyers, M., and Amon, A. (1998). The phosphatase Cdc14 triggers mitotic exit by reversal of Cdk-dependent phosphorylation. Mol. Cell *2*, 709–718.

Wegmann, S., Eftekharzadeh, B., Tepper, K., Zoltowska, K.M., Bennett, R.E., Dujardin, S., Laskowski, P.R., MacKenzie, D., Kamath, T., Commins, C., et al. (2018). Tau protein liquid-liquid phase separation can initiate Tau aggregation. EMBO J *37*.

Wesseling, H., Mair, W., Kumar, M., Schlaffner, C.N., Tang, S., Beerepoot, P., Fatou, B., Guise, A.J., Cheng, L., Takeda, S., et al. (2020). Tau PTM profiles identify patient heterogeneity and stages of Alzheimer's disease. Cell *183*, 1699–1713.e13.

Wippich, F., Bodenmiller, B., Trajkovska, M.G., Wanka, S., Aebersold, R., and Pelkmans, L. (2013). Dual specificity kinase DYRK3 couples stress granule condensation/dissolution to mTORC1 signaling. Cell *152*, 791–805.

Zempel, H., and Mandelkow, E.M. (2015). Tau missorting and spastin-induced microtubule disruption in neurodegeneration: Alzheimer disease and hereditary spastic paraplegia. Mol. Neurodegener. *10*, 68.

Zhang, H., Cao, X., Tang, M., Zhong, G., Si, Y., Li, H., Zhu, F., Liao, Q., Li, L., Zhao, J., et al. (2021a). A subcellular map of the human kinome. eLife *10*, e64943.

Zhang, X., Lin, Y., Eschmann, N.A., Zhou, H., Rauch, J.N., Hernandez, I., Guzman, E., Kosik, K.S., and Han, S. (2017). RNA stores Tau reversibly in complex coacervates. PLoS Biol *15*, e2002183.

Zhang, Y., Lee, D.S.W., Meir, Y., Brangwynne, C.P., and Wingreen, N.S. (2021b). Mechanical frustration of phase separation in the cell nucleus by chromatin. Phys. Rev. Lett. *126*, 258102.

STAR★METHODS

KEY RESOURCES TABLE

REAGENT or RESOURCE	SOURCE	IDENTIFIER
Antibodies		
anti-Elk1	9182	Cell signaling; RRID: AB_2277936
anti-p-Elk1(Ser383)	9181	Cell signaling; RRID: AB_2099016
anti-p-Erk1(T202/Y204)	4377	Cell signaling; RRID: AB_331775
anti-HA	12CA5	Roche; RRID: AB_2920713
anti-p-P53(S37)	9289	Cell signaling; RRID: AB_2210689
anti-p-P53(S9)	9288	Cell signaling; RRID: AB_331470
anti-Rps6(S235/236)	2211	Cell signaling; RRID: AB_331679
Bacterial and virus strains		
Rosetta (DE3) Competent Cells - Novagen	Millipore Sigma	Cat# 70954-3
E.coli XL-1 Blue	Agilent	Cat# 200249
Chemicals, peptides, and recombinant proteins		
Gibson Assembly Master mix	NEB	Cat# E2611S
[γ-32P]ATP	Perkin Elmer	Cat# BLU002250UC
Ni-NTA Beads	Qiagen	Cat# 30210
PD-10 desalting column	GE	Cat# 17085101
Rapamycin	Tocris Bioscience	Cat# 1292
Sorbitol	Sigma-Aldrich	Cat# S1876
Lambda Protein Phosphatase	NEB	Cat# P0753S
GA3-AM	Tocris Bioscience	Cat. No. 5407
Experimental models: Organisms/strains		
S.cerevisiae: W303 MATa leu2-3, 112 trip1-1 can1-100 ura3-1 ade2-1 ade2-1 his3-11-,15	DOM0090	David Morgan Lab
W303 + HIS3::PRpl18-mCherry-Elk1WT-1SIM	LH-DJ001	Holt lab
W303 + HIS3::PRpl18-mCherry-Elk1WT-1SIM, LEU2::PPAB1-GFP-ERK1R84S-1SIM	LH-DJ002	Holt lab
W303 + HIS3::PRpl18-mCherry-Elk1WT-1SIM, URA3::PTDH3-SUMO2	LH-DJ003	Holt lab
W303 + HIS3::PRpl18-mCherry-Elk1WT-1SIM, URA3::PTDH3-SUMO10-SIM6	LH-DJ004	Holt lab
W303 + HIS3::PRpl18-mCherry-Elk1WT-1SIM, LEU2::PPAB1-GFP-ERK1R84S-1SIM, URA3::PTDH3-SUMO2	LH-DJ005	Holt lab
W303 + HIS3::PRpl18-mCherry-Elk1WT-1SIM, LEU2::PPAB1-GFP-ERK1R84S-1SIM, URA3::PTDH3-SUMO10-SIM6	LH-DJ006	Holt lab
W303 + HIS3::PRNR2-mCherry-Elk1DM-1SIM	LH-DJ007	Holt lab
W303 + HIS3::PRNR2-mCherry-Elk1DM-1SIM, LEU2::PPAB1-GFP-ERK1R84S-1SIM	LH-DJ008	Holt lab

(*Continued on next page*)

Continued

REAGENT or RESOURCE	SOURCE	IDENTIFIER
W303 + HIS3::PRNR2-mCherry-Elk1DM-1SIM, URA3::PTDH3-SUMO2	LH-DJ009	Holt lab
W303 + HIS3::PRNR2-mCherry-Elk1DM-1SIM, URA3::PTDH3-SUMO10-SIM6	LH-DJ010	Holt lab
W303 + HIS3::PRNR2-mCherry-Elk1DM-1SIM, LEU2::PPAB1-GFP-ERK1R84S-1SIM, URA3::PTDH3-SUMO2	LH-DJ011	Holt lab
W303 + HIS3::PRNR2-mCherry-Elk1DM-1SIM, LEU2::PPAB1-GFP-ERK1R84S-1SIM, URA3::PTDH3-SUMO10-SIM6	LH-DJ012	Holt lab
W303 + HIS3::PRpl18-mCherry-Elk1WT11APMU-1SIM	LH-DJ013	Holt lab
W303 + HIS3::PRpl18-mCherry-Elk1WT11APMU-1SIM, LEU2::PPAB1-GFP-ERK1R84S-1SIM, URA3::PTDH3-SUMO10-SIM6	LH-DJ014	Holt lab
W303 + HIS3::PRpl18-mCherry-Elk1WT-1SIM, LEU2::PPAB1-GFP-ERK1R84S-1SIM, URA3::PTDH3-SUMO10-SIM6	LH-DJ015	Holt lab
W303 + HIS3::PRNR2-mCherry-Elk1DM-1SIM,FUS3-GFP-2SIM::KANMX, URA3::PTDH3-SUMO2	LH-DJ016	Holt lab
W303 + HIS3::PRNR2-mCherry-Elk1DM-1SIM,FUS3-GFP-2SIM::KANMX, URA3::PTDH3-SUMO10-SIM6	LH-DJ017	Holt lab
W303 + HIS3::PRNR2-mCherry-Elk1DM-1SIM,CDC28-GFP-1SIM::KANMX	LH-DJ018	Holt lab
W303 + HIS3::PRNR2-mCherry-Elk1DM-1SIM,CDC28-GFP-1SIM::KANMX, URA3::PTDH3-SUMO2	LH-DJ019	Holt lab
W303 + HIS3::PRNR2-mCherry-Elk1DM-1SIM,CDC28-GFP-1SIM::KANMX, URA3::PTDH3-SUMO10-SIM6	LH-DJ020	Holt lab
W303 + HIS3::PRpl18-mCherry-Elk1WT-1SIM,TRP::PRNR2-2XNES-GFP-2XWW, LEU2::PPAB1-GFP-ERK1R84S-1SIM, URA3::PTDH3-SUMO10-SIM6	LH-DJ021	Holt lab
W303 + HIS3::PRpl18-mCherry-Elk1WT-1SIM,TRP::PRNR2-2XNES-GFP-2XWW, LEU2::PPAB1-GFP-ERK1K71R-1SIM, URA3::PTDH3-SUMO10-SIM6	LH-DJ022	Holt lab
W303 + HIS3::PTDH3-mCherry-2xElk1DM-3SIM,TRP::PRPL18-1xNLS-GFP-2XWW, LEU2::PTDH3-2xNLS-BFP, URA3::PTDH3-SUMO10-SIM6	LH-DJ023	Holt lab
W303 + HIS3::PTDH3-mCherry-2xElk1DM-3SIM,TRP::PRPL18-1xNLS-GFP-2XWW, LEU2::PTDH3-2xNLS-BFP, CDC28-mCherry-1SIM::KANMX, URA3::PTDH3-SUMO10-SIM6	LH-DJ024	Holt lab
W303 + HIS3::PRPL18-mCherry-EPCT383-5SIM	LH-DJ025	Holt lab

(*Continued on next page*)

Continued

REAGENT or RESOURCE	SOURCE	IDENTIFIER
W303 + HIS3::PRPL18-mCherry-EPCT383-5SIM, LEU2::PPAB1-GFP-ERK1R84S-5SIM	LH-DJ026	Holt lab
W303 + HIS3::PRPL18-mCherry-EPCT383-5SIM, URA3::PTDH3-SUMO10-SIM6	LH-DJ027	Holt lab
W303 + HIS3::PRPL18-mCherry-EPCT383-5SIM, LEU2::PPAB1-GFP-ERK1R84S-5SIM, URA3::PTDH3-SUMO2	LH-DJ028	Holt lab
W303 + HIS3::PRPL18-mCherry-EPCT383-5SIM, LEU2::PPAB1-GFP-ERK1R84S-5SIM, URA3::PTDH3-SUMO2	LH-DJ029	Holt lab
W303 + LEU2::PPAB1-GFP-ERK1R84S-5SIM, URA3::SUMO10-SIM6 HIS3::PRPL18-mCherry-EPCT383-5SIM,	LH-DJ030	Holt lab
W303 + LEU2::PPAB1-GFP-ERK1R84S-5SIM, URA3::SUMO10-SIM6, HIS3::PRPL18-mCherry-EPCT383-5SIM truncation	LH-DJ031	Holt lab
W303 + LEU2::PPAB1-GFP-ERK1R84S-5SIM, URA3::SUMO10-SIM6, HIS3::PRPL18-mCherry-EPCT383-5SIM S394Del	LH-DJ032	Holt lab
W303 + LEU2::PPAB1-GFP-ERK1R84S-5SIM, URA3::PSUMO10-SIM6, HIS3::PRPL18-mCherry-EPCT383-5SIM S375A	LH-DJ033	Holt lab
W303 + LEU2::PPAB1-GFP-ERK1R84S-5SIM, URA3::SUMO10-SIM6, HIS3::PRPL18-mCherry-EPCT383-5SIM 4SDel	LH-DJ034	Holt lab
W303 + LEU2::PPAB1-GFP-ERK1R84S-5SIM, HIS3::PRPL18-mCherry-EPCT383-5SIM	LH-DJ035	Holt lab
W303 + LEU2::PPAB1-GFP-ERK1R84S-5SIM, HIS3::PRPL18-mCherry-EPCT383-5SIM truncation	LH-DJ036	Holt lab
W303 + HIS3::PRpl18-mCherry-PR-3SIM	LH-DJ037	Holt lab
W303 + HIS3::PRpl18-mCherry-PR-3SIM,CDC28-GFP-1SIM::KANMX	LH-DJ038	Holt lab
W303 + HIS3::PRpl18-mCherry-PR-3SIM,URA3::PTDH3-SUMO10-SIM6	LH-DJ039	Holt lab
W303 + HIS3::PRpl18-mCherry-PR-3SIM,CDC28-GFP-1SIM::KANMX,URA3::PTDH3-SUMO10-SIM6	LH-DJ040	Holt lab
W303 + HIS3::PRpl18-mCherry-PR-3SIM,CDC28-GFP-1SIM::KANMX,URA3::PTDH3-SUMO2	LH-DJ041	Holt lab
W303 + HIS3::PRNR2-mCherry-Elk1DMI9P-1SIM, LEU2::PPAB1-GFP-ERK1R84S-1SIM, URA3::PTDH3-SUMO10-SIM6	LH-DJ042	Holt lab
W303 + HIS3::PRNR2-mCherry-Elk1DM-1SIM, LEU2::PPAB1-GFP-ERK1R84S-1SIM, URA3::PTDH3-SUMO10-SIM6	LH-DJ043	Holt lab
W303 + HIS3::PRPL18-mCherry-Elk1DM-1SIMI9P, LEU2::PPAB1-GFP-ERK1R84S-1SIM, URA3::PTDH3-SUMO10-SIM6	LH-DJ044	Holt lab
W303 + HIS3::PRNR2-mCherry-Elk1DM-2SIM, LEU2::PPAB1-GFP-ERK1R84S-2SIM, URA3::PTDH3-SUMO10-SIM6	LH-DJ045	Holt lab
W303 + HIS3::PRPL18-mCherry-Elk1DM-1SIM, LEU2::PRPL18-GFP-ERK1R84S-1SIM, URA3::PTDH3-SUMO10-SIM6	LH-DJ046	Holt lab
W303 + HIS3::PRNR2-mCherry-Elk1DM-1SIM, LEU2::PPAB1-GFP-ERK1R84S-1SIM, URA3::PTDH3-SUMO7-SIM6	LH-DJ047	Holt lab
W303 + HIS3::PRPL18mCherry-Elk1DM-1SIM, LEU2::PRPL18-GFP-ERK1R84S-1SIM	LH-DJ048	Holt lab

(*Continued on next page*)

Continued

REAGENT or RESOURCE	SOURCE	IDENTIFIER
W303 + HIS3::PRPL18mCherry-Elk1DM-1SIM, LEU2::PRPL18-GFP-ERK1R84S-1SIM, URA3::PTDH3-SUMO7-SIM6	LH-DJ049	Holt lab
W303 + HIS3::PRpl18-mCherry-Elk1WT-1SIM, LEU2::PRPL18-GFP-ERK1R84S-1SIM, URA3::PTDH3-Dimer-1SUMO	LH-DJ050	Holt lab
W303 + HIS3::PRpl18-mCherry-Elk1DM-1SIM, LEU2::PRPL18-GFP-ERK1R84S-1SIM, URA3::PTDH3-Dimer-1SUMO, TRP::PTDH3-Hexamer	LH-DJ051	Holt lab
W303 + HIS3::PRpl18-mCherry-Elk1DM-1SIM, LEU2::PRPL18-GFP-ERK1R84S-1SIM, URA3::PTDH3-Dimer-2SUMO, TRP::PTDH3-Hexamer	LH-DJ052	Holt lab
W303 + HIS3::PRpl18-mCherry-Elk1DM-1SIM, LEU2::PRPL18-GFP-ERK1R84S-1SIM, URA3::PTDH3-Dimer-3SUMO, TRP::PTDH3-Hexamer	LH-DJ053	Holt lab
W303 + HIS3::PRpl18-mCherry-Elk1DM-1SIM, LEU2::PRPL18-GFP-ERK1R84S-1SIM, URA3::PTDH3-Dimer-weak08-1SUMO, TRP::PTDH3-Hexamer	LH-DJ054	Holt lab
W303 + HIS3::PRNR2-mCherry-Elk1DM-1SIM, LEU2::PPAB1-GFP-ERK1R84S-1SIM, URA3::PTDH3-SUMO7-SIM6, hog1Δ::KANMX	LH-DJ055	Holt lab
W303 + HIS3::PRNR2-mCherry-Elk1DM-1SIM, LEU2::PPAB1-GFP-ERK1R84S-1SIM, URA3::PTDH3-Dimer-weak08-1SUMO, *TRP*::PTDH3-Hexamer, *hog1Δ*::KANMX	LH-DJ056	Holt lab
W303 + HIS3::PRNR2-mCherry-Elk1DM-1SIM, LEU2::PPAB1-GFP-ERK1R84S-1SIM, URA3::PTDH3-Dimer-weak08-1SUMO, hog1Δ::KANMX	LH-DJ057	Holt lab
W303 + HIS3::PRNR2-mCherry-Elk1DM-1SIM, LEU2::PPAB1-GFP-ERK1R84S-1SIM, URA3::PTDH3-SUMO2, *hog1Δ*::KANMX	LH-DJ058	Holt lab
W303 + HIS3::PRNR2-mCherry-Elk1DM-1SIM, LEU2::PPAB1-GFP-ERK1R84S-1SIM, URA3::PTDH3-SUMO10, *TRP*::PTDH3-Hexamer-1SIM, *hog1Δ*::KANMX	LH-DJ059	Holt lab
W303 + HIS3::PRNR2-mCherry-Elk1DM-1SIM, LEU2::PPAB1-GFP-ERK1R84S-1SIM, URA3::PTDH3-SUMO10-SIM6, hog1Δ::KANMX	LH-DJ060	Holt lab
W303 + HIS3::PRpl18-mCherry-Elk1DM-1SIM, LEU2::PRPL18-GFP-ERK1R84S-1SIM, URA3::PTDH3-SUMO7-SIM6, *hog1Δ*::KANMX	LH-DJ061	Holt lab
W303 + HIS3::PRNR2-mCherry-Elk1DM-1SIM, LEU2::PPAB1-GFP-ERK1R84S-1SIM, URA3::PTDH3-Dimer-weak08-1SUMO, *TRP*::PTDH3-Hexamer, *hog1Δ*::KANMX	LH-DJ062	Holt lab
W303 + HIS3::PRNR2-mCherry-Elk1DM-1SIM, LEU2::PPAB1-GFP-ERK1R84S-1SIM, URA3::PTDH3-SUMO7-SIM6, hog1Δ::KANMX, sfp1Δ::KANMX	LH-DJ063	Holt lab
W303 + HIS3::PRNR2-mCherry-Elk1DM-1SIM, LEU2::PPAB1-GFP-ERK1R84S-1SIM, URA3::PTDH3-SUMO7-SIM6, *hog1Δ*::KANMX, *fus3Δ*::NATMX	LH-DJ064	Holt lab
BY4741 + LEU2::PINO4-PFV-GS-Sapphire	LH4258	Holt lab
BY4741 + sfp1Δ::HPHNT1 + LEU2::PINO4-PFV-GS-Sapphire	LH4259	Holt lab
Recombinant DNA		
pAV103-PRpl18-mCherry-Elk1WT-1SIM	pLH-DJ001	Holt lab
pAV103-PRNR2-mCherry-Elk1DM-1SIM	pLH-DJ002	Holt lab
pAV103-PRpl18-mCherry-Elk1DM-1SIM	pLH-DJ003	Holt lab
pAV103-PRpl18-mCherry-Elk1WT11APMU-1SIM	pLH-DJ004	Holt lab

(*Continued on next page*)

Continued

REAGENT or RESOURCE	SOURCE	IDENTIFIER
pAV103-PRNR2-mCherry-Elk1DMI9P-1SIM	pLH-DJ005	Holt lab
pAV103-PRPL18-mCherry-Elk1DMI9P-1SIM	pLH-DJ006	Holt lab
pAV103-PRPL18-mCherry-EPCT383-5SIM	pLH-DJ007	Holt lab
pAV103-PRPL18-mCherry-EPCT383Trncation-5SIM	pLH-DJ008	Holt lab
pAV103-PRPL18-mCherry-EPCT383S394Del-5SIM	pLH-DJ009	Holt lab
pAV103-PRPL18-mCherry-EPCT383S375A-5SIM	pLH-DJ010	Holt lab
pAV103-PRPL18-mCherry-EPCT3834SDEL-5SIM	pLH-DJ011	Holt lab
pAV103-PRpl18-mCherry-PR-3SIM	pLH-DJ012	Holt lab
pAV103-PTDH3-mCherry-2xElk1DM-3SIM	pLH-DJ013	Holt lab
pAV103-PRNR2-mCherry-Elk1DM-1SIMI9P	pLH-DJ014	Holt lab
pAV103-PRPL18-mCherry-Elk1DM-1SIMI9P	pLH-DJ015	Holt lab
pAV103-PRNR2-mCherry-Elk1DM-2SIM	pLH-DJ016	Holt lab
pAV105-PPAB1-GFP-Erk1R84S-1SIM	pLH-DJ017	Holt lab
pAV105-PRPL18-GFP-Erk1R84S-1SIM	pLH-DJ018	Holt lab
pAV105-PPAB1-mCherry-Erk1R84S-3SIM	pLH-DJ019	Holt lab
pAV105-PPAB1-mCherry-Erk1K71R-3SIM	pLH-DJ020	Holt lab
pAV105-PPAB1-GFP-Erk1R84S-5SIM	pLH-DJ021	Holt lab
pAV105-PPAB1-GFP-Erk1R84S-2SIM	pLH-DJ022	Holt lab
pAV105-PPAB1-GFP-Erk1R84S-3SIM	pLH-DJ023	Holt lab
pAV105-PTDH3-2xNLS-BFP	pLH-DJ024	Holt lab
pRS306-PTDH3-SUMO2	pLH-DJ025	Holt lab
pRS306-PTDH3-SUMO10	pLH-DJ026	Holt lab
pRS306-PTDH3-SUMO10-6SIM	pLH-DJ027	Holt lab
pRS306-PTDH3-Dimer-1SUMO	pLH-DJ028	Holt lab
pRS306-PTDH3-Dimer-2SUMO	pLH-DJ029	Holt lab
pRS306-PTDH3-Dimer-3SUMO	pLH-DJ030	Holt lab
pRS306-PTDH3-Dimer-weak08-1SUMO	pLH-DJ031	Holt lab
pRS306-PTDH3-SUMO7-6SIM	pLH-DJ032	Holt lab
pRS3304-PRNR2-2XNES-GFP-2XWW	pLH-DJ033	Holt lab
pRS3304-RPL18-1xNLS-GFP-2XWW	pLH-DJ034	Holt lab
pRS3304-PTDH3-HEXAMER	pLH-DJ035	Holt lab
pRS3304-PTDH3-HEXAMER-1SIM	pLH-DJ036	Holt lab
pET28b-SUMO10	pLH-DJ037	Holt lab
pET28b-FKBP12-6SIM	pLH-DJ038	Holt lab
pET28b-FRB-mCherry-Erk1	pLH-DJ039	Holt lab
pET28b-FRB-GFP-Elk1	pLH-DJ040	Holt lab
pFA6a-CDK-GFP-1SIM	pLH-DJ041	Holt lab
pFA6a-FUS3-GFP-2SIM	pLH-DJ042	Holt lab
Software and algorithms		
FIJI (FIJI is just image J)	Schindelin et al., 2012	http://www.nature.com/nmeth/journal/v9/n7/full/nmeth.2019.html
Image J2	Schindelin et al., 2015	http://onlinelibrary.wiley.com/https://doi.org/10.1002/mrd.22489/full
MOSAIC for ImageJ	Shivanandan et al., 2013	https://bmcbioinformatics.biomedcentral.com/articles/10.1186/1471-2105-14-349
MATLAB 2019a	MathWorks, Inc.	https://www.mathworks.com/products/matlab.html
Nikon Elements	Nikon Instruments, Inc.	https://www.nikoninstruments.com/Products/Software

(*Continued on next page*)

Continued

REAGENT or RESOURCE	SOURCE	IDENTIFIER
pcrma package	Borchers and Borchers, 2021	https://cran.r-project.org/web/packages/pracma/index.html
Scripts for droplet properties analysis and GEM & Ribosome concentration analysis	This article	https://doi.org/10.5281/zenodo.6979049

RESOURCE AVAILABILITY

Lead contact

Further information and requests for resources aCnd reagents should be directed to and will be fulfilled by the lead contact, Liam J. Holt (liam.holt@nyulangone.org).

Materials availability

All materials will be made available on request.

Data and code availability

- All data reported in this paper will be shared by the lead contact upon request.
- All code is available at: https://doi.org/10.5281/zenodo.6979049.
- Any additional information required to reanalyze the data reported in this work paper is available from the Lead Contact upon request.

EXPERIMENTAL MODEL AND SUBJECT DETAILS

Escherichia coli strains

XL-1 blue competent bacterial strains were grown in lysogeny broth (LB) containing antibiotic selection in a shaking incubator at 220 rpm, 37°C.

Rosetta2 DE3 competent cells were grown in LB containing antibiotic selection in a shaking incubator at 220 rpm for 18 h at 16°C. Recombinant protein expression was induced by addition of 100 μM IPTG.

Yeast strains

Plasmids were transformed into W303 strain and grown in a rotating drum incubator in synthetic dropout (SD) media –Leu, -His, -Trp, or –Ura, respectively at 30°C.

METHOD DETAILS

Yeast transformation

Yeast strains were created by transforming with a LiAc based approach according to Cold Spring Harbor Protocols (Amberg et al., 2006). All strains were constructed in the W303 strain background (*MATa leu2-3, 112 trip1-1 can1-100 ura3-1 ade2-1 ade2-1 his3-11-,15*). A list of strains built is provided in Table S1. To tag Cdk1 and Fus3 with GFP-SIM, pFA6a-CDK-GFP-SIM or pFA6a-FUS3-GFP-2xSIM, the plasmid was cut within the coding sequences of Cdk1 or Fus3, and the linearized plasmid was then transformed, leading to recombination into the endogenous locus. As the plasmids do not contain a promoter, this leads to a tagged allele, and inactivation of the endogenous allele.

Plasmid construction

The open reading frames encoding $SUMO_{10}$-SIM_6 condensates, GFP-MAPK3-1SIM and mCherry-ELK1-1SIM were chemically synthesized (Qinglan, China). The $SUMO_{10}$-SIM_6 condensate expression plasmid in yeast was constructed by fusion 5' end of the ORF with the strong promoter from *TDH3* by Gibson assembly (Gibson et al., 2009) into the pRS306 vector (Sikorski and Hieter, 1989). Plasmids for kinase expression in yeast were constructed with either a weak (from the *PAB1* gene), or medium promoter (from the *RPL18* gene) by Gibson assembly into the pAV105 vector (Agmon et al., 2015). Substrate expression plasmids were similarly constructed with either yeast weak (from the *RNR2* gene), or medium (from the *RPL18* gene) promoters in the pAV103 vector (Agmon et al., 2015). To express the rigid synthetic condensate components in yeast, the dimer and hexamer components were amplified by PCR and assembled into pRS306 vector or pRS304 vector (Sikorski and Hieter, 1989) by Gibson assembly. The WW reporter was generated by fusion of GFP to a tandem repeat of the WW domain from Peptidyl-prolyl cis-trans isomerase NIMA-interacting 1, *Homo sapiens*. This protein was expressed from the promoter of the *RPL18* gene and assembled into the pRS304 vector (Sikorski and Hieter, 1989). To tag Cdk1 and Fus3 with GFP-SIM, Cdk1/Fus3 CDS, GFP and SIM tag were amplified and assembled into pFA6a

vector (Sikorski and Hieter, 1989) by Gibson (Bähler et al., 1998). All yeast plasmids were integrated into the host genome. pET28b vectors were used for bacterial expression. Open Reading Frames (ORFs) of the $SUMO_{10}$, FKBP12-SIM_6, FRB-mCherry-MAPK3 and FRB-GFP-ELK1 proteins were fused at the N terminus to the 6x histidine tag for purification. The ORFs and the vectors were Gibson assembled. A list of plasmids constructed is provided in Table S2.

Protein purification

Protein purification from *E. coli* cells was performed as previously described (Howard et al., 2014). Briefly, proteins were expressed in Rosetta2 DE3 competent cells by induction with 100 μM IPTG for 18 hr at 16°C. Bacterial culture were collected and centrifuged at 4000 rpm for 20 min at 4°C. The cell pellet was resuspended in cold lysis buffer (50 mM NaH2PO4, 300 mM NaCl, 10 mM imidazole pH7.6, 1 mM PMSF). After sonication, the lysate was centrifuged at 12000 rpm for 20 min at 4°C. The supernatant was mixed with magnetic Ni-NTA beads (Qiagen) and incubated for 2 hr at 4°C. The bound beads were collected and rinsed 3 × with wash buffer containing (50 mM NaH2PO4, 300 mM NaCl, 20 mM imidazole pH7.6). The bound proteins were eluted with elution buffer (50 mM NaH2PO4, 300 mM NaCl, 500 mM imidazole pH7.6). The eluted proteins were concentrated using Amicon® Ultra Centrifugal Filters (Millipore Sigma). The concentrated proteins were dialyzed into SUMO-SIM protein buffer (150 mM KCl, 20 mM HEPES pH 7, 1 mM MgCl2, 1 mM EGTA, 1 mM DTT) with 10% glycerol using PD10 columns (GE Healthcare), followed by further concentration using an Amicon Ultra 30K device (Millipore) at 4C, and finally flash frozen in aliquots with liquid nitrogen and stored at -80°C.

In vitro kinase assays

For phosphorylation in condensates, the components for kinase reaction and condensate formation were divided into two halves, each with a 10 μl volume. Combination of these two mixtures initiated the kinase reaction. The first half contained 30 μM FKBP12-SIM_6, 40 nM FRB-GFP-MAPK3, 8 μM FRB-mCherry-ELK1, 50 μM Rapamycin (or same volume of DMSO), 10 mM $MgCl_2$ and 75 mM KCl. Components were equilibrated for 20 minutes. The phosphorylation was started by addition of the second half, which contained 24 μM $SUMO_{10}$, 200 μM ATP, 10 mM $MgCl_2$, 75 mM KCl and 0.1 μCi of [γ-32P]ATP. The two halves were mixed thoroughly by gentle pipetting. Reactions were carried out at room temperature for 5 minutes and terminated by addition of 10 μl 5x SDS loading buffer (10% SDS, 0.5 M DTT, 50% glycerol, 0.25% Bromophenol blue). All samples were separated on 4–12% Bis-Tris gels (ThermoFisher Scientific). The gel was dried and exposed to a phosphor screen. Phosphor screens were analyzed with a Typhoon 9500 scanner (GE) using ImageQuant software (GE).

MAPK3-GFP total partition calculation

While the reaction proceeded, the other half of the solution was transferred to a 384-well glass bottomed imaging plates and imaged using an Andor Yokogawa CSU-X confocal spinning disc on a Nikon TI Eclipse microscope. Fluorescence was recorded with a sCMOS Prime95B camera (Photometrics) with a 100x objective (pixel size: 0.11um). A stack of 50 images were acquired at 1μM intervals from the bottom of the plate upwards. A blank well with buffer was imaged to determine the camera background value. This background value was subtracted from every image. The fluorescence integrated density of 'drops' or 'solvent' in the 488 and 561 channels was calculated using a classifier mask derived from contrast adjusted imaged segmented with the trainable Weka Segmentation package on default settings. The condensates are denser than the solution and sediment near the bottom of the well. Therefore, the reaction is asymmetrically distributed along the z axis and symmetric along the x & y axes. We reasoned that it would be necessary to calculate the total protein in the solvent and condensates along the entire vertical stack to calculate the total partition of a given volume. It was calculated that given the volume of reaction added to the well, there would be an additional 2490 'slices' spaced out every 1uM on top of the 50 μM imaged. It was observed that condensates never formed in slices 48-51 as the condensates had sedimented below this point. It should also be noted that carefully controlling temperature and evaporation are required to prevent solution turbidity. Therefore, the average solvent protein concentration was determined by finding the mean integrated density per slice in this 'top of the well' equivalent from slices 48-51. Next, the condensate and solvent protein concentrations across the entire well were calculated by integrating along the slices using the 'trapz' function from the pcrma package (Borchers and Borchers, 2021). To calculate total MAPK3-GFP partition , the total protein in condensates was divided by the total concentration in solution across the entire y dimension. The scripts used for partition coefficient calculation are provided in supplementary files as QC1 and QC2.

Western blots

Cell cultures were grown to OD 0.6–0.8. Cells were collected and treated with 1M LiAc for 5 min on ice. After centrifugation cell pellets were treated with 0.4M NaOH for 5 min. Then cells were centrifuged again, and were suspended in SDS-PAGE sample buffer and boiled for 5min. Supernatant samples were separated on 10% SDS-PAGE gels and transferred to Immobilon-FL PVDF membrane (Millipore). Membranes were probed with primary antibodies, including anti-p-ELK1-S383, anti-ELK1, anti-p-MAPK3, anti-ERK2, anti-Tubulin, anti-HA, anti-p-P53-S37, anti-p-P53-S9, anti-p-RPS6-S235/236 and anti-p-Sata3-Y705 (key resources table in STAR Methods), and corresponding secondary IRDye 800CW antibodies (LI-COR Biosciences). Band intensities were quantified with Image Studio™ analysis software (LI-COR Biosciences).

For hyperphosphorylation (Hypershift/Tubulin) quantification, the intensity signal of hypershifted phosphorylated band (detected by anti-p-ELK1-S383, which is indicated by the red arrowheads in the western blot gel figure) was normalized to the intensity signal of tubulin band (detected by anti-Tubulin).

Cell perturbations

For α factor experiments, cells were grown to log phase (OD 0.2 - 0.8) and then treated with 2 μM α factor for up to 1 h, then collected by centrifugation for 3min at 3000g and lysed for western blot.

For sorbitol treatments, log phase cells were collected by centrifugation for 3min at 3000g. Cells were then suspended in media with or without 1 M sorbitol, grown for 1h, and then collected and lysed as above.

For rapamycin treatment, log phase cells were incubated with DMSO (solvent control) or 1 μM rapamycin for 2h. Then cells were collected as above for western blot.

For treatment with rapamycin combined with sorbitol, cells were first incubated with 1 μM rapamycin for 1 h or 1 μM DMSO (solvent control), then collected by centrifugation for 3min at 3000g. Cells were next resuspended in media with 1 μM rapamycin or 1 μM DMSO, with or without 1 M sorbitol for an additional 1 h. Then cells were collected and lyses as above.

Phosphatase treatment of yeast lysates

Yeast cell were collected when the culture OD reach 0.8. Cells were pretreated with 0.4M NaOH for 2 min on ice. After centrifugation, cell pellets were suspended in lysis buffer with protease inhibitor tablet (Pierce) and lysed by bead beating. Then samples were centrifuged at 800g for 2 minutes. The supernatants were incubated with lambda protein phosphatase (NEB) according to the manufacturer's protocol. For treatment with phosphatase inhibitor, NaF (final 50 mM), β-glycerol phosphate (final 50 mM), and Na3VO4 (final 1 mM) were added. The lysates were incubated at 30°C for 30 minutes and terminated by addition of 5x SDS loading buffer followed by boiling for 5 minutes.

Imaging and quantification of fluorescence intensity inside condensates and condensate size

Cells were imaged using TIRF Nikon TI Eclipse microscope in epifluorescence mode, and fluorescence was recorded with an sCMOS camera (Zyla, Andor) with a 100x objective. GFP and mCherry channel images were generated by average projection of 13 z-slices with 0.4 μm spacing (4.8 μm total). Condensate properties within cells were characterized using the TrackMate ImageJ plugin (Schindelin et al., 2012; Schindelin et al., 2015; Tinevez et al., 2017). Due to relatively higher intensity and higher contrast in GFP fluorescent signals, condensates in GFP channel were first detected using LoG (Laplacian of Gaussian filter) detector with one micron 'Estimated blob diameter' and a fixed 'Threshold' across all experimental conditions. For each individual image with both GFP and mCherry channels, the number of detected condensates within the GFP channel was then recorded and was used as a criterion for choosing the 'Threshold' parameter for condensate detection in the mCherry channel. The 'Estimated blob diameter' parameter for mCherry condensate detection still maintained as one. Using this method, the majority of condensates detected in both channels overlapped with each other. Particle detection results from TrackMate were saved as *xml* files. We then extracted and compiled particle properties in both channels, especially condensate mean pixel intensity, using home-written MATLAB code. In addition, we also extracted the background mean pixel intensity by randomly selecting 20 circles in each image from areas away from cellular condensates. Thus, the final condensate mean pixel intensity were calculated by subtracting the background mean pixel intensity from condensate mean pixel intensity identified above.

For calculation of condensate area and client concentration changes, log-phase cells were immobilized in 384-well imaging plates coated with concanavalin A (ConA). GFP and mCherry channel images were generated by average projection of 13 z-slices with 0.4 μm spacing (4.8 μm total). For experiments with sorbitol treatment only, immobilized cells were imaged, then media was carefully removed and replaced with media containing 1M sorbitol, and the same cells were imaged again after 1h. For experiments under various conditions, such as rapamycin treatment, cells were immobilized, imaged and then media was carefully changed, and cells were imaged again after 2h with 1 μM rapamycin. For treatment with rapamycin and sorbitol, cells were imaged, then were treated sequentially with 1μM rapamycin for 1h, then old medium was removed and incubated with fresh SCM with 1μM rapamycin and 1M sorbitol for a further 1h, and cells were imaged again. Condensates were identified manually based on their GFP signal, and the area of the same condensate before and after treatment was calculated by measurement in Image J (Schindelin et al., 2012; Schindelin et al., 2015).

HILO imaging of GEMs

GEM particles in *S. cerevisiae* yeast cells were imaged using Highly inclined thin illumination (HILO) TIRF Nikon TI Eclipse microscope in partial TIRF mode under 100% power of 488nm excitation laser. The emitted fluorescent signals were transmitted through a 100x objective (100x Phase, Nikon, oil NA = 1.4, part number = MRD31901) and recorded with a sCMOS camera (Zyla, Andor, part number = ZYLA-4.2p-CL10). The GFP filter set (ET-EGFP (FITC/Cy2), Chroma, part number = 49002) was embedded within the light path, which includes an excitation filter (Excitation wavelength/ Bandwidth (FWHM) = 470/40 nm), a dichroic mirror (long pass beamsplitter, reflecting < 495 nm and transmitting > 495 nm wavelength) and an emission filter (Emission wavelength/ Bandwidth (FWHM) = 525/50 nm). Each GEM movie was recorded at a single focal plane with 10 ms frame rate with no delay (100 Hz) for a total of 4 s (400 frames

total), using Nikon NIS-Elements Advanced Research software. Trajectories of GEM particles from each GEM movie were subsequently analyzed using Mosaic plugin in ImageJ/FIJI (Schindelin et al., 2012; Schindelin et al., 2015; Shivanandan et al., 2013).

Calculation of effective diffusion constant

For every 2D GEM trajectory, we calculated the time-averaged mean-square displacement (MSD) at different time intervals:

$$< \Delta r^2(\tau) >_T = < [x(t+\tau) - x(t)]^2 + [y(t+\tau) - y(t)]^2 >_T \quad \text{(Equation 1)}$$

where '$< >_T$' represents time averaging for each trajectory of all displacements for time interval τ.

To reduce statistical error, we limited our analyses to particle trajectories with longer than 10 time points. The time-averaged MSD for each trajectory was then fitted for the first 10 time intervals:

$$MSD(\tau)_T = 4D_{eff}\tau \quad \text{(Equation 2)}$$

where D_{eff} is effective diffusion coefficient for each trajectory (units of $\mu m^2/s$).

For each experimental condition, we then used the median value of D_{eff} from all trajectories (typically thousands of trajectories from hundreds of cells) and plotted bar graphs with error bars as standard error of the mean.

Relative ribosome concentration calculation

We inferred ribosome concentration based on a model derived from the phenomenological Doolittle equation (Doolittle, 1951; Delarue et al., 2018).

$$\log\left(\frac{D}{D_0'}\right) = \zeta \frac{\varphi_0/\varphi_m}{1 - \varphi_0/\varphi_m} \frac{1 - c_{ribo-rela}}{1 - c_{rib0-rela*}\varphi_0/\varphi_m} \quad \text{(Equation 3)}$$

where D represents the experimentally observed effective diffusion coefficient, D_0' represents the effective diffusion coefficient in control conditions, φ_0 is the volume fraction of macromolecules in control conditions, φ_m is the maximum volume fraction of macromolecules when it no longer possible to remove water from the cell, ζ is a dimensionless parameter, representing the interaction strength between the probe particle and its surrounding environment, $c_{ribo-rela}$ is the relative ribosomal concentration compared to control conditions.

When cells are exposed to an instantaneous osmotic pressure, the number of macromolecules can be approximated as unchanged. Thus, $c_{ribo-rela}$ would become the inverse of the normalized cell volume compared to control condition, i.e. $1/\tilde{v}$, where $\tilde{v}$ is the normalized cell volume. By observing the effective diffusion coefficient of GEMs under different osmotic pressures, and measuring the corresponding cell volume (approximating the cell as prolate ellipsoid in brightfield images), the equation parameters: ζ, φ_0/φ_m were obtained by fitting equation (4).

$$\log\left(\frac{D}{D_0'}\right) = \zeta \frac{\varphi_0/\varphi_m}{1 - \varphi_0/\varphi_m} \frac{\tilde{v} - 1}{\tilde{v} - \varphi_0/\varphi_m} \quad \text{(Equation 4)}$$

NMR Methods

Sample preparation for Tau phosphorylation experiment

^{15}N-labeled Tau protein (2N4R Tau; hTau40) was expressed in *Escherichia coli* strain BL21(DE3) from a pNG2 vector (a derivative of pET-3a, Merck-Novagen, Darmstadt) in presence of an antibiotic. Cells were grown, centrifuged at low speed, washed with M9 salts (Na_2HPO_4, KH_2PO_4 and NaCl) and resuspended in minimal medium M9 supplemented with $^{15}NH_4Cl$ as the only nitrogen source and induced with 0.5 mM IPTG. Subsequently, cells were disrupted with a French pressure cell press in lysis buffer (20 mM MES pH 6.8, 1 mM EGTA, 2 mM DTT) complemented with protease inhibitor mixture, 0.2 mM $MgCl_2$, lysozyme and DNAse I. NaCl was added to a final concentration of 500 mM and boiled for 20 minutes. Denaturated proteins were removed by ultracentrifugation at 4 °C. Salt was removed by dialysis and the sample was filtered and purified by ion exchange and gel filtration chromatography. Finally, the protein was dialyzed against HEPES buffer, pH 6.8.

NMR samples were prepared by adding 1 mM TCEP, 5.6 mM $MgCl_2$, 0.1 mM PMSF, 5.6 mM ATP, 5.6% D_2O and 1 mM DSS. The reference sample volume was 180 µl and the LLPS sample, supplemented with 10% dextran T500, reached a final volume of 770 µl in order to get a good amount of the condensate phase that fills the NMR coil. The final protein concentration was 168 µM in both cases. After introducing the sample into a 3 mm Shigemi NMR tube the CDK2/CycA3 enzyme was added with a final concentration of 6.4 µg/ml. The samples were mixed followed by centrifugation at ~1500 g for one hour at room temperature. The reference sample received the same treatment in order to start the experiment in an equivalent condition.

NMR experiments and kinetics analysis

Two-dimensional ^{1}H-^{15}N heteronuclear single quantum coherence (HSQC) experiments were acquired at 278 K on a Bruker 900 MHz spectrometer equipped with a triple-resonance 5 mm cryogenic probe. Spectra were processed with NMRPipe (Delaglio et al., 1995) and analyzed using Sparky (Lee et al., 2015). Despite increased signal overlap in the condensed phase, careful analysis of the sufficiently separated cross-peaks of T205 and S198 (which is neighboring the phosphorylated S199; Figure 6C, right panel) provided

single-residue access to the phosphorylation kinetics inside the Tau condensate (Figure 6D). Peak intensities were extracted from a series of two-dimensional ^{1}H-^{15}N HSQC data sets at one-hour time intervals. After peak assignment using the previously established resonance assignment (Mukrasch et al., 2009), the peak intensities were normalized with respect to the peak intensity of the C-terminal residue (L441). The resulting values were then normalized to the reference intensity values (non-phosphorylated sample) for each phosphorylated residue and analyzed with GraphPad Prism by fitting to first-order decay kinetics. As the temperature during sample preparation was around 298 K (faster phosphorylation kinetics) and the experiment was measured at 278 K, the zero time of the analyzed 278 K kinetics is expected to be negative. This problem was solved by global fitting of the starting point t_0 for all analyzed residues according to:

$$P = A(1 - \exp(-K_{obs}(t - t_0))$$

The four phosphorylation kinetic traces, i.e. S199 in the dispersed phase, T205 in the dispersed phase, S199 in the Tau condensate and T205 in the Tau condensate, were simultaneously fitted to a single value of t_0.

CDK2/CyclinA1-ALEXA 488 LABELLING

CDK2/CyclinA1 was labeled with Alexa Fluor 488 on lysine residues employing Microscale Protein Labeling Kit (Thermo Fisher Scientific). DIC and fluorescence images were recorded using a Leica DM6000B microscope with a 63x objective (water immersion). Imaging analyses were performed using FIJI software ((Schindelin et al., 2012), NIH).

QUANTIFICATION AND STATISTICAL ANALYSIS

Statistical analyses were performed using MATLAB R2019a. Statistical differences between samples within a group were assessed using one-way analysis of variance (ANOVA) and subsequently pairwise post-hoc Tukey-Kramer test, with *: $p<0.05$, **: $p<0.01$, ***: $p<0.001$, N.S.: $p \geq 0.05$. Correlation statistics between two variables were performed using Spearman's rank correlation (ρ), which assesses monotonic relationships whether linear or not. P values were generated based on the null hypothesis of either there is no positive correlation or there is no negative correlation. All quantitative data are presented as the mean ± SEM or ± SD of biologically independent samples (n), unless stated otherwise. Statistical analysis was carried out using MATLAB R2019a software. Statistical differences between samples within a group were assessed using one-way analysis of variance (ANOVA) and subsequently pairwise post-hoc Tukey-Kramer test, *$p<0.05$, **$p<0.01$, **$p<0.001$, N.S. (not significant) $p \geq 0.05$. Spearman's rank correlation was used to assess correlation statistics between two variables.